arXiv:cond-mat/0011152v2 12 Feb 2001

Quantum Phase Transitions and Vortex Dynamics in Superconducting Networks

Rosario Fazio[1,2] and Herre van der Zant[3]
[1] *Dipartimento di Metodologie Fisiche e Chimiche (DMFCI), Università di Catania, viale A. Doria 6, 95125 Catania, Italy*
[2] *Istituto Nazionale per la Fisica della Materia (INFM), Unità di Catania, Italy*
[3] *Department of Applied Sciences and DIMES, Delft University of Technology, Lorentzweg 1, CJ 2628, Delft, The Netherlands*

Abstract

Josephson-junction arrays are ideal model systems to study a variety of phenomena such as phase transitions, frustration effects, vortex dynamics and chaos. In this review, we focus on the quantum dynamical properties of low-capacitance Josephson-junction arrays. The two characteristic energy scales in these systems are the Josephson energy, associated with the tunneling of Cooper pairs between neighboring islands, and the charging energy, which is the energy needed to add an extra electron charge to a neutral island. The phenomena described in this review stem from the competition between single-electron effects with the Josephson effect. They give rise to (quantum) Superconductor-Insulator phase transitions that occur when the ratio between the coupling constants is varied or when the external fields are varied. We describe the dependence of the various control parameters on the phase diagram and the transport properties close to the quantum critical points. On the superconducting side of the transition, vortices are the topological excitations. In low-capacitance junction arrays these vortices behave as massive particles that exhibit quantum behavior. We review the various quantum-vortex experiments and theoretical treatments of their quantum dynamics.

Typeset using REVTEX

Contents

I Introduction **4**
- A Josephson-junction arrays . . . 4
- B Phase-number relation . . . 5
- C Structure of the review . . . 6

II Quantum Phase Transitions **7**
- A The model of a Josephson Junction Array . . . 7
  - 1 Quantum Phase Model . . . 7
  - 2 Dissipative Models . . . 10
  - 3 Related Models . . . 12
- B The zero-field phase diagram . . . 13
  - 1 Mean-Field approach . . . 15
  - 2 Coarse-Graining approach . . . 16
  - 3 Duality transformations . . . 17
  - 4 Berezinskii-Kosterlitz-Thouless transitions . . . 20
- C Magnetic frustration . . . 21
- D Charge frustration and the supersolid . . . 24
  - 1 Phase diagram . . . 24
  - 2 Supersolid . . . 26
- E Dissipation induced S-I transition . . . 27
  - 1 Quasi-particle dissipation . . . 28
  - 2 Ohmic dissipation . . . 29
  - 3 Local damping . . . 29
  - 4 Tunable dissipative environment . . . 30
- F Transport Properties . . . 31
  - 1 Zero-temperature conductivity . . . 33
  - 2 Finite-temperature conductivity . . . 34
  - 3 Non universal behavior . . . 35
- G One-dimensional arrays . . . 35
  - 1 1D arrays as Luttinger Liquids . . . 38
- H Field-tuned transitions . . . 39

III Quantum Vortex Dynamics **40**
- A Classical equation of motion . . . 42
  - 1 Experiments on classical, underdamped arrays . . . 44
  - 2 Spin-wave damping . . . 45
  - 3 The Hall Effect . . . 46
- B Ballistic vortex motion . . . 47
- C Effective single vortex action . . . 49
- D Quantum vortices . . . 52
  - 1 Macroscopic quantum tunneling of vortices . . . 52
  - 2 Vortex interference: the Aharonov-Casher effect . . . 54
  - 3 Bloch oscillations . . . 55
- E One-dimensional vortex localization . . . 57

1 Mott insulator of vortices 57
2 Anderson localization of vortices 59

IV Future directions **60**
A Persistent vortex currents 61
B The Quantum Hall effect 63
C Quantum Computation with Josephson junctions 64

APPENDIXES **68**

A Array fabrication and experimental details **68**

B Triangular arrays and geometrical factors **69**

C Phase correlator **69**

D Derivation of the coupled Coulomb gas action **70**

E Effective single vortex action **72**

F List of symbols **73**

I. INTRODUCTION

A. Josephson-junction arrays

The first artificially fabricated Josephson-Junctions Arrays (JJAs) were realized twenty years ago at IBM [1] as part of their effort to develop an electronics based on superconducting devices. In the first ten years of their existence, Josephson arrays were intensively studied to explore a wealth of classical phenomena [2–6]. JJAs proved to be an ideal model system in which classical phase transitions, frustration effects, classical vortex dynamics, non-linear dynamics and chaos could be studied in a controlled way. The observation of the Berezinskii-Kosterlitz-Thouless (BKT) transition [7,8] in Josephson arrays is probably one of the most spectacular experiments [9] in this respect.

All classical phenomena can be successfully explained by studying the classical (thermo)dynamics of the phases of the superconducting order parameter on each island. This approach is justified because experiments are usually carried out at temperatures well below the BCS transition temperature. Each island is then superconducting with a well defined gap, but phase fluctuations are still allowed. Under these conditions, classical JJAs are a physical realization of the two-dimensional XY-model and above the BKT transition temperature, phase fluctuations destroy global phase coherence preventing the system to reach the superconducting state. Global phase coherence is only restored below temperatures corresponding to the Josephson coupling energy E_J, which is the energy scale associated with Cooper pair tunneling between neighboring islands.

As we now understand, the relatively large junctions at that time had resistances too low [1] to observe clear quantum effects. By the end of the eighties semiconductor technology had pushed device dimensions well below the micron size. It became possible to fabricate arrays with Josephson tunnel junctions of sizes 100×100 nm^2. Circuits with such small junctions showed single-electron effects when cooled down to temperatures corresponding to the charging energy E_C, the energy needed to add an extra electron charge to a neutral island. It was soon realized that the competition between single-electron effects [10,11] and the Josephson effect would lead to new, exciting physics.

An appealing feature of JJAs already emerges at this stage as they can be visualized as model systems to investigate quantum (zero-temperature) phase transitions [12,13]. In recent years, this field of research has attracted the attention of many physicists. Experiments on thin, superconducting films, high-temperature superconductors, spin systems and two-dimensional electron gases have all shown the existence of quantum critical points. In arrays made of submicron junctions, the quantum fluctuations drive the system through a variety of quantum phase transitions. A quantum JJA may be insulating at zero temperature even though each island is still superconducting. In the classical limit $E_J \gg E_C$, the system turns superconducting at low temperatures since the fluctuations of the phases are

[1] A simple estimate for value of the junction resistance above which clear quantum effects become visible can be obtained by using the Heisenberg relation $\Delta E \Delta\tau \geq \hbar$. By taking the charging energy $(e^2/2C)$ for ΔE and τ of the order of the junction RC-time one finds that the junction resistance R_N should satisfy the inequality $R_N > R_Q = h/4e^2$ for quantum effects to be observable.

weak and the system is globally phase coherent. In the opposite limit, $E_J \ll E_C$, the array becomes a Mott insulator since the charges on each islands are localized and an activation energy of the order of E_C is required to transport charges through the system (Coulomb blockade of Cooper pairs). Strong quantum fluctuations of the phases prevent the system from reaching long-range phase coherence in this regime.

Granular superconducting thin films are closely related to arrays. In granular films, superconducting islands of various sizes and with various coupling energies are connected together. Therefore, disorder plays a crucial role in these granular materials while it is virtually absent in JJAs (or it can be introduced in a controlled way). Models based on the behavior of Josephson arrays also form the starting point to describe the physics of ultra-thin, amorphous superconducting films in which superconductivity is quenched by disorder or by an applied magnetic field. In these two-dimensional homogeneous films it is believed that, although the order parameter is suppressed, phase fluctuations are still responsible for driving the system through the Superconductor-Insulator (S-I) transition [14].

Another important field of investigation addressed with JJAs, is the study of the quantum dynamics of macroscopic objects. In the classical limit vortices are the topological excitations that determine the (thermo)dynamic properties of JJAs. In the opposite situation ($E_J \ll E_C$) the charges on each island are the relevant degrees of freedom. Vortices and charges play a dual role and many features of JJAs can be observed in the two limits if the role of charges and vortices are interchanged. By fabricating arrays with different geometries, vortices can be manipulated to a great extent. Quantum dynamics of macroscopic objects requires knowledge of the coupling to the surrounding environment [15]. To a certain degree, the dissipative environment can be modeled and therefore JJAs are prototype systems to study macroscopic quantum mechanics as well. Born as a problem related to the foundations of quantum mechanics, macroscopic coherence in superconducting nanocircuits is acquiring increasing attention since the advent of quantum computation.

B. Phase-number relation

Throughout this review, the interplay between the phase ϕ of an island and number of charge carriers Q on it plays a crucial role. Together they determine the properties of quantum Josephson networks. The competition between these two canonically conjugated variables is captured by the following Heisenberg relation [16]:

$$[\phi_i, Q_j] = 2e\, i\, \delta_{ij}$$

where the subscripts i and j label the island positions.

An elegant illustration of this competition is presented by what became known as the Heisenberg transistor [17,18]. The aim of the experiment was to control and measure the quantum phase fluctuations through a modulation of the critical current of the system. In Fig.1 the layout of the device is shown. Two junctions in series (indicated by crosses) are connected to a current source. The junction parameters are such that $E_J \sim E_C$, i.e., quantum mechanical fluctuations of the number of Cooper pairs and of the phase of the central island are comparable. A large superconducting reservoir is coupled to the island through a Superconducting QUantum Interference Device (SQUID).

In the experiment the critical current was measured as a function of the applied flux through the SQUID ring. It shows a periodic modulation with a period equal to the superconducting flux quantum ($\Phi_0 = h/2e$). The role of the SQUID is to provide a tunable coupling to the reservoir of Cooper pairs. When the flux equals an integer times half a flux quantum ($nPhi_0/2$) the coupling is turned off and fluctuations in the number of Cooper pairs are suppressed. At the same time, phase fluctuations reach their maximum as indicated by the Heisenberg relation. At fields equal to zero or an integer number of flux quanta, the coupling is maximum so that the amount of charge fluctuations reaches a maximum as well. In the experiment, the critical current probes the scale of charge fluctuations: The situation with large charge fluctuations corresponds to favorable Cooper-pair tunneling and a high critical current. Thus, for zero applied field a high critical current is measured because charge fluctuations are at their maximum. At half a flux quantum applied, the critical current reaches its minimum value because phase fluctuations are at their maximum.

C. Structure of the review

This review is organized as follows. In Chapter II the basic physical properties and models are introduced. Some theoretical tools to study the phase diagram including the boundary of the S-I transition are briefly discussed: the mean-field approximation, the coarse-graining approach to derive a Ginzburg-Landau effective free energy, and the Villain transformation that leads to a description in terms of charges and vortices. These approaches capture most of the essential physics. Sections II C and II D are devoted to a description of the phase diagram when charge and/or magnetic frustration are included. Since the number of control parameters that can be varied is large, the phase diagram is discussed in some limiting cases only. Section II E describes the various sources of dissipation in JJAs and their effect on the phase diagram. The final three sections of Chapter II report on the transport properties close to the S-I transition, the S-I transition in one-dimensional arrays and the physics of the field-tuned S-I transitions. In all sections, comparison of the theoretical phase diagrams with the experimental results is discussed as well.

Chapter III deals with quantum vortex dynamics. After introducing the important vortex properties (vortex mass, pinning potential,...) and its classical equation of motion, a theoretical description of quantum corrections to the classical equation of motion is presented. The remainder of the chapter concerns the description of quantum vortex-experiments. We start with the single vortex properties (tunneling, interference, and Bloch oscillations) and then proceed with collective vortex motion in quasi-one dimensional samples (Mott insulation of vortices and Anderson vortex localization).

In the last chapter, some future directions are explored. The theoretical description of two new experiments is outlined: persistent vortex currents in Corbino geometries and the Quantum Hall effect for vortices/charges. The experimental technicalities for the observation of these phenomena are described as well. We end this review with a brief discussion on Josephson qubits in which fundamental aspects of quantum mechanics and quantum information theory can be studied.

We tried to keep this review self-contained and, at the same time, to give a comprehensive overview of the quantum properties of Josephson networks. For each of the sections, we present the main ideas without going into a detailed enumeration of all the results obtained in

the field. There are some topics which are not discussed here. Probably the most important, which would require a review by itself, is the effect of disorder which seems to be more important for granular materials and ultra-thin films.

Basics in superconductivity and Josephson physics can be found in the books by Tinkham [19] and by Barone and Paternò [20]. Since many ideas (e.g. persistent current, localization) were born in the field of more traditional mesoscopic physics we refer for these topics to the books by Beenakker [21] and Imry [22] and to the conference proceedings [23,24]. Various other aspects of JJAs have already been discussed in previous reviews devoted to this topic [25–27].

Throughout the review we put $\hbar = k_B = c = 1$. Distances are expressed in units of the lattice constant a. We restore S.I. units in the formulas expressing measurable quantities.

II. QUANTUM PHASE TRANSITIONS

A quantum Josephson array consists of a regular network of superconducting islands weakly coupled by tunnel junctions. Thanks to submicron lithography, array's parameters (associated to the shape of the islands, the thickness of the oxide barrier,...) can be made uniform (virtually identical) across the whole array. With present-day technology variations in junction parameters are below 20 % across the array. The dimensions of the unit cell are of the other of few μm^2 while the superconducting islands have an area of about $1\,\mu$m^2. The largest samples consist of about 10000 junctions (e.g. 100 by 100 or 1000 by 7).

Quantum arrays are fabricated of all-aluminum high-quality Josephson tunnel junctions with a shadow-evaporation technique. The evaporation mask is made of electron sensitive resists in which the bottom resist layer has an undercut to ensure a proper lift-off after evaporation. Junctions are formed by evaporating a thin aluminum layer (25 nm) as the bottom electrode followed by in situ oxygen oxidation and evaporation of the counter electrode of about 50 nm from an opposite angle. A more detailed discussion of the fabrication techniques is presented in the Appendix A.

A. The model of a Josephson Junction Array

1. Quantum Phase Model

In Fig. 2, we show a scanning-electron-microscope (SEM) picture of a Josephson junction array. Its schematic representation is given in Fig. 3. In this square geometry the coordination number, z = 4. The coupling strength between adjacent islands is determined by the Josephson energy $E_J = \Phi_0 I_c/(2\pi)$. This coupling energy is inversely proportional to the normal-state junction resistance R_N. Experimentally R_N is determined from the normal-state array resistance r_N measured at 4.2 K, $R_N = (N+1) r_N M_y/M_x$, where M_y is the number of cells across the array and M_x is the number of cells along its length. The maximum junction critical current I_c, in the absence of charging effects and thermal fluctuations, is assumed to be given by the Ambegaokar-Baratoff value [28]

$$I_c R_N = \pi \frac{\Delta}{2e}$$

with the measured critical temperature T_c. For a BCS critical temperature $T_c = 1.35$ K one gets $I_c R_N$=0.32 mV at low temperatures.

Quantum effects in Josephson arrays come into play when the charging energy (associated with non-neutral charge configurations of the islands) is comparable with the Josephson coupling (the physics associated with charging effects in single normal and superconducting junctions has been reviewed in Refs. [10,11]). In addition, as explained in the introduction, the junction resistance should be of the order of (or larger than) R_Q [29].

Arrays are made in a planar geometry, in which each island is coupled to each of the other islands and to a far-away ground by its self-capacitance C_0. The junctions are made of two overlapping superconducting layers separated by a thin oxide layer and the main contribution to the capacitance therefore comes from the junction capacitance C. An estimate of the total island capacitance C_Σ is obtained from measuring the voltage offset (V_{offset}) in the I - V characteristics at high bias currents at T=10 mK in a magnetic field of 2 T. Using the so-called local rule [10,30], $C_\Sigma = Me^2/2V_{offset}$. For junctions of 0.01 μm^2, C_Σ is found to be 1.1 fF. If one identifies C with C_Σ, the specific capacitance is 110 fF/μm^2. Measurements on large-area junctions have yielded a specific capacitance that is about a factor of two lower. This discrepancy shows that stray capacitance (capacitance between next-nearest and further neighbors) may play a role in Josephson circuits as pointed out by Lu *et al.* [31]. However, for simplicity one often identifies the measured C_Σ as the junction capacitance C.

Reliable estimates of this self-capacitance (C_0)are obtained from separate measurements on small series arrays with high E_C/E_J ratio. A magnetic field of 2 Tesla is applied so that the series arrays are in the normal state; C_0 is then measured by varying the potential of the circuit with respect to the ground potential. Recording the current through the circuit yields a periodic signal with period e/C_0. For islands of 1 μm by 1 μm, $C_0 \approx 1.2\text{x}10^{-17}$ F which is much smaller than C [32].

As already mentioned, the electrostatic energy can be determined once the capacitance matrix C_{ij} and the gate voltages (if present) are known [30,33]. Generally one only considers the junction capacitance C and the capacitance to the ground C_0. In this case the capacitance matrix has the form $C_{ii} = C_0 + \text{z}C$, $C_{ij} = -C$ (if i, j nearest neighbors) and zero in all other cases. Consequently the charging energy (for two charges placed in islands i and j of coordinates $\mathbf{r}_i$ and $\mathbf{r}_j$ respectively) is given by

$$E_{ij}^{(ch)} = \frac{e^2}{2} C_{ij}^{-1} = \frac{e^2}{2} \int \frac{d\mathbf{k}}{4\pi^2} \frac{e^{i\mathbf{k}\cdot(\mathbf{r}_i - \mathbf{r}_j)}}{C_0 + 2C(1-\cos k_x) + 2C(1-\cos k_y)} \quad , \tag{1}$$

which is well approximated by the expression:

$$E_{ij}^{(ch)} \sim \frac{e^2}{4\pi C} K_0 \left(\frac{|\mathbf{r}_i - \mathbf{r}_j|}{\lambda} \right) \tag{2}$$

Here, K_0 is the modified Bessel function. The charging interaction increases logarithmically up to distances of the order of the screening length λ and then dies out exponentially. The characteristic energy scale is

$$E_C = \frac{e^2}{2C} \quad .$$

Equation (2) assumes three-dimensional screening and the range of the electrostatic interaction between Cooper pairs is given by (in units of the lattice spacing):

$$\lambda = \sqrt{C/C_0} \quad .$$

. If the two-dimensional limit is considered (if e.g. the array is sandwiched between two media with large dielectric coefficients) the screening length scales linearly with C/C_0 yielding a longer ranged interaction.

From all these considerations, we arrive at the following Hamiltonian which describes Cooper pair tunneling in superconducting quantum networks (quasi-particle tunneling is ignored at this stage). This model is frequently called the Quantum Phase Model (QPM) and is its most general form it is given by:

$$\begin{aligned} H &= H_{ch} + H_J \\ &= \frac{1}{2}\sum_{i,j}(Q_i - Q_{\mathrm{x},j})\, C_{ij}^{-1}\, (Q_j - Q_{\mathrm{x},j}) - E_J \sum_{<i,j>} \cos\left(\phi_i - \phi_j - A_{ij}\right) \ . \end{aligned} \tag{3}$$

The first term in the Hamiltonian is the charging energy in which the C_{ij}^{-1} is the capacitance matrix; the second is due to the Josephson tunneling. An external gate voltage $V_{\mathrm{x},i}$ gives the contribution to the energy via the induced charge $Q_{\mathrm{x,i}} = 2eq_{\mathrm{x}} = \sum_j C_{ij}V_{\mathrm{x,j}}$. This external voltage can be either applied to the ground plane or it may be (unintentionally) induced by trapped charges in the substrate. In this latter case $Q_{\mathrm{x,i}}$ will be a random variable.

A perpendicular magnetic field with vector potential $\mathbf{A}$ enters the Hamiltonian of Eq. (3) through $A_{ij} = 2e\int_i^j \mathbf{A}\cdot d\mathbf{l}$. The relevant parameter that describes the magnetic frustration is

$$f = (1/2\pi)\ \sum_P A_{ij}$$

where the summation runs over an elementary plaquette. In quantum arrays, the 2D flux penetration depth $\lambda_\perp(T) = \Phi_0/2\pi\mu_0 I_c(T)$ is much larger than the array size so that the magnetic field is essentially uniform over the whole array, i.e., f is position independent. A similar conclusion can be drawn by considering the ratio of the geometric inductance (we estimate it to be of the order of 1 pH) to the Josephson inductance (larger than 1 nH).

Throughout this review, two limits of the QPM are frequently discussed: $C \gg C_0$ and $C \ll C_0$. The former limit has already been discussed in detail as it is the appropriate regime of Josephson arrays. The latter limit is more appropriate for granular films that have a short-range Coulomb interaction. To describe these systems we use the following notation. When the on-site contribution is dominant, the characteristic energy is

$$E_0 = \frac{e^2}{2}C_{00}^{-1} \quad .$$

However, some properties (see e.g. discussion in Section II D) are crucially dependent on the details of the electrostatic energy at small distances, i.e., on weather the nearest-neigbor interaction is also included or not. E_1 represents the variable denoting this nearest-neigbor interaction; E_2 the interaction between next nearest-neighors and so on.

The two contributions in the Hamiltonian of Eq.(3) favor different types of ground states. The Josephson energy tends to establish phase coherence which can be achieved if supercurrents flow through the array. On the other hand the charging energy favors charge

localization on each island and therefore tends to suppress superconducting coherence. This interplay becomes evident if one recalls the Josephson relation (which here can be obtained at the operator level by calculating the Heisenberg equation of motion for the phase)

$$\frac{d\phi_i}{dt} = \frac{2e}{\hbar} V_i = \frac{2e}{\hbar} C_{ij}^{-1} Q_j \tag{4}$$

A constant (in time) charge on the islands implies strong fluctuations in the phases. On the other hand phase coherence leads to strong fluctuations in the charge.

The low-lying excitations of the model defined in Eq.(3), are long wave-length phase waves whose dispersion relation can be obtained by considering the QPM in the harmonic approximation

$$H \sim \frac{1}{2} \sum_{i,j} Q_i \, C_{ij}^{-1} \, Q_j - \frac{E_J}{2} \sum_{<i,j>} (\phi_i - \phi_j)^2 \ . \tag{5}$$

The dispersion relation of these modes (usually named spin-waves from the magnetic analogy of the Josephson coupling with the XY model) depends on the form of the capacitance matrix (see Section III B). The QPM possesses topological excitations as well, charges and vortices, that will be discussed in Section II B 3.

A qualitative understanding of the phase diagram can be obtained by considering the two limiting cases in which one of the two coupling energies is largest. For simplicity we look at the ground state of the system ignoring external voltages and magnetic field. If the Josephson term is dominant, the array minimizes its energy by aligning all the phases, i.e. it is in the superconducting state. If instead the charging energy is dominant, each island has a zero charge in the ground state. In order to put an extra charge on the island one has to overcome a Coulomb gap of the order of the charging energy (max E_C, E_0). The array behaves as an insulator although each island is still in the superconducting state.

2. Dissipative Models

Since the seminal paper by Caldeira and Leggett [36,37] it became clear that dissipation changes the quantum dynamics of macroscopic systems. One can therefore ask the question to what extent dissipation plays a role in Josepson-junction arrays and what its role is on the SI transition in quantum arrays. At low temperatures one expects quasi-particle tunneling not to be present since the charging energy is smaller than the superconducting gap Δ. Experiments on small arrays indicate that even at mK-temperatures a small but finite amount of quasi-particles is always present, although it has not been possible to discriminate the exact details of dissipation. Therefore, we treat the various models that have been proposed to describe dissipation in superconducting networks.

The QPM defined in Eq.(3) only accounts for Cooper pair tunneling between neighboring islands and needs to be generalized. The appropriate description is formulated in terms of an effective action by the authors of Ref. [10,38]:

$$Z = \int \prod_i D\phi_i(\tau) \exp[-S\{\phi\}] \tag{6}$$

The Euclidean effective action $S\{\phi\}$, corresponding to the Hamiltonian of Eq.(3) has the form (for simplicity we ignore charge and magnetic frustration for the time being)

$$S[\phi] = \int_0^\beta d\tau \left\{ \frac{C_0}{8e^2} \sum_i (\dot{\phi}_i)^2 + \frac{C}{8e^2} \sum_{\langle ij \rangle} (\dot{\phi}_i - \dot{\phi}_j)^2 - E_J \sum_{\langle ij \rangle} \cos(\phi_i - \phi_j) \right\} \tag{7}$$

with β being the inverse temperature. The first two terms are easily recognized as charging energies expressed in terms of voltages (see Eq.(4)). In the presence of dissipative tunneling, the effective action has a Caldeira-Leggett form and acquires an additional term

$$S_D[\phi] = \frac{1}{2} \int_0^\beta d\tau d\tau' \sum_{<ij>} \alpha(\tau - \tau') F(\phi_{ij}(\tau) - \phi_{ij}(\tau')) \tag{8}$$

where $\phi_{ij} = \phi_i - \phi_j$. Both the dissipative kernel $\alpha(\tau)$ related to the $I - V$ characteristic of tunnel junctions [10], and the function $F(\{\phi\})$ depend on the nature of the dissipation. Various mechanisms: tunneling of quasi-particles and/or the flow of Ohmic currents through the substrate or between the junctions themselves [20,35].

For an Ohmic junction, as is the case when the bath is formed by quasi-particle excitations in normal metals (or gapless superconductors), the kernel is

$$\alpha(\tau) = \frac{\pi}{2e^2 R_N} \frac{1}{\beta^2} \frac{1}{\sin^2(\pi\tau/\beta)}$$

Here, the normal-state resistance R_N controls the coupling to the environment [39]. For ideal superconducting islands on the other hand, the BCS gap inhibits leakage currents at small voltages and as a consequence the dissipative kernel is short range in imaginary time. Therefore, quasi-particle tunneling results in a renormalization of the junction capacitance [38]

$$C \longrightarrow C + \frac{3\pi}{32\Delta R_N} \quad . \tag{9}$$

The dissipation mechanism also affects the form of the function $F(\phi)$ in Eq. (8). If normal-electron tunneling occurs via discrete charge transfer, as it is for a quasi-particle current, $F(\phi)$ is a periodic function of the phase ϕ

$$F_{QP}(\phi_{ij}(\tau) - \phi_{ij}(\tau')) = 1 - \cos\left(\frac{\phi_{ij}(\tau) - \phi_{ij}(\tau')}{2} \right) \quad . \tag{10}$$

If, on the contrary, dissipation is due to normal shunts or more generally to the interaction with the electromagnetic environment, F is quadratic in ϕ

$$F_N(\phi_{ij}(\tau) - \phi_{ij}(\tau')) = \frac{1}{2} \left(\frac{\phi_{ij}(\tau) - \phi_{ij}(\tau')}{2} \right)^2 \tag{11}$$

indicating that the charge at a junction can assume continuous values.

One can also consider dissipation due to currents flowing to the substrate. This local-damping model plays an important role in classical, proximity coupled Josephson arrays. Voltage fluctuations compared to the ground instead of voltage differences between junctions

are the crucial variables: the dissipative part of the action now depends on the phase ϕ_i of each island and not on the phase difference ϕ_{ij}

$$F_{LD}(\phi_i(\tau) - \phi_i(\tau')) = \frac{1}{2}\left(\frac{\phi_i(\tau) - \phi_i(\tau')}{2}\right)^2 \quad . \tag{12}$$

The path integration in Eq.(6) depends on the nature of dissipation mechanism and it is related to the charge on the islands being a continuous or discrete variable [10]. In the first case, the phase is considered an extended variable and in the path integral $\phi_i(0) = \phi_i(\beta)$. If the charge is a discrete variable, a summation over winding number is implied in Eq.(6)

$$\int D\phi \longrightarrow \prod_i \int_0^{2\pi} d\phi_{i0} \sum_{\{m_i=0,\pm1,\ldots\}} \int_{\phi_{i0}}^{\phi_{i0}+2\pi m_i} D\phi_i(\tau) \; . \tag{13}$$

These non-trivial boundary conditions express the fact that the charges of the grains are integer multiples of $2e$.

The dissipative coupling strength is usually expressed in the form $\alpha = R_e/R_Q$. The exact value of the effective resistance R_e is not a priori clear. Consider an array of unshunted tunnel junctions. If thermally excited quasi-particles were the only source of damping, a measure of R_e would be the subgap resistance which is many orders of magnitude larger than the normal-state resistance R_N. However, measurements hint at a much smaller R_e that is closer to R_n. The exact mechanism is not clear but one should always keep in mind that Josephson junctions are highly nonlinear elements. Some coupling to higher energy scales may therefore occur and R_e is smaller than the subgap resistance but not lower than R_N. This coupling may for instance occur when a vortex crosses a single junction thereby producing voltage spikes. Throughout this review, we keep the notation simple and use α to denote the dissipation strength regardless of the underlying dissipation mechanism. Its origin will be specified from case to case.

3. Related Models

The S-I transition has been investigated by studying model Hamiltonians, the so called Bose-Hubbard and XXZ models, closely related to the QPM of Eq.(3). We follow the notation used currently in the literature and point out the connection with the couplings used to defined the QPM. The Bose-Hubbard (BH) model [40] is defined as

$$H = \frac{1}{2}\sum_i n_i U_{ij} n_i - \mu \sum_i n_i - \frac{t}{2}\sum_{\langle ij \rangle}(e^{-iA_{ij}}\; b_i^\dagger b_j + h.c.) \tag{14}$$

Here, $b^\dagger, b$ are the creation and annihilation operators for bosons and $n_i = b_i^\dagger b_i$ is the number operator. U_{ij} describes the Coulomb interaction between bosons ($U_{ij} \longrightarrow E_{ij}^{ch}$), μ is the chemical potential, and t the hopping matrix element. The connection between the Bose-Hubbard model and the QPM is easily seen by writing the field b_i in terms of its amplitude and phase and by subsequently approximating the amplitude by its average. This procedure leads to the identification $b_i \sim e^{i\phi_i}$. The hopping term is then associated with the Josephson tunneling ($< n > t \longrightarrow E_J$) while the chemical potential plays the same role as the external

charge in the QPM ($\mu \longrightarrow Q_x$). The mapping becomes more accurate as the average number of bosons per sites increases.

In the case of strong on-site Coulomb interaction $U_{ii} \to \infty$ and very low temperatures only few charge states are important. If the gate voltage is tuned close to a degeneracy point, the relevant physics is captured by considering only two charge states for each island, and the QPM is equivalent to an anisotropic XXZ spin-1/2 Heisenberg model [41,42]

$$H_S = -h \sum_i S_i^z + \sum_{i \neq j} S_i^z \; U_{ij} \; S_j^z - E_J \sum_{\langle i,j \rangle} \left(e^{iA_{ij}} \; S_i^+ \; S_j^- + e^{-iA_{ij}} \; S_j^+ \; S_i^- \right) \; . \tag{15}$$

The operators S_i^z, S_i^+, S_j^- are the spin-1/2 operators, S_i^z being related to the charge on each island ($q_i = S_i^z + \frac{1}{2}$), and the raising and lowering $S_i^{\pm}$ operators corresponding to the "creation" and "annihilation" operators $e^{\pm i\phi_j}$ of the QPM. The "external" field h is related to the external charge by $h = (q_{\rm x} - 1/2) \sum_j U_{ij}$. Different magnetic ordered phases of the XXZ Hamiltonian correspond to the different phases in the QPM. Long-range order in $\langle S^+ \rangle$ indicates superconductivity in the QPM while long-range order in $\langle S^z \rangle$ describes order in the charge configuration (Mott insulator).

The three models are equivalent in the sense that they belong to the same universality class (they lead to the same Ginzburg-Landau effective free energy). The non-universal features like the location of the phase transitions, the shape of the phase diagram (and sometimes the very existence of some intermediate phase) depend quantitatively on the specific choice of the model. A more rigorous discussion of the different dynamical algebras realized by the three models can be found in Refs. [43–47].

A generalization of these models to the case in which amplitude fluctuations are coupled to phase fluctuations was discussed in Ref. [48]. Very recetly Yurkevich and Lerner [49] developed a nonlinear sigma model description of granular superconductors that reduces to the BH model in the limit in which amplitude fluctuations are ignored.

B. The zero-field phase diagram

Superconductor-Insulator transition has been investigated in great details in JJAs [50–53] as well as in granular systems [54–60] and uniform ultra-thin films [61–63]. The first controlled measurements on the S-I transition in junction arrays have been carried out by Geerligs *et al.* [50]. Part of the data of Ref [50] together with the new data of Ref. [51] are presented in Fig. 4. It shows the resistive behavior of six different square arrays in zero magnetic field. The zero-bias resistance per junction $R_0(T)$ has been measured with a very small transport bias (current per junction smaller than $< 10^{-3} I_c$) in the linear part of the current-voltage characteristics. Three arrays become superconducting; two arrays insulating and one array that lies very close to the S-I transition shows a doubly reentrant dependence. The horizontal dashed line in Fig.4 is the critical resistance value of $8R_Q/\pi$ (see Eq.(44)).

For the three arrays that become superconducting, the data are fitted to the predicted BKT square-root cusp dependence on temperature,

$$R_0(T)/R_N = c \exp(-b[E_J/(T - T_J)]^{1/2})$$

with b and c constants of order one. In order to compensate for the temperature dependence of E_J, it is convenient to define a normalized temperature is defined as $T/E_J(T)$. From the

fits the normalized BKT transition temperature T_J is determined. Near the S-I transition T_J is substantially smaller than the classical value of $0.90E_J$. Note that at low resistance levels ($R_0(T) < 10^{-3}R_N$), deviations from the square-root cusp dependence are found and that the resistance decreases exponentially. This is indicative of thermal activation of single vortices across the whole array width [64].

The two arrays with a ratio of $E_J/E_C \leq 0.55$ show a continuous increase of the resistance as the temperature is lowered, i.e., the arrays become insulating at zero temperature despite the fact that each island is still superconducting with a well developed BCS gap! It has been proposed that, due to the long range interaction between the charges, the conductance will follow a square-root cusp dependence on temperature in a similar way as the resistance for the superconducting samples. This square-root cusp dependence characteristic for a charge-BKT transition is generally not observed. Instead the conductance decreases exponentially as temperature is lowered. This issue will be discussed in some details in the section devoted to the BKT transition (section II.B.4).

The resistance of sample with $E_C/E_J = 1.7$ has a very remarkable dependence on temperature. Starting at high temperatures, $R_0(T)$ first decreases when the temperature is lowered. Below T=150 mK, however, $R(T)$ increases by more than three orders of magnitude and at the same time a charging gap develops in the I-V curve. Finally at 40 mK, $R_0(T)$ starts to decrease again. The second reentrant transition at 40 mK seems to be a more general feature of arrays near the S-I transition which is also present in a magnetic field.

Reentrant behavior in the resistance has also been observed in granular superconductors. Already in the early theoretical works on the QPM various explanations have been proposed. We will summarize some of the ideas. Efetov [65] suggested that the thermally excited quasi-particles could screen the Coulomb energy thereby lowering the threshold for the onset of phase coherence. Stimulated by Efetov's work a number of theoretical papers showed that a reentrant phase boundary can be obtained in the QPM however it turned out that the very existence of the re-entrance was sensitive to the approximation scheme used. Moreover it was shown that even if there is no re-entrance in the phase diagram, the QPM leads to a fluctuation dominated region [66–68] which may account for the observed re-entrance. Many physical ingredients not contained in the QPM (random offset, dissipation,...) may play a role as well. Recently Feigelman *et al.* [69] proposed that the parity effects may be responsible. At intermediate temperatures the screening of quasi-particles would decrease the effective Coulomb interaction (and therefore the resistance). At lower temperatures screening disappears due to the excess free energy associated with odd grains, leading to an upturn of the resistance curve.

The data of Fig.4 can be used to construct a phase diagram for phase transition of Josephson arrays in zero-magnetic field [51] as shown in Fig. 5. In this figure the superconducting-to-normal phase boundary is the vortex-BKT phase transition. Temperature on the vertical axis in this figure is given in units of E_J and scaled to the classical (in absence of charging effects) BKT transition $T_J^{(0)}$. The experimental value $T_J^{(0)} = 0.95E_J$ is close to the theoretical value of 0.90 determined from Monte Carlo simulations. On the insulating side of the figure no strict phase transition was observed. The dashed line therefore is somewhat arbitrary. It represents the crossover to the low-temperature region with $R_0 > 10^3 R_N$. Fig.5 indicates that at zero temperature the S-I transition takes place at $E_C/E_J \approx 1.7$.

The existence of a zero temperature (quantum) phase transition can be understood by simple arguments as already discussed in the previous section. Mean-field [70], variational approaches [71–73], 1/z expansion [74], Monte Carlo simulations [75,76] and cluster expansions [77] were also applied to the QPM model of Eq. (3). We refer the reader to the various articles for a discussion and comparison. Here, we present a few approaches that give a self-contained description of the phase diagram. We start with the mean-field calculation. Inaccurate in determining the critical behavior, this approach is yet capable to capture most of the features measured in the experiments. We first consider the case in which both charge and magnetic frustration are absent. Note that for the time being, dissipation is not included. It will be considered in detail in Section II E.

1. Mean-Field approach

The mean-field decoupling consists in approximating the Hamiltonian of Eq.(3) by [65,70]

$$H_{\rm MF} = \frac{1}{2}\sum_{i,j} Q_i C_{ij}^{-1} Q_j - {\rm z}E_J \langle \cos\phi \rangle_{\rm MF} \sum_j \cos\phi_j \ .$$

The average $\langle \cos(\phi) \rangle_{\rm MF}$ plays the role of the order parameter and it should be calculated self-consistently

$$\langle \cos(\phi) \rangle_{\rm MF} = {\rm Tr}\left\{ \cos(\phi_i) \exp(-\beta H_{\rm MF}) \right\} / {\rm Tr}\left\{ \exp(-\beta H_{\rm MF}) \right\} \ .$$

Close to the transition point the thermal average on the r.h.s can be evaluated by expanding it in powers of $\langle \cos(\phi) \rangle_{\rm MF}$ (This can be done because the transition is continuous). The transition line is determined by the equation

$$1 - {\rm z}E_J \int_0^\beta d\tau \langle \cos\phi_i(\tau) \cos\phi_i(0) \rangle_{ch} \ = 0 \tag{16}$$

where the average $< ... >_{ch}$ is calculated using the eigenstates of the charging part of the Hamiltonian only. Note that the (imaginary) time evolution of the phase is due to charging as well.

In the classical limit the phase correlator is unity (there are no quantum fluctuations) and the mean-field transition temperature is ${\rm z}E_J/2$. Charging effects inhibit phase fluctuations and the critical temperature decreases. Explicit formulas for the phase-phase correlator are given in Appendix C. At $T = 0$ in the self-charging limit ($E_{ij}^{(ch)} = E_0 \delta_{ij}$) the correlator reads

$$\langle \cos\phi_i(\tau) \cos\phi_i(0) \rangle_{ch} = \frac{1}{2} \exp\{ -4\tau E_0 (1 - \tau/\beta) \} \ .$$

By substituting this expression in Eq.(16) one gets a value for the S-I transition which coincides with the simple estimate based on energy considerations.

The detailed structure of the phase diagram depends, even in the absence of (magnetic or electric) external frustration, on the range of the electrostatic energy. The phase diagram in the short-range case is sketched in Fig.6. Very recently a detailed analysis of the dependence of the phase boundary on the form of the capacitance matrix has been performed in Ref. [78] using perturbation theory and numerical simulations.

For two-dimensional arrays the transition to the superconducting state is of the BKT type with no spontaneous symmetry breaking. Quantum fluctuations renormalize the value of the transition temperature but do not change the universality class of the transition. The corrections to the BKT transition due to quantum fluctuations have been evaluated in a semi-classical approximation in Ref. [79]. For $E_J >> E_C$, the JJA behaves as a classical XY model but with a renormalized E_J. This approach breaks down when quantum fluctuation drive the transition to zero. At zero temperature there is a dimensional crossover and the S-I transition belongs to the $(d+1)$-XY universality class.

2. Coarse-Graining approach

Although it is very useful in determining the structure of the phase diagram, the mean-field approach has various shortcomings. For a more accurate description of the quantum critical regime one has to resort to different approaches. Universality implies that the critical behavior of the system depends only on its dimensionality and on the symmetry which is broken in the ordered phase. Many properties of JJAs can be extended to other systems that show a S-I transition. By using the coarse-graining approximation it is possible to go from the QPM model to a Ginzburg-Landau model with an effective free energy which is a function of the order parameter [80,81] only. Since the transition is governed by quantum fluctuations, the order parameter depends both on space and (imaginary)-time [13,82].

The coarse-graining proceeds in two steps:

- An auxiliary field $\psi(x,\tau)$ (which has the role of the order parameter) is introduced through a Hubbard-Stratonovich transformation. The partition function is then expressed as a path integral over ψ.
- The assumption that the order parameter is small close to the transition allows for a cumulant expansion to obtain the appropriate Ginzburg-Landau free energy. The coefficients depend on the details of the microscopic model.

The partition function of the QPM is given by

$$Z = Tr\{e^{-\beta H_{\rm QPM}}\} = Z_{ch}\langle T_\tau e^{-\int_0^\beta d\tau H_J(\tau)}\rangle_{ch} \tag{17}$$

where the subscripts ch and J refer to the charging and Josephson part of the Hamiltonian in Eq.(3). By applying the Hubbard-Stratonovich transformation to the Josephson term one gets (in absence of magnetic and charge frustration)

$$\exp\left\{\frac{E_J}{2}\int_0^\beta d\tau \sum_{\langle i,j\rangle} e^{i\phi_i}e^{-i\phi_j} + h.c.\right\}$$

$$\sim \int D\psi^* D\psi \exp\left\{-\int_0^\beta d\tau \sum_{i,j}[E_J]^{-1}_{ij}\psi_i^*(\tau)\psi_j(\tau) + \int_0^\beta d\tau \sum_i \left[\psi_i^*(\tau)e^{i\phi_i(\tau)} + h.c.\right]\right\} \tag{18}$$

Here we introduced a matrix $[E_J]_{ij}$ which is equal to E_J if i and j are nearest neighbors and zero otherwise. The partition function can be written as

$$Z = Z_{ch} \int D\psi^* D\psi \exp\left\{-F[\psi]\right\} \tag{19}$$

Close to the phase transition one can perform a gradient expansion:

$$F = \sum_{\langle i,j \rangle} \int d\tau d\tau' \psi_i(\tau) \left[[E_J]^{-1}_{ij} \delta(\tau - \tau') - g(\tau - \tau') \delta_{ij} \right] \psi^*_j(\tau') + \kappa \sum_i \int d\tau |\psi_i(\tau)|^4 \ . \tag{20}$$

The dynamics of the field ψ is governed by the phase-phase correlator

$$g(\tau - \tau') = \langle \exp[\phi_i(\tau) - \phi_i(\tau') \rangle_{ch}$$

that was already encountered in Eq.(16). The coefficient κ is related to the four-point phase correlator.

The partition function in Eq.(19) can be calculated using a mean-field approximation for the phase by evaluating it in the saddle point approximation. The results coincide with that of the previous subsection. In the coarse-graining approach, however, a systematic treatment of the fluctuations is possible and it allows to study transport as well. In the case of zero offset charges and zero external magnetic field, by expanding the phase correlator around the zero-frequency and zero-momentum value, the quadratic part of Eq.(20) can then be rewritten as

$$F^{(0)}[\psi] = T \sum_{\mathbf{k}, \omega_n} \left[\epsilon + \gamma k^2 + \zeta \omega_n^2 \right] |\psi(\mathbf{k}, \omega_n)|^2$$

where, using the expression given in Appendix C, the coefficients can be expressed as:

$$\begin{aligned} \epsilon &= \frac{g^{-1}(\omega_n = 0)}{2E_0} - \frac{E_J}{E_0} \\ \gamma &= \frac{g^{-1}(\omega_n = 0)}{8E_0} \\ \zeta &= \frac{\partial^2_{\omega_n} g(\omega_n) \mid_{\omega_n = 0}}{4E_0} \quad . \end{aligned} \tag{21}$$

At $T = 0$, this system belongs to the same universality class as the $(d+1)$ XY model. One can readily obtain all the critical exponents from what is know from the XY model [83]. The dynamical critical exponent is $z = 1$ due to the symmetry between space and time. At finite temperatures the transition belongs to the Berezinskii-Kosterlitz-Thouless universality class and there is no spontaneous breaking of the symmetry. The dynamical critical exponent and the dimensional crossover is modified in the case of $1/r$-Coulomb interaction between charges [84].

3. Duality transformations

Duality transformations have proven to be a powerful tool in field theory and statistical mechanics [85]. The idea behind it is that the weak coupling region of a particular system can be mapped onto the strong coupling range (and vice versa). The symmetries of the system under this transformation lead to important insight into the structure of the model, especially in the region of intermediate couplings which is usually elusive to standard treatments. Dual

transformations constitute a powerful approach since it is possible to recast the partition function solely in terms of the topological excitations of the system [86–89].

In this section we derive some properties of quantum JJAs derived from duality. There is a dual transformation [90–92] relating the classical vortex limit, $E_J \gg E_C$, to the opposite charge limit, $E_J \ll E_C$. The situation is most transparent in the case $C_0 \ll C$, which might be more relevant for arrays. The interaction between charges on islands is then logarithmic, analogous to vortex interactions in classical, superconducting arrays. The charges form a 2D Coulomb gas and are expected to undergo a BKT transition at $T_{ch}^{(0)} \sim E_C$ [93] (see also next subsection).

Using the results discussed in Appendix D, the partition function of a JJA can be expressed as a sum over charge q and vortex v configurations

$$Z = \sum_{[q,v]} e^{-S\{q,v\}} \ . \tag{22}$$

The effective action $S\{q,v\}$ reads

$$S\left\{q,v\right\} = \int_0^\beta d\tau \sum_{ij} \quad \Big\{ 2e^2 q_i(\tau) C_{ij}^{-1} q_j(\tau) + \pi E_J v_i(\tau) G_{ij} v_j(\tau) + i\ q_i(\tau)\Theta_{ij}\dot{v}_j(\tau) + \frac{1}{4\pi E_J}\dot{q}_i(\tau) G_{ij}\dot{q}_j(\tau) \Big\} . \tag{23}$$

This action describes two coupled Coulomb gases. We have used a continuous time notation for clarity. Since q and v are integer valued fields, the path integral is well defined on a discretized time expression. The charges interact via the inverse capacitance matrix (first term). The interaction among the vortices (second term) is described by the kernel G_{ij}, which is the Fourier transform of k^{-2}. At large distances $r_{ij} \gg a$ between the sites i and j it depends logarithmically on the distance:

$$G_{ij} \sim -\frac{1}{2}\ln r_{ij}.$$

The third term describes the coupling between the topological excitations in the two limits, i.e., it describes the coupling between charges and vortices. The function

$$\Theta_{ij} = \arctan\left(\frac{y_i - y_j}{x_i - x_j}\right)$$

represents the vortex-phase configuration at site i when its center is placed at the site j. The coupling has a simple physical interpretation: a change of vorticity at site j produces a voltage at site i which is felt by the charge at this location. The last term $\dot{q}G\dot{q}$ stems from the spin-wave contribution to the charge-correlation function. In the limit in which $E_J \to 0$ or $E_C \to 0$ the action for a classical system of Cooper pair charges or vortices is recovered.

The effective action in Eq.(23) shows a high degree of symmetry between the vortex and charge degrees of freedom. In particular, in the limit $C_0 \ll C$ the inverse capacitance matrix has the same functional form as the kernel describing vortex interactions:

$$e^2 C_{ij}^{-1} = \frac{E_C}{\pi} G_{ij} \ .$$

Hence charges and vortices are dual. There is a critical point for which the system is self-dual with respect to interchanging them:

$$\frac{E_J}{E_C} = \frac{2}{\pi^2}$$

The duality is strict for vanishing self-capacitance and in the absence of the spin-wave duality breaking term $(\dot{q}G\dot{q})$ in Eq.(23). This latter term is irrelevant at the critical point, i.e., it merely shifts the transition point. However, it has important implications for the dynamical behavior.

Duality transformations have also been applied to a three-dimensional JJA consisting of two 2D arrays placed on top of each other [94–96]. The authors of these papers assume that there is only capacitive coupling between them (no Josephson coupling). The most interesting situation arises when one array is in the quasi-classical (vortex) regime while the other is in the quantum, charge regime. Then, vortices in one layer and charges in the other one are well-defined.

The Euclidean effective action, in term of phases, $S\{\phi_1, \phi_2\}$ has the form

$$S\{\phi_1,\phi_2\} = \int_0^\beta d\tau \sum_{\mu=1,2}$$
$$\left\{ \sum_i \left[\frac{C_{0\mu}}{8e^2}(\dot{\phi}_{i\mu})^2 + \frac{C_{\rm x}}{8e^2}(\dot{\phi}_{i1} - \dot{\phi}_{i2})^2 \right] + \sum_{\langle ij \rangle} \left[\frac{C_\mu}{8e^2}(\dot{\phi}_{i\mu} - \dot{\phi}_{j\mu})^2 - E_{J\mu}\cos(\phi_{i\mu} - \phi_{j\mu}) \right] \right\} \qquad (24)$$

where $C_{0\mu}$ are the island capacitances in array μ relative to ground, C_μ are the junction capacitances in the array μ, and $C_{\rm x}$ are the interlayer capacitances between islands on top of each other, while $E_{J\mu}$ are the Josephson coupling constants in the layers. Similar as in a single array, we move from a description in terms of phases to one in terms of charges and vortices, and use the duality of the resulting action to investigate the transition.

Before we proceed with the calculation it is necessary to stress that in the regime of interest the interlayer capacitances $C_{\rm x}$ not only couple the layers, but also renormalize the island capacitances C_{01} and C_{02} to ground. The physical reason for this is that due to the strong fluctuations of charges in layer 2 and vorticities in layer 1 these variables are effectively continuous, and hence a coupling to the other array plays the same role as a coupling to ground. Due to screening, the interaction between charges in each layer has a finite range for any non-zero $C_{\rm x}$, and the BKT transition is replaced by a crossover. However, in the limit $C_{01} \ll C_{\rm x} \ll C_1$ the screening length $\xi_1 \sim (C_1/C_{\rm x})^{1/2}$ can be large enough to make it meaningful to speak about the charge-unbinding transition (the transition is exponentially sharp). Below we consider this case. For not so weak coupling, on the other hand, this description becomes meaningless, since the crossover is strongly smeared, and the insulating phase is absent.

It is possible to introduce vortex degrees of freedom in the same way as for one array. We obtain the effective action for charges $q_{i1}(\tau)$ in layer 1 and vorticities $v_{i2}(\tau)$ in layer 2 (to be referred below as q_i and v_i)

$$S\{q,v\} = \int_0^\beta d\tau \left\{ \frac{2E_{C1}}{\pi} \sum_{ij} q_i(\tau) G_{ij} q_j(\tau) + \frac{1}{4\pi E_{J1}} \sum_{ij} \dot{q}_i(\tau) G_{ij} \dot{q}_j(\tau) + \pi E_{J2} \sum_{ij} v_i(\tau) G_{ij} v_j(\tau) \right.$$

$$+\frac{\pi}{8E_{C2}}\sum_{ij}\dot{v}_i(\tau)\Big[G_{ij}-\frac{C_{\rm x}^2}{4\pi^2C_1C_2}\sum_{kl}\Theta_{ik}G_{kl}\Theta_{lj}\Big]\dot{v}_j(\tau)+\frac{iC_{\rm x}}{2\pi C_1}\sum_{ijk}\dot{v}_i(\tau)\Theta_{ik}G_{kj}q_j(\tau)\Big\}. \quad (25)$$

This equation looks rather similar to the effective charge-vortex action in one Josephson junction array (see Eq.(23)). The most important difference is that while in one layer either charges or vortices are well-defined degrees of freedom, Eq. (25) describes the system of two *well-defined* dynamic variables on each site – the charges in layer 1 and the vortices in layer 2. The action shows a duality between charges and vortices (the second term in the square brackets is small for $C_{\rm x} \ll C_1, C_2$). Both kinetic terms for charges and vortices violate the duality due to the numerical coefficients. However, close enough to the transitions these terms only produce a small renormalization of the transition temperature, and are therefore irrelevant. Another interesting feature of this action is that the last term, describing the interaction between charges and vortices, is also small, while in a single-layer array the interaction is always of the same order of magnitude as the other terms.

4. Berezinskii-Kosterlitz-Thouless transitions

In classical arrays, it is well established that JJAs undergo a BKT phase transition to the superconducting state. In the opposite limit where charging dominates, quantum fluctuations of the phases are strong, and vortices are ill-defined objects. In this regime the duality transformations discussed in the previous section show that charges on the islands are the relevant variables. Similarly to vortices in classical arrays, they interact logarithmically with each other and are expected to undergo a charge-BKT transition leading to insulating behavior [93].

A critical point separates the superconducting and insulating regime at $T = 0$. As discussed before, the various models give different estimates for the value of the critical point, but in all cases it lies close to $E_J/E_C \sim 1$. The theoretical phase diagram in the limit of logarithmically interacting charges is shown in Fig.7. For any $T \neq 0$ the array has three phases. Next to the superconducting and insulating phase, there is a region with normal conduction. Here, there are always some free vortices/charges present as they are generated by thermal or quantum fluctuations. Experimental verification of this diagram has been reported in Refs. [97,98] In the remainder of this subsection, we discuss the experimental aspects of BKT transitions in arrays.

The BKT transition in the classical case has been studied in great detail (see e.g. Refs. [2,3]). On approaching the critical point of the S-I transition, the vortex-BKT transition temperature is lowered by quantum fluctuations. For $C_0 = 0$ the shift of the transition temperature is [76,99]

$$T_J = \frac{\pi E_J}{2}\left(1-\frac{4}{3\pi}\frac{E_0}{E_J}\right) \quad . \quad (26)$$

A reduction of the transition temperature is generally observed in quantum arrays. The Delft data (shown in Fig. 4), however, show that with increasing E_C/E_J ratio the reduction of the transition temperature goes faster than predicted above (Eq. (26).

On the charging side ($E_J \ll E_C$) of the phase diagram, the charge-BKT transition occurs at a temperature [91]

$$T_{ch} = \frac{E_C}{\pi} - 0.31\frac{E_J^2}{E_C} \ .$$

Note that the charge-BKT transition exists for both arrays with superconducting and normal islands [100].

The existence of a charge-BKT transition implies that arrays are insulating below the transition temperature. The conductance should vanish with a characteristic square-root dependence according to

$$G \sim R_N^{-1} \exp\left\{-2b\left[T/T_{ch} - 1\right]^{-1/2}\right\} \tag{27}$$

where the constant $b \sim 1$. The temperature dependence of the conductance in the charge regime has been investigated by several groups [101–103]. Instead of the predicted square-root cusp behavior, an exponential (activated) temperature dependence

$$G \sim R_N^{-1} \exp\left\{-E_a/T\right\}$$

has been observed with an activation energy

$$E_a \sim \Delta + 0.24E_C \quad .$$

In arrays the screening length is about 10^2 lattice constants and therefore there is no a priori reason for observing such dramatic deviations from the BKT theory. Recently, Feigelman *et al.* [69] re-examined the problem and found that parity effects together with the screening of the Coulomb interaction due to thermally activated quasi-particles is responsible for masking the charge-BKT transition. At temperatures above a crossover temperature T^* where parity effects [104] set in, the presence of quasi-particles rules out the possibility to observe the charge-BKT transition. If the BKT transition temperature is larger than the crossover temperature, the array behaves as a normal one and a charge BKT transition occurs associated with the unbinding of quasi-particles at temperatures close $E_C/4\pi$. The presence of free charges screens the interaction between Cooper pairs resulting in the unbinding of pairs. The resistance as calculated by Feigelman *et al.* [69] is expected to be

$$\ln\frac{R(T)}{R(E_C/4\pi)} \sim \min\left[\frac{F_P(T)}{T - E_C/4\pi}, \frac{b}{\sqrt{4\pi}}\left(\frac{E_C}{T - E_C/4\pi}\right)^{1/2}\right]$$

where $F_P(T)$ is the free energy difference between islands with an even and an odd number of electrons [104]. From analogous considerations one may conclude [69] that normal arrays are better suited for studying the charge unbinding transition.

C. Magnetic frustration

When in the classical limit ($E_C << E_J$) a perpendicular magnetic field is applied, vortices enter the array above a certain threshold field [64]. Just as in films, the vortex density increases with increasing magnetic field. In junction arrays the periodic lattice potential,

however, prevents vortices to move at low temperatures. Only above the depinning current, vortices move (flux-flow branch). The resistance in this branch increases approximately linearly with $f = \Phi/\Phi_0$ up to $f \sim 0.2$ (Φ is the magnetic flux piercing through an elementary plaquette). A phenomenological model, analogous to the Bardeen-Stephen model used to describe flux-flow in films, is in good agreement with experiments providing that coupling between spin waves and vortices is taken into account (see section III.C) The properties of arrays at low frustration (low vortex densities) are dominated by single-vortex properties and are the subject of the next chapter.

In larger magnetic fields commensurability effects come into play and the behavior of junction arrays is richer than that of films. A magnetic field applied perpendicularly to the array leads to frustration [106]. The presence of the magnetic field induces vortices in the system and if the frustration is a rational number, $f = p/q$, the ground state consists of a checkerboard configuration of vortices with a $q \times q$ elementary cell. The stability of the vortex lattice against a bias current leads to a decrease in the small-bias resistance at finite fractional fillings. In order of their relative strength, one expects dips at $f = 1/2, 1/3, 1/4, 2/5, ...$ in square arrays and at $f = 1/2, 1/4, 1/3, 3/8, ...$ in triangular arrays as is illustrated in Fig.8. Near these fractional values of f, defects from the ordered lattice (excess single vortices or domain walls) are believed to determine the array dynamics in a similar way as the field induced vortices determine array dynamics near $f = 0$. Therefore, arrays near commensurate values with high stability such as $f = 1/2$ may qualitatively behave in a similar way as near zero magnetic field. Because all properties are periodic in f with period $f = 1$ an increase beyond $f = 1/2$ does not lead to new physics.

A particularly interesting case is the fully frustrated situation ($f = 1/2$) in square arrays. The two degenerate ground states consist of a vortex lattice with a 2×2 elementary cell. The current corresponding to this vortex arrangement flows either clockwise or anti-clockwise in each plaquette (chiral ground state). Interaction between domain wall excitations with $1/4$ fractionally charged vortices (at the corners of a domain wall) and excess single integer vortices are believed to trigger a combined BKT-Ising transition. A fully frustrated array has two critical temperatures related to the Z_2 and $U(1)$ symmetries of the problem. Their existence has been investigated both by analytical methods and Monte Carlo simulations. Even at the classical level, the complete scenario is not fully understood yet. There is numerical evidence either supporting the existence of two very close critical temperatures with critical behavior typical of Ising and BKT transitions respectively or the existence of a single transition with novel critical behavior. Further reference to classical frustrated arrays can be found in Ref. [107].

At the mean-field level the full phase-diagram including charging effects and magnetic fields is obtained by solving an eigenvalue problem equivalent to the Hofstadter problem [108]. The resulting phase boundary as a function of vorticity shows commensurability effects. Although the superconducting transition temperature is reduced, the average configuration of the phases and the supercurrent flow patterns are unchanged. The ground state is still chiral [109]. More detailed calculations based on expansion in E_J/E_0 of the QPM [110] and on the BH model [111] confirm the butterfly-like behavior of the S-I transition. In Fig.9 the theoretical results obtained by Kim *et al.* [110] are shown.

As in the unfrustrated case, measurements indicate a S-I transition at $T = 0$. For the same set of samples as presented in Fig.4 the S-I transition for $f = 1/2$ has been studied.

The phase diagram is shown in Fig.10. The transition takes place very close to a normal-state resistance of 11 kΩ. The critical E_C/E_J ratio is about 1.2, a factor 0.7 lower than the zero-field value. This decrease of is consistent with the simple model that involves a reduction of effective Josephson coupling energy at $f = 1/2$: the interaction energy of a vortex pair is a factor $\sqrt{2}$ smaller than in zero field. With this lower effective coupling the critical value of E_J/E_C of the S-I transition is reduced by a factor $\sqrt{2}$, which is close to the observed reduction of 0.7.

The experimental data agree rather well with the quantum Monte Carlo calculations [112] in the classical limit. The experimental points of the transition temperatures are, however, lower than the calculated ones by entering in the quantum regime. At present, there is no explanation for this discrepancy. It would require a more detailed study and better understanding of the phase transition at $f = 1/2$. The calculations do indicate, on the other hand, a S-I transition at $E_J/E_C \approx 1$, in agreement with the experiment.

In Fig.11, the critical E_C/E_J ratio as a function of applied magnetic field for square arrays is plotted. The three points at $f = 0,\ 1/2$, and $1/3$ are combined with two data points of the field-tuned S-I transition (see Section II H). After a rapid decrease the critical ratio is almost constant for $f > 0.1$. The critical E_C/E_J ratio at $f = 1/2$ is larger than at other nearby values of f, indicating once again the stability of the phase configuration at $f = 1/2$. Fig.11 also indicates that arrays in the range $1.2 < E_C/E_J < 1.7$ do not show special behavior at commensurate f-values (e.g. dips in the magnetoresistance); arrays are superconducting in zero field but insulating at $f = 1/2,\ 1/3,\ 1/4, ...$

It is possible to derive a Ginzburg-Landau free energy also in the presence of rational frustration [113]. The calculation proceeds along the lines outlined for the $f = 0$ case in Section II B 2. The important difference is that one should expand the free energy about the most fluctuating modes. In the unfrustrated case this means an expansion about $\mathbf{k} = (0, 0)$. For the fully frustrated case ($f = 1/2$) the expansion is carried around the two points: $\mathbf{k} = (0, 0)$ and $\mathbf{k} = (0, \pi)$ thereby reflecting the superlattice structure of the ground state. The resulting free energy depends on a multicomponent (complex) order parameter (e.g. two coupled complex fields in the fully frustrated case).

The magnetic-field dependence of the critical exponent $z\nu$ (ν governs the divergence of the correlation length and z is the dynamical critical exponent) was considered by Niemeyer *et al.* [111]. In zero field the mapping onto a three-dimensional XY model implies that $z\nu = 0.67$. Their analysis hints to a dynamical exponent that increases with the magnetic field. It is, however, difficult draw conclusions on the values of $z\nu$. It could smoothly increase with magnetic field, or immediately jump to one on once the magnetic field has switched on. Combining the fact that $z\nu < 1$ for $f = 1/2$ and that a higher-order expansion predicts $z\nu = 1$ there, the authors conclude that the answer is $z\nu = 1$ for all nonzero magnetic fields. Monte Carlo simulations by Cha and Girvin [114] obtain for the $f = 1/2$ and $f = 1/3$ cases the values $z = 1$ and $1/\nu = 1.5$, consistent with the analysis outlined above.

Finally we mention that, in addition to two-dimensional arrays, frustration effects can be studied in quantum ladders as proposed in Refs. [115].

D. Charge frustration and the supersolid

A uniform charge can be introduced in a quantum JJA by applying a gate voltage $V_{\rm x}$ with respect to the ground plane. This effect is known as *charge frustration*. Although from a theoretical point of view charge and magnetic frustration are dual to each other, experimentally it is only possible to tune the magnetic frustration in a controlled way. In all arrays random offset charges, presumably caused by defects in the junctions or in the substrate [116], are present. Electron or quasi-particle tunneling will partly compensate these offset charges so that their value lies between $-e/2$ and $+e/2$. These charges can, in principle, be nulled out by the use of a gate for each island; this procedure, however, works only for small networks. In large arrays they cannot be compensated because too many gate electrodes would be necessary, requiring too complicated fabrication procedures. A uniform charge frustration has therefore not been realized yet in 2D Josephson arrays. Lafarge *et al.* [117] have investigated charge frustration by placing a gate underneath a Josephson array. They managed to obtain a 40% variation of the resistance between the unfrustrated and the (nominally) fully frustrated array. But most importantly, in studying the current-voltage characteristics, it was impossible to quench the Coulomb blockade as it can be done in circuits with few junctions. In future arrays, charge frustration may be applied more uniformly if the influence of offset charges can be drastically lowered.

1. Phase diagram

The energy difference of two charge states in each island with q and $q+1$ extra Cooper pairs may be reduced by changing $V_{\rm x}$ (which means to change the external charge $q_{\rm x}$). Consequently the effects of a finite charging energy are weakened and the superconducting region in the phase diagram is enlarged. It turns out that for certain values of the gate voltages the energy difference vanishes implying that the Mott gap, and therefore the insulating behavior, is completely frustrated. At the degeneracy point even a small Josephson coupling makes the system superconducting since there is no pay in energy for moving a charge through the whole array. In general it is intuitive to expect that the extension of the insulating lobe will be maximum at integer values of the external charge since in this case the excitation energy is highest.

A quantitative analysis of this phenomenon has only been obtained in models with a short-range electrostatic potential. Uniform charge frustration gives rise to two new effects:

- lobe structures appear in the phase diagrams
- new states in the phase diagram may occur (Wigner-like crystals and the Supersolid).

The remainder of this subsection is devoted to the lobe structures and the Wigner-like charge ordering; the next subsection treats the supersolid.

The lobe-structure already follows from a mean-field analysis with on-site interaction only. The corresponding phase diagram can be obtained by evaluation of the correlator given in Eq.(16) in the presence of an uniform charge. In Fig.12, the mean-field phase boundary in the presence of a uniform background charge is shown. The detailed structure of the lobes is very sensitive to the model used (QPM, BH, XXZ) and on the approximation

made [40,118–123]. The lobes in the Monte Carlo calculation are sharper than predicted by mean-field, but smoother than expected from the strong coupling expansion.

In the case of a finite-range interaction a number of new classical ground states exists characterized by a crystal like ordering of charges. The phase diagram contains extra lobes where the charge density is pinned to a given fractional filling. Their range of existence, in the limit of vanishing Josephson coupling, is found by minimizing the charging part of the Hamiltonian for a given charge filling. We illustrate this by considering the simple case of short range charging energy (only on-site and next-neighbors). In the case of $0 \geq q_x \geq 1/2$ (and for square lattices) only three different charge configuration should be considered.

- All the islands are neutral
- A checkerboard state can be formed in which a sublattice is neutral and the other is charged with one extra Cooper pair
- All the islands can be uniformly charged with charge $2e$.

The corresponding energies of the different ground states are respectively

$$E_{ch,00}/4N = E_0 q_x^2 + \frac{z}{2} E_1 q_x^2 \tag{28}$$

$$E_{ch,01}/4N = \frac{1}{2} E_0 q_x^2 + \frac{1}{2} E_0 (1-q_x)^2 - \frac{z}{2} E_1 q_x (1-q_x) \tag{29}$$

$$E_{ch,11}/4N = E_0 (1-q_x)^2 + \frac{z}{2} E_1 (1-q_x)^2 \tag{30}$$

where N is the number of islands in the array. The ground state energy is given by $E_{ch,00}$ for $0 \geq q_x \geq q_{x,1}$, $E_{ch,01}$ for $q_{x,1} \geq q_x \geq q_{x,2}$ and $E_{ch,00}$ for larger q_x. The critical values at which the ground state changes are

$$q_{x,1} = \frac{1}{2} \frac{1}{1 + (z/2) E_1/E_0}$$
$$q_{x,2} = \frac{1}{2} \frac{1 + z E_1/E_0}{1 + (z/2) E_1/E_0} \; .$$

The S-I boundary (for finite E_J) can be determined, for example, using a mean-field approach. The result is presented in Fig.13. The checkerboard state for $q_{x,1} \geq q_x \geq q_{x,2}$ can be thought of as a Wigner crystal of Cooper pairs. The role of a longer-range charging energy (next nearest neighbors,...) is to stabilize the crystalline phases with lower fillings $(1/4, 1/8, ...)$. Not all the lobes extend down to the $E_J = 0$ axis. First-order phase transitions between different checkerboard states are then possible. Note, that the presence of charge ordering, characterized by a periodicity $2\pi/k_x, 2\pi/k_y$, is detected by studying the structure factor S at a give wave-vector

$$S(k_x, k_y) = \frac{1}{L^4} \Big\langle \sum_{ij} e^{i\mathbf{k}\cdot\mathbf{r}_i} q_i q_0 \Big\rangle \; . \tag{31}$$

A uniform charge frustration changes the symmetry properties of the system. At $k_x = 0$ the energy cost to create (or remove) a Cooper pair in a given island is the same. The system

possesses particle-hole symmetry. For generic values of the external charge this symmetry is broken (i.e., $E_{ch,00} \neq E_{ch,11}$). In the phase diagram shown in Fig.13 the tips of the lobes correspond to a particle-hole symmetric case while away from the tips the symmetry is broken. This change of symmetry is reflected as a new term in the quadratic part of the Ginzburg-Landau free energy. This new contribution is

$$\lambda \sum_i \int d\tau \psi_i^*(\tau) \partial_\tau \psi_i(\tau) \tag{32}$$

where

$$\lambda = i \frac{\partial_{\omega_n} g(\omega_n, q_x) \mid_{\omega_n=0}}{2E_0} \quad . \tag{33}$$

The coefficient λ vanishes in the particle-hole symmetric case (see Appendix C). The particle-hole symmetry has important consequences for the critical behavior of the system [40]. The dynamical critical exponent z changes from $z = 1$ at the tip of the lobes to $z = 2$ in the generic case.

2. Supersolid

A solid phase is characterized by charges being pinned on the islands whereas a superfluid phase is characterized by phase coherence over the whole system (i.e.,charges are delocalized). At the end of 60's [124–126,41] it was suggested that, in addition to the solid and superfluid phases, a new state should appear, characterized by the coexistence of off-diagonal (superfluid) and diagonal (charge-crystalline) long-range order. This phase is known as the *supersolid*. If vacancies in a quantum crystal such as solid ^{4}He Bose-Einstein condense, they do not necessarily destroy the crystal structure and they may form a superfluid solid (or supersolid). Experiments have been performed on ^{4}He, but no positive identification of this coexistence phase has yet been made. There are, however, hints that such a phase exists [127,128].

An exciting possibility that attracted a lot of attention was the idea to observe supersolids in Josephson arrays [42,129–133]. The supersolid phase is located in an intermediate region around the half-filling lobe. A simple way to understand its existence is to focus on a region close to the phase boundary at $q_x \sim 1/2$. At densities corresponding to half filling the particles form an incompressible solid. Away from half-filling vacancies in the charge-solid appear. As they have a bosonic character, they can Bose condense, and therefore they are able to move freely through the system. For a small enough density of vacancies one expects that the crystal order is not destroyed.

In the limit of very large on-site charging (hard-core limit in which the island charge can only be zero or one) the existence of the supersolid is related to the finite next-nearest neighbor interaction as it does not exist for nearest-neighbor interaction only. Furthermore, there is no supersolid phase at exactly half-filling. In Fig.14 the mean-field phase diagram in the hard-core limit is shown. The supersolid region appears in a tiny region away from half filling between the superconducting and Mott insulating phases.

If higher values of charge are allowed, the supersolid phase already exists for nearest-neighbor interaction and also at half-filling on the tip of the checkerboard lobe. This is

related to excitations which are forbidden in the hard-core limit. A large nearest-neighbor interaction or small on-site interaction favors the supersolid, whereas in the hard-core limit the supersolid is suppressed. Thus, it seems that the system itself generates the defects (particle-hole excitations) that Bose condense, thereby turning the solid into the supersolid. The phase diagram for soft-core bosons is shown in Fig.15.

Since the supersolid phase is very sensitive to fluctuations, it was important to obtain independent checks of its existence. Monte Carlo simulations on the QPM [130] and the BH model [132] have confirmed the qualitative picture discussed above. In Fig.15 the symbols represent the phase diagram as obtained from Monte Carlo simulations by van Otterlo and Wagenblast [129,130]. Note that the supersolid region is considerably reduced as compared to the mean-field estimates.

By changing the electrostatic interaction new phases named collinear supersolid were found by Scalettar *et al.* [132] and by Frey and Balents [133]. A detailed analysis of various supersolids including striped phases has recently been performed by Pich and Frey [134]. Supersolid phases in frustrated systems have been studied as well either by combining the effect of charge and magnetic frustration [135] or by considering arrays on Kagomè lattices [136].

Several other kinds of coexistence phases were studied. The possibility of a spontaneous vortex anti-vortex lattice in superfluid films was explored in Refs. [137,138] and a coexistence phase of superfluidity and hexatic orientational order was proposed in Ref. [140]. Orientational order in incompressible quantum Hall fluids is discussed in Ref. [141]. Finally, we mention the relation between 2D bosons and 3D flux-lines in type II superconductors (high-T_c materials) in a magnetic field [143,144]. Also in these systems different kinds of long-range order may coexist and the equivalent of the supersolid is discussed in Refs. [145,146]. Related is the question whether or not vortices may form a disentangled liquid, which would imply a normal ground state for bosons with long-range Coulomb interaction.

E. Dissipation induced S-I transition

The behavior of a single Josephson junction with Ohmic dissipation has been discussed in a pioneering work by A. Schmid [147] who found that there is a zero-temperature phase transition governed by the dissipation strength α. Above the critical value $\alpha = 1$, dissipation suppresses quantum fluctuations thereby restoring the classical behavior with a finite critical current. For weak damping, on the other hand, quantum fluctuations destroy global phase coherence. The supercurrent is suppressed to zero and the junction is in the insulating state.

Experimentally, this transition has only very recently been detected by Penttila *et al.* [148]. The reason is that for a single junction the high-frequency coupling to the environment determines the effective damping. Consequently, the effective impedance is of the order of 100 Ω [], which is about two order of magnitude smaller than the quantum resistance. Penttila *et al.* increased this impedance, i.e., the decoupled their single junction from its environment by placing high-Ohmic, Chromium resistors in the leads close by.

Dissipation plays an important role in quantum phase transitions of JJAs as well. Originally the interest was stimulated by the idea that dissipation could be responsible for the observed critical resistance at the S-I transition in arrays and granular films. Later Fisher [150] and Wen and Zee [151] pointed out that the observed critical resistance is a zero temperature property associated with the existence of a quantum phase transition and

it is not related to the presence of an "extrinsic" source of dissipation. The next section discusses the critical behavior on transport properties in more details. Here, we discuss the influence of dissipation on the phase diagram.

The coupling to a dissipative bath has the effect to suppress the quantum fluctuations of the phase, i.e. to quench the insulating region. The properties of the environment and the type of dissipation are important ingredients in Eq.(10) and in Eq.(11). As stated before, various sources of dissipation should be considered for JJAs. Quasi-particles may still play a role at mK as they may be generated by the environment or the motion of vortices themselves. From a theoretical point of view and in view of the recent experimental advances, it is also possible to realize arrays in which Ohmic shunts are important. These shunts can be normal wires placed parallel to the junctions in a a similar way as was done for a single junction. Ohmic shunts may also arise because of coupling to the substrate (local damping). Very recently the group of Kobayashi succeeded in fabricating a JJA in which each junction is shunted by a Cr resistor [152]. A different and controlled environment was investigated in the experiments of Rimberg *et al.* [153] by placing a 2D electron gas underneath the Josephson array. We briefly discuss all these sources of dissipation.

1. Quasi-particle dissipation

When the mechanism responsible for dissipation is quasi-particle Tunneling, the effective action is that given in Eq.(10). Theoretically this model was studied by means of mean-field calculation [154,155], variational approaches [156–159], and Monte Carlo simulations [160]. The dominant effect coming from quasi-particle tunneling enters in the renormalization of the effective junction capacitance given in Eq.(9). In the mean-field calculation, this amounts to a modification of the capacitance matrix in the evaluation of the phase correlator. The zero-temperature phase boundary (for short range Coulomb interaction) obtained by Chakravarty *et al.* [154], is given by the expression

$$1 = \frac{3\pi}{4}\alpha^2 \frac{1}{\ln\left(1+\frac{3\pi}{4}\frac{E_0}{E_J}\alpha^2\right)} \quad .$$

It is important to stress that in the case of quasi-particle tunneling the array is either insulating or superconducting. The interplay between the long-range Coulomb interaction and quasi-particle dissipation has been discussed in Ref. [91].

In Section II B, we have interpreted the S-I transition as being driven solely by Coulomb interactions. However, given the uncertainty in the damping resistance (e.g. sub-gap resistance of normal-state resistance) of the junctions the possibility that the transition is driven by quasi-particle dissipation cannot be ruled out. The data do not exclude the possibility that the S-I transition is influenced by the normal-state resistance. In fact, the Chalmers group [161] and the group of S. Kobayashi and collaborators [60] have interpreted their data in terms of a Schmid-like diagram. In Fig.16 we show the results from the Chalmers group. The normal state resistance R_N is used as the resistance determining the dissipation parameter. If this resistance is used, a reasonable agreement with the theoretical models is obtained.

2. Ohmic dissipation

The influence of Ohmic shunts on the phase diagram has been intensively investigated as well. A new phase with local phase coherence is possible, i.e., phase coherence only exists as a function of time. Various theoretical methods have been applied in this case such as coarse graining [162–164], variational [163,165–168] and renormalization group [163,166,169] approaches. The general trend is, as expected, that the critical value of E_J/E_0 for the onset of phase coherence is lowered. The dependence on the dissipation strength is stronger as compared with the case of quasi-particle damping. As for a single junction, a true dissipative transition occurs. A rigorous analysis can be performed in various limits in the $E_J - \alpha$ phase diagram [163,166]. For simplicity we discuss only the $T = 0$ case and follow the discussion presented in Ref. [170].

- In the large α limit time-like fluctuations of the phase are strongly suppressed and they only contribute to the renormalization of the effective Josephson coupling. The system behaves like a classical JJA with an effective Josephson coupling

$$E_J^{eff} = E_J \left(1 - \frac{1}{\alpha \mathrm{z}} \ln\left(1 + \frac{\alpha}{2\pi}\right)\right) \quad .$$

  At zero temperature the array is in the superconducting phase independent on the ratio E_J/E_0.

- In the case $E_J/E_0 \gg 1$ there is a phase transition at

$$\alpha = \frac{1}{\mathrm{z}}$$

  which separates two phases that both exhibit long-range coherence. Evidence of such a phase transition could be detected by measuring the voltage noise power spectrum.

- In the limit of small damping, the critical ratio of E_J/E_0 is renormalized to smaller values indicating that dissipation enhances the superfluid phase.

- If the ratio E_J/E_0 is very small, a dissipative transition to a phase with local order can take place at a critical value of dissipation given by

$$\alpha = \frac{2}{\mathrm{z}} \quad .$$

Very recently Takahide *et al.* [152] fabricated a JJA in which each junction was shunted by a Cr resistor. By varying the resistance of the shunts and the ratio E_J/E_0 they were able to map out the phase diagram. The results are in good agreement with the theories of dissipation induced quantum phase transition discussed above.

3. Local damping

Dissipation may also arise from coupling with the substrate by means of what is named as the 'local damping' model. Local damping changes the universality class of the S-I transition [174], and influences the low-frequency dispersion of the vortex response in classical

arrays [172,173]. As shown in Eq.(12)), the local damping model correlates the island phase in time. In proximity-coupled arrays, which consist of superconducting islands on top of a metallic film, the model with local-damping is appropriate to describe the flow of normal electrons into the substrate. Aluminum tunnel junction arrays are always placed on insulating substrates so that it is not appropriate.

Dissipation due to local damping is associated with the phase ϕ_i, rather with the phase difference $\phi_i - \phi_j$ as in the resistively shunted junctions (RSJ) model. The number of Cooper pairs in each island is allowed to decay, whereas the RSJ model describes only charge transfer between neighboring islands. By going through the same steps outlined in the section on the coarse-graining method, it is possible to obtain also in this case an effective Ginzburg-Landau free energy. The only difference is that now the phase-phase correlator $g(\tau)$ has to be evaluated including the local damping term. For small frequencies the Fourier transform reads (for more details see Ref. [174])

$$g(\omega_\mu) = g(0) - \eta \left|\omega_\mu\right|^s - \zeta\omega_\mu^2 \qquad \text{with } s = \frac{2}{\alpha} - 1 \; . \tag{34}$$

The coefficients η and ζ can be determined from the phase correlator (their value is not important for our purposes). Using this expression for $g(\omega_\mu)$, the free energy in Eq.(20) contains a *non-Ohmic* dissipative term ($\propto |\omega_\mu|^s$) (reducing to Ohmic, or 'velocity proportional' damping only in the special case $s = 1$). This means that *Ohmic* damping in the quantum phase model yields *non-Ohmic* dynamics for the coarse-grained order-parameter. The phase boundary in the saddle point approximation is shown in the inset of Fig.17. By increasing damping strength, the superconducting region is enlarged. At $T = 0$ a quantum phase transition is ruled out beyond the critical value $\alpha = 2$.

4. Tunable dissipative environment

A controlled study of the dissipative S-I transition has been performed by Rimberg *et al.* [153]. They placed a Josephson array on top of a two-dimensional electron gas (2DEG). Junction parameters are chosen such that in the absence of the 2DEG the array is insulating. The array is capacitively coupled to the electron gas and its screening currents provide a source for dissipation. By tuning the back-gate voltage, the electron density and the sheet resistance R_g of the 2DEG are varied without changing the array parameters. As the resistance of the 2DEG increases the current-voltage characteristics of the array change from superconducting to insulating with a Coulomb gap as illustrated in Fig.18. Moreover the resistance of the array is very sensitive on R_g as shown in Fig.19. Note that in the experiment the island capacitance (to the 2DEG) exceeds the estimated junction capacitance of 0.5 fF by a factor of 6.

Wagenblast *et al.* [171] analyzed these measurement and modeled the experimental setup by capacitively coupling the array to the 2DEG. Assuming Ohmic dynamics of the 2DEG they obtained the following (Caldeira-Leggett like) effective action for the array

$$S_{\text{eff}}[\varphi] = \frac{1}{2}\sum_{\omega_\mu} \int d\mathbf{k} D_0^{-1}(k,\omega_\mu) |\varphi_{k,\omega_\mu}|^2 + S_J \tag{35}$$

(S_J is the action related to the Josephson coupling) with the propagator

$$D_0^{-1}(k,\omega_\mu) = \frac{C}{4e^2}k^2\omega_\mu^2 + \frac{C_0}{4e^2}\frac{k^2\omega_\mu^2}{k^2+|\omega_\mu|/\Omega_0} \quad , \tag{36}$$

where C_0 now represents the capacitive coupling to the 2DEG and where $1/\Omega_0 = R_g C_0$. The effective action for the array is Ohmic only in an *intermediate* frequency range. At the lowest and highest frequencies the dynamics is capacitive. The two energy scales are well separated in the case $C_0 \gg C$ and a quantum phase transition is driven by the action at the lowest frequencies. As the dissipative action is cut off at the lowest frequencies, a dissipation driven transition cannot occur in the strict sense. However, quasi-critical behavior can be observed at temperatures and voltages exceeding the low energy scale Ω_0. In the limit $\Omega_0 \to 0$ ($C_0 \to \infty$) this behavior converges to a true dissipation-tuned transition.

An analysis of the conductivity as a function of E_J and α suggests a phase diagram of the type represented in Fig.20. The insets show $R_0(T)$ as a function of the temperature in different regions. The experiments of Rimberg *et al.* belong to the right-lower sector of the Schmid diagram. The theoretical temperature dependence of the resistivity $R_0(T)$ as well as the exponential relation between R_0 and R_g are in good agreement with the experiments [153].

F. Transport Properties

The unique feature of quantum critical points is that quantum fluctuations, which drive the system through the transition, govern its dynamical behavior. The interest in understanding charge transport near a quantum phase transition goes beyond the study of JJAs. Important examples are the transition in quantized Hall systems [12], localization in Si-MOSFETs [175] and the quantum critical point in cuprates [176].

In two dimensions right at the S-I transition the zero-temperature conductance [177] has been predicted to be finite and universal. This metallic behavior is present even in the absence of extrinsic dissipation and it is entirely due to the presence of collective modes which become soft at the zero-temperature transition point. Universality at a quantum phase transition then implies that the properties of the system are governed by a set of critical exponents. X.G. Wen [178] employed a scaling theory of conserved currents at anisotropic critical points identifying universal amplitudes. One of these amplitudes in two dimensions reduces to the universal conductance.

A very simple argument [179] leading to a finite *and* universal conductance at zero temperature can be discussed using the duality between charges and vortices formulated in Section II B. Strictly speaking it applies to the case $C_0 = 0$, i.e. for logarithmic interacting charges. From the Josephson relation the voltage drop across an array is given by the rate of vortices crossing the sample boundary. The current is given by the number of Cooper pairs which flow through the system per unit time, i.e.,

$$V = \frac{h}{2e}\langle \dot{v} \rangle \qquad\qquad I = 2e\langle \dot{q} \rangle$$

At the self-dual point $\langle \dot{v} \rangle = \langle \dot{q} \rangle$ and therefore the conductance at the transition (denoted with σ^*) is finite, universal and corresponds to the quantum of resistance for Cooper pairs:

$$\sigma^* = \frac{4e^2}{h}$$

The value of σ^* changes in the case of short-range charging and/or in the presence of disorder. Nevertheless it remains universal (independent on the sample parameters).

A large amount of theoretical work has been devoted to the determination of the critical value σ^* and the scaling behavior of the conductance. The universal conductance in a model with no disorder was considered in Ref. [180] by means of a $1/N$ expansion and Monte Carlo simulations and in Ref. [181] by means of an ϵ-expansion. The dirty boson system and the transition to the Bose glass phase (including the case of long-range Coulomb interaction) was extensively studied by Monte Carlo simulations [182–185] and Lanczos diagonalization [186] as well as by using analytic calculations [187]. The finite-frequency properties close to the transition point were analyzed in Refs. [188–190]. More recently, in a series of papers, Sachdev and coworkers [191–193] studied non-zero temperature transport properties by means of a Boltzmann equation.

A general analysis of the conductivity close to the transition can be performed based on scaling arguments. The frequency dependence of the conductivity $\sigma(\omega)$ has been obtained from its relation with the frequency dependent stiffness $\rho_s(\omega)$ (related to the increase of the free energy due to a time dependent twist) $\sigma(\omega) = 4e^2\rho_s(-i\omega)/i\omega$. Close to the transition it can be shown that the conductance obeys the scaling form [150,180,194]

$$\sigma(\delta, T, \omega) = \frac{h}{4e^2} f(\frac{\omega}{T}\ ,\ \frac{\delta}{T^{z\nu}}) \tag{37}$$

where δ measures the distance from the critical point, and where $f(x, y)$ is a dimensionless scaling function. In the limit of very low temperature (compared to the frequency), the temperature drops out of the previous expression and the two scaling variables enter in the form

$$\sigma(\delta, T = 0, \omega) = \frac{h}{4e^2} \tilde{f}(\frac{\delta}{\omega^{z\nu}}). \tag{38}$$

In view of the scaling behavior of the conductance, one should consider two limits $\omega \ll T$ and $\omega \gg T$. This point, emphasized in Refs. [191–193], is important both from a conceptual point of view and for a detailed comparison with experiments. The two situations correspond to two different experimental setups for transport measurements. In the $\omega \ll T$ case, charge transport is governed by inelastic scattering between thermally excited carriers. In the opposite $\omega \gg T$ situation, collision between carriers can be neglected. In Eq.(37) the two limiting cases correspond to $f(0, 0)$ and $f(\infty, 0)$ respectively. It turns out that both values are universal but different.

Here, we discuss the most prominent features of the conductivity close to the S-I transition by means of the Ginzburg-Landau free energy of Eq.(20). Connections to other models will be given. In the linear response regime the conductivity follows from the functional derivatives of the partition function. In the presence of an electromagnetic potential $\mathbf{A}$, the gradient term in the Ginzburg-Landau free energy enter in a gauge-invariant form:

$$\nabla \ \longrightarrow \ \nabla - \frac{2\pi}{\Phi_0}\mathbf{A}$$

By noticing that the current is the derivative of the free energy with respect to the vector potential and that the electric field is the time derivative of the vector potential (with a negative sign), the conductivity, in imaginary time, is expressed as ($a(b) = x, y$)

$$\sigma_{ab}(\omega_\mu) = \frac{1}{\omega_\mu} \int d^2r\, d\tau \frac{\delta^2 \ln Z}{\delta A_a(\mathbf{r},\tau)\delta A_b(0)} \mid_{\mathbf{A}=0} e^{i\omega_\mu \tau} \ . \tag{39}$$

Using Eq.(20), the longitudinal conductivity $\sigma_{aa} = \sigma$ can be expressed in terms of two- and four-point Green's functions. In the absence of charge and magnetic frustration and by evaluating the correlators in the Gaussian approximation, one obtains [180]

$$\sigma(\omega_\mu) = \frac{2}{R_Q \omega_\mu} \frac{1}{\beta} \sum_\nu \int dk\, k^3\, G(k,\omega_\nu)\left[G(k,\omega_\nu) - G(k,\omega_\nu+\omega_\mu)\right] \ , \tag{40}$$

where

$$G(k,\omega_\mu) = \frac{1}{\epsilon + k^2 + \zeta\omega_\mu^2} \quad .$$

This turns out to be the first term in a $1/N$ expansion [180]. The sum over the Matsubara frequencies can be performed by contour integration. The result is

$$\sigma(\omega) = \frac{1}{4\pi R_Q \omega} \int_{-\infty}^{\infty} \frac{dz}{1-e^{-\beta z}} \int_0^\infty dk k^3 \Im G^R(k,z)\Big[\Re G^R(k,z) - \Re G^R(k,z+\omega)\Big], \tag{41}$$

where the retarded G^R and advanced G^A Green's functions are given by

$$G^{R/A}(k,\omega) = G(k,\omega_\nu \longrightarrow \omega \pm i\eta) \ .$$

The previous expression can be evaluated in various important limits.

1. Zero-temperature conductivity

Performing the k-integral the real and imaginary parts of the conductivity are

$$\Re\, \sigma(\omega) = \frac{\pi}{8R_Q}\left(1 - \frac{\omega_c^2}{\omega^2}\right)\Theta(\omega^2 - \omega_c^2) \tag{42}$$

$$\Im\, \sigma(\omega) = \frac{1}{8R_Q}\left[-\frac{2\omega_c}{\omega} + \left(1 - \frac{\omega_c^2}{\omega^2}\right)\ln\left|\frac{\omega-\omega_c}{\omega+\omega_c}\right|\right] \tag{43}$$

where

$$\omega_c = 2\sqrt{\frac{\epsilon}{\zeta}} \quad .$$

At low frequencies the real part of the conductivity exhibits an excitation gap equal to ω_c. In the insulating region the system, as can be deduced from the behavior of the imaginary part of the conductivity, behaves as an effective capacitor with

$$C_{eff} = \frac{1}{6R_Q\omega_c} \ .$$

The previous expressions can be calculated in the lowest order in $1/N$ and obey the scaling law with $z\nu = 1$. The threshold frequency vanishes at the S-I transition leading to a finite d.c. ($\omega \to 0$) conductivity,

$$\sigma^\star = \frac{\pi}{8}\frac{4e^2}{h} \ . \tag{44}$$

As explained in the first part of this section, this corresponds to the evaluation of the scaling function for $\omega/T \to \infty$ (the collision-free regime). Corrections to the next order in the $1/N$ expansion correct this Gaussian result by roughly 30%.

Another powerful method for evaluating critical quantities is the ϵ-expansion. In order to set up the ϵ-expansion one should move away from two dimensions and consider systems with $d-1$ spatial dimensions. This approach allows one to obtain the scaling form of the frequency dependent conductance [181] in d dimensions.

In the fully frustrated case ($f = 1/2$) the conductance at the S-I transition is still finite but with a value which is different from the $f = 0$ case. It is possible to evaluate it in a $1/N$-expansion [195] and to the lowest order the conductance is twice the value of the critical conductance in zero field.

$$\sigma^\star(f = 1/2) = 2\sigma^\star(f = 0)$$

This factor of two is reminiscent of the superlattice structure at full frustration. There are, however, no fundamental reasons why this ratio should hold in general.

2. Finite-temperature conductivity

At low temperatures ($T \ll \omega_c$), the real part of the conductivity is given by [188,191]

$$\Re\,\sigma(\omega) = \frac{2\pi}{R_Q} T e^{-\beta\omega_c}\delta(\omega) + \frac{\pi}{8R_Q}\left(1 - \frac{\omega_c^2}{\omega^2}\right)\Theta(\omega^2 - \omega_c^2)\left[1 + 2e^{-\beta|\omega|/2}\right] \tag{45}$$

The imaginary part is obtained by means of Kramers-Kronig dispersion relations

$$\Im\,\sigma(\omega) = \frac{2}{R_Q\omega} T e^{-\beta\omega_c} + \omega C_{eff} \tag{46}$$

where

$$C_{eff} = \frac{1}{6\omega_c R_Q}\left(1 + 24\frac{T^2}{\omega_c^2}e^{-\beta\omega_c}\right) \tag{47}$$

The Drude peak in the real part of the conductivity arises due to a lack of dissipation or disorder in this model. Once electron or hole like excitations are created, they will propagate without damping thus leading to perfect conductivity. Although the system is a perfect conductor it is not a superconductor since it shows no Meissner effect. The response of the system to a static **k**-dependent magnetic field, is proportional to k^2, i.e. it vanishes at long wavelengths.

The scale for the crossover to the classical behavior is set by $T \sim \omega_c$ In the high temperature limit ($T \gg \omega_c$), the real and imaginary part of the conductivity read

$$\Re\,\sigma(\omega) = \pi\frac{\rho_D}{R_Q}\delta(\omega) + \frac{\pi T}{2R_Q \mid \omega \mid}\left(1 - \frac{\omega_c^2}{\omega^2}\right)\Theta(\omega_c^2 - \omega^2) \tag{48}$$

$$\Im\,\sigma(\omega) = \frac{\rho_D}{R_Q\omega} + \frac{T}{4R_Q\omega_c^2}\omega \tag{49}$$

where $\rho_D \sim T$ and the expression for the imaginary part is valid at frequencies much smaller than ω_c.

Damle and Sachdev [191,192] pointed out that since the conductance is a universal function of ω/T, it makes a difference which limit is taken first (either $\omega \to 0$ or $T \to 0$). In order to study the collision-dominated regime they used a Boltzmann like approach in which the current is expressed in terms of distribution functions for the particle and hole-like excitations. By solving the appropriate Boltzmann equation (the collision term can be obtained by Fermi golden rule) they showed that also in the collision dominated regime the conductivity is a universal function at the critical point. We refer to the book by Sachdev for a clear and comprehensive presentation of these aspects of transport close to quantum critical points [13].

3. Non universal behavior

Despite the conceptual elegance of the theories predicting a universal conductance at the transition, the experiments on JJAs and two-dimensional superconducting films show critical resistivities that are different (by a factor up to ten) as compared to the predicted universal values. Wagenblast *et al.* [174] developed a theory of this non-universal behavior using the local-damping model. The evaluation of the dynamical conductivity proceeds along the same lines discussed before (see Eq. 34). The advanced and retarded Greens functions are given by

$$\Big[G^{A/R}(k,\omega)\Big]^{-1} = \epsilon + k^2 - \zeta\omega^2 + \eta|\omega|^s\Big[\cos\frac{s\pi}{2} \pm i\mathrm{sign}(\omega)\sin\frac{s\pi}{2}\Big], \tag{50}$$

With increasing damping the Mott gap is smeared out. For $s < 2$ and low frequencies $\omega \ll \omega_c$ one finds

$$\mathrm{Re}\,\sigma(\omega) = \frac{1}{R_Q}\frac{\eta^2\sin^2(\frac{\pi}{2}s)}{6\pi\epsilon^2}\frac{[\Gamma(1+s)]^2}{\Gamma(2+2s)}|\omega|^{2s}\,. \tag{51}$$

The conductivity shows a power-law behavior at low frequency, where the power depends on the dissipation strength for $s \leq 2$. Of particular interest is the d.c. conductivity at the transition, which becomes a function of the strength of Ohmic damping for $\alpha > 2/3$.

This model with local damping was further explored by Dalidovich and Phillips [196] in the case $s = 1$. In the limit of weak damping they find that dissipation leads to a leveling off of the d.c. conductivity at intermediate temperatures. Their estimates indicate resistance plateaus of the order of 10 kΩ in the mK range, compatible with the experiments. These results seem more applicable to uniform films rather than to JJAs. In any case they offer an interesting explanation for the experimental observation that the critical resistance is not universal.

G. One-dimensional arrays

Josephson-junction chains have been much less investigated (both theoretically and experimentally) as compared to two-dimensional systems and only recently the S-I transition

in one-dimensional samples has been measured [197]. In addition to the possibility to fabricate arrays with controlled couplings, in Josephson chains the ratio of the Josephson to the charging energy can be varied *in situ* by connecting mesoscopic SQUIDS in series (as illustrated in Fig.21). In this setup, the sample behaves as a chain of junctions with a tunable Josephson coupling $E_J(\Phi) = 2E_J \cos(\pi\Phi/\Phi_0)$ depending on the magnetic flux Φ piercing the SQUID. By varying Φ, it is possible to sweep through the S-I transition while measuring on the same sample.

At zero temperature and for short range Coulomb interaction the S-I transition of a d-dimensional array is of the same universality class as a classical XY model in $d+1$ dimensions. Therefore Josephson chains should exhibit a BKT-like transition. By means of duality transformation it is possible to map the XY-model onto a gas of logarithmic interacting vortices [198]. Vortices are bound in pairs (of opposite vorticity) below the transition temperature and are in a plasma phase in the disordered (high temperature phase). In a quantum chain the relevant topological excitations, which correspond to vortices in space-time, are (quantum) phase slips. The mapping of a Josephson chain onto a gas of interacting phase slips has been performed by Bradley and Doniach [199].

Consider, for simplicity, only the charging part of the Hamiltonian and neglect the contribution due to the junction capacitance.

$$Z_{ch} = \prod_{i,} \int D\phi_i(\tau) Dq_i(\tau) \exp\left[- \int_0^\beta d\tau 4E_0 \sum_i q_i^2 + i \sum_i \int_0^\beta d\tau q_i \dot{\phi}_i \right] \quad . \tag{52}$$

The summation over the winding numbers fixes the charges to be integers in units of $2e$. By discretizing the path integral (with a time slice τ_ϵ and performing the summation over the integers q_i the charging contribution to the partition function can be recasted into the form

$$Z_{ch} = \prod_{i,\tau} \int d\phi_{i,\tau} \sum_{[n]} \exp[-(1/8\tau_\epsilon E_0) \sum_{i,\tau} (\phi_{i,\tau} - \phi_{i,\tau+\tau_\epsilon} - 2\pi n_{i,\tau})^2] \; . \tag{53}$$

Eq.(53) is the Villain approximation of the XY potential [86] if one identifies $\phi_{i,\tau} - \phi_{i,\tau+\epsilon}$ as the dynamical variable and $1/\epsilon E_0$ as the effective coupling. The time slice ϵ can then be chosen such that the coupling in space and time is isotropic ($\epsilon \sim 1/\sqrt{8E_J E_0}$) [200]. The XY model in space-time has a reduced coupling proportional to the ratio $\sqrt{E_J/8E_0}$. Therefore, all the known results for the classical XY model directly apply with the following replacement

$$\frac{E_J}{T} \quad \longrightarrow \quad \sqrt{\frac{E_J}{8E_0}} \tag{54}$$

The identification of the charging energy with the effective temperature shows the analogy between classical (thermal) and quantum (induced by charging effects) fluctuations. The partition function can now be expressed in terms of interacting phase slips (in the same fashion as in the classical where it is expressed in terms of vortices):

$$\mathcal{Z} = \sum_p \exp\left[- \frac{2\pi^2}{N_x N_\tau} \sqrt{\frac{E_J}{E_0}} \sum_{k,\omega} p(k,\omega) G_0(k,\omega) p(-k,-\omega) \right] , \tag{55}$$

where $p \pm 1$ are the "charges" associated with the occurrence of a phase slip.

The function

$$G_0(k,\omega) \sim (k^2+\omega^2)^{-1}$$

implies that phase slips interact logarithmically in space-time. The chain undergoes a BKT phase transition at a critical value

$$\sqrt{E_J/E_0} \sim 2/\pi \quad .$$

When a Josephson coupling is larger than the critical value the phase correlator decays algebraically (quasi-long range order) and the chain is superconducting. Phase slips are bound in pairs of opposite sign and therefore they do not lead to any dissipation over a macroscopic region (the Josephson relation implies that the occurrence of phase slip leads to a voltage drop). In the opposite regime the chain is in the insulating phase. Phase slips are not paired and any current leads to a voltage. The correlation length is then given by

$$\xi \sim \exp\left\{-\frac{b}{\sqrt{1-[\pi^2 E_J/16E_0]^{1/2}}}\right\}$$

($b \sim 1$). Due to the isotropy in the space-time direction, one can now define an effective Coulomb gap $\sim E_0\xi^{-1}$. As long as there is particle-hole symmetry a finite range Coulomb interaction does not change the universality class of the transition. A detailed analysis of the phase diagram, for realistic Coulomb interactions, as a function of the charge frustration has been performed by Odintsov [201].

The presence of dissipation (see also Section II E) modifies the critical behavior of the chain. The case of a Josephson chain with Ohmic dissipation has been considered by several authors [202–205] by means of dual transformations and Monte Carlo simulations. The main conclusions of this series of works is the zero-temperature-phase diagram as a function of dissipation strength and Josephson coupling as shown in Fig.22. In addition to the S-I phase boundary there are two new phases induced entirely by dissipation:

- for small Josephson coupling and large dissipation the chain is in a phase with local order. The phase difference at each junction is locked in time but the chain has no quasi long-range order
- for large dissipation and large Josephson coupling there is a new type of superconducting phase characterized by the phase slips bound in quadrupoles.

The four different phases can be measured by considering different setups as discussed in Ref. [205].

We conclude this section by reviewing the experiments of Chow *et al.* [197]. The dependence of the resistance on the temperature, shown in Fig.23, shows a non trivial scaling behavior. The two set of curves (solid and dashed) refer to two chains of different length. While in the insulating phase the resistance increases with the number of junctions, in the superconducting phase the opposite trend is visible. By identifying the scale-independent value of $R_0(T)$, Chow *et al.* were able to trace out the zero-temperature critical point (indicated with J^* in the figure).

The resistance in the superconducting chains can be explained in terms of formation of phase slips. The flat tails in the curves are due to a finite-size effect and occur for temperatures of the order of the effective Coulomb gap. In this region the probability of a phase slip event obtained in the Coulomb gas picture presented above scales with the number of junctions as $N_x^{2-\pi\sqrt{E_J/8E_0}}$. Quantum phase fluctuations are suppressed by increasing the system size. In the insulating regime the $I-V$ curves show Coulomb blockade with a threshold voltage which depends on the magnetic flux piercing the SQUID [206] as shown in Fig.24. Thus, there is reasonable agreement with the theory, but finite-size effects make a quantitative analysis difficult because of the rapidly diverging correlation lengths.

1. 1D arrays as Luttinger Liquids

The interest in one-dimensional arrays goes further as they can be described in terms of the Luttinger liquid (LL) model [207]. The low-energy excitations of the interacting electron gas in one dimension are long-wavelength spin and charge oscillations, rather than fermionic quasi-particle excitations. Accordingly, the transport properties cannot be described in terms of the conventional Fermi-liquid approach. The density of states shows asymptotic power-law behavior at low energies. Depending on the sign of the interaction an arbitrarily weak barrier in a quantum wire leads to perfectly reflecting (for repulsive interactions) or transmitting behavior at low voltages [208]. It is customary to characterize this interaction by a parameter g such that $g=1$ in the noninteracting situation while $g>(<)1$ in the attractive (repulsive) case.

A Josephson chain seems an ideal system to explore LL correlations [209]. In the limit of large Josephson coupling $g=\sqrt{E_J/8E_0}\gg 1$; i.e., the chain behaves as an attractive LL. Glazman and Larkin [210] showed that in a certain region of parameters (close to $q_x=1/2$) between the Mott lobe and the superconducting region, there is a new intermediate phase which is equivalent to the chain behaving as a *repulsive* LL. In order to characterize this repulsive behavior one should consider a Josephson chain with a defect. One of the junctions could for example be made with a Josephson coupling much smaller than the charging energy [210,209]. The different phases in the phase diagram can be characterized by the dependence of the Josephson current on the chain length. In the superconducting phase, the defect has no effect as the number of junctions increases. On the contrary, in the repulsive LL phase there is a strong dependence on the number of junctions. The LL phase can be studied also by means of Andreev tunneling spectroscopy along the lines discussed in Ref. [211].

Repulsive LL behavior is also present in a Josephson ladder as discussed in Ref. [212]. The possibility of repulsive LL behavior is related to a normal phase of interacting bosons at zero temperature. In one-dimensional systems such a possibility cannot be excluded and Monte Carlo simulations on a Josephson chain [213] show a phase in which there is neither crystalline nor superfluid order. The existence of a normal phase has been questioned in Ref. [214] through Density Matrix Renormalization Group of the BH model. One should note however that phase boundaries are non-universal and therefore the QPM and BH system can lead to different results.

H. Field-tuned transitions

In arrays which are in the superconducting state at $f = 0$ but have an E_J/E_C ratio close to the critical value, a magnetic field can be used to drive the array into the insulating state. This field-tuned transition has been considered theoretically by M.P.A. Fisher [215] in disordered systems and has first been observed by Hebard and Palaanen [216,217] in thin InO_x films. The interplay between disorder and vortex-vortex interactions plays an essential role. At low magnetic fields vortices at $T = 0$ are pinned (by disorder) but for higher fields, the vortex density increases and at some critical density, vortices Bose-condense (a vortex superfluid leads to an infinite resistance). By employing duality arguments this transition can also be thought as a Bose condensation of vortices that occurs by changing the applied magnetic field.

The general characteristic of the field-tuned S-I transition is that when f is increased from zero, the temperature derivative of the resistance changes sign at critical values $\pm f_c$. Fisher's analysis [215] leads to the following scaling for the resistivity tensor close to the field tuned transition

$$\rho_{\alpha,\beta} = \frac{h}{4e^2}\tilde{\rho}_{\alpha,\beta}(\frac{f - f_c}{T^{1/z\nu}}) \tag{56}$$

where ν is the exponent which controls the divergence of the correlation length at the transition and z is the dynamical critical exponent (with $z\nu \geq 1$). The resistivities are predicted to be universal at the transition and should satisfy the relation

$$\sqrt{\rho_{x,x}^2 + \rho_{x,y}^2} = \frac{h}{4e^2} \tag{57}$$

These predictions were tested in Josephson arrays by the Delft [51,218] and the Chalmers groups [52].

For several values of the frustration, the resistance as a function of temperature is shown in Fig.25. Below a critical value f_c, the resistance decreases upon cooling down ($dR_0/dT > 0$). Above f_c the resistance increases ($dR_0/dT < 0$) and for low temperatures reaches a value that might be orders of magnitudes higher than the normal-state resistance. This sign change in the temperature dependence corresponds to a change in the I-V characteristics shown in Fig.26. For $f < f_c$, a critical current is observed in the I-V characteristics, whereas above f_c a charging gap develops. Note that at low temperatures, the resistance flattens off. This is most likely a finite size effect involving quantum tunneling of vortices. Finite-size effects are expected to play a more prominent role in JJAs as compared to films because arrays are typically 100 cells wide. In units of the coherence length, films are much larger.

A more detailed way of observing the field-tuned S-I transition is obtained by measuring the resistance versus magnetic field for different temperatures (see Fig.27). In the range $0 < f < 1/3$, the $R(f)$ curves are very similar to the ones measured in thin films. Below the critical field f_c=0.14 the resistance becomes smaller when the temperature is lowered and above f_c the resistance increases.

From the scaling analysis [215], it follows that the slopes of the $R(f)$ curves at f_c should follow a power-law dependence on T with power $-1/(z\nu)$. When on a double logarithmic plot the slopes of the $R(f)$ curves at f_c are plotted versus $1/T$, one finds straight lines in

the temperature range $50 < T < 500$ mK. ¿From the reciprocal of the slope, the product $z\nu$ can be determined. Values in JJAs range from 1.2 to 2 for the Delft data and from 1.5 to 8.2 for the Chalmers data, in agreement with the theoretical expectations $z = 1$ and $\nu \geq 1$. The scaling resulting from Eq.(56) is best seen by plotting the resistance as a function $(f - f_c)/T^{1/z\nu}$ as illustrated in Fig.28: A universal function is obtained by plotting the resistance as a function of $E_J(f - f_c)/(E_C T^{1/z\nu})$. The tails on the superconducting side (bottom curve) correspond to the finite-size effect mention above.

The exponent z can also be obtained form the measurements by plotting f_c as a function of the zero-field BKT transition temperature:

$$f_c \propto T_J^{2/z} \quad .$$

The Delft-data points on the triangular arrays yield a rough estimate of $z \approx 0.34$ and their two data points on the square arrays of $z \approx 1.4$. The Chalmers data provide a more accurate fit yielding $z = 1.05$, in good agreement with the theoretical expectation.

Measurements on different thin films show that the resistance right at the transition is of the order of R_Q but measurements are not conclusive regarding the universality. In arrays, this resistance is again of order R_Q, yet in different arrays it varies between 1.6 and 12.5 kΩ. The Chalmers group has also measured the Hall resistance in order to check the validity of Eq.57. For two arrays, the Hall resistance at the critical point is of the order of 30 Ω, but again $\sqrt{\rho_{x,x}^2 + \rho_{x,y}^2}$ is not a universal quantity.

A new feature introduced by JJAs is the existence of field-tuned transitions near commensurate values of the applied field, i.e., at $f_{comm} \pm f_c$ [53,218]. Studying the $R(f)$ curves of JJAs in more detail, critical behavior is not only seen around $f = 0$, but also around $f = \pm 1/4,\ \pm 1/3,\ \pm 1/2,\ \pm 2/3$, and $\pm 3/4$. For each commensurate f-value $z\nu$ can be determined as described above and the values of $z\nu$ are close to one. The sample-dependent critical resistances are of the order of a few kΩ. Calculations on the Bose-Hubbard model in a magnetic field [114] show that the product $z\nu$ at $f = 1/2$ is close to 1 in agreement with the measurement.

III. QUANTUM VORTEX DYNAMICS

A vortex (antivortex) is a topological excitation. When going around its center in a closed loop, the phases of the islands wind up to 2π (-2π). Vortices have extensively been studied in classical arrays where they both determine both the phase diagram and the dynamical properties. To a large extent, this still holds for quantum arrays where the interplay between vortex and charge dynamics plays the central role. The field tuned transition for instance can be understood as a Bose condensation of vortices or charges and the S-I transition in zero field can be analyzed using the duality between charge and vortex excitations. In this section we show that vortices characterize the quantum dynamics of arrays as well. We concentrate on the superconducting side of the S-I transition where vortices are well defined excitations.

As discussed before, quantum arrays have flux penetration depths that are larger than the array sizes. The magnetic field is almost uniform over the whole array area indicating

that there is not one flux quantum in particular cell. [2]

The essential aspect of vortices in junction arrays is therefore not the flux, but the distribution of phases. The phase configuration of a vortex (shown in Fig.29) in a large 2D array can be approximated by the following analytical expression

$$\phi_i = \pm \arctan\left(\frac{y_i - y}{x_i - x}\right) \tag{58}$$

where the site i has coordinates $\mathbf{r}_i = [x_i, y_i]$ and the vortex center is placed at ($\mathbf{r} = [x, y]$). The $\pm$ sign refers to the vortex (antivortex) configuration. For most purposes Eq.(58) is accurate even very close to the vortex center. As we will see, the approximate arc-tan solution is very useful since it allows to express the action in terms of the coordinates of the vortex center $\mathbf{r}$ only (instead of in term of all the phases). This appears to be a reliable description as long as the vortex can be considered as a rigid body. In most of the cases we discuss in this review, this turns out to be a good approximation.

An important property of vortices is that supercurrents around them fall off inversely proportional to the distance r from their core. Vortex-vortex interactions therefore have a long-distance character as they are proportional to $\ln r$. Eq.(58) is the solution for a single vortex in an infinite system. In finite systems, vortices interact with boundaries. The interaction of vortices with the open edges can be viewed as the attraction of a vortex with an image antivortex outside the array. Superconducting banks repel vortices; the interaction with these edges can be viewed as the one with an image vortex (of the same sign) outside the array. The interaction between boundaries indicates that especially in small arrays the approximation given in Eq.(58) is no longer valid. Numerical calculations are then used to extract the quasi-static phase configuration around a vortex.

Experimentally, single-vortex dynamics is studied by applying a small magnetic field (low vortex densities) and performing transport measurements. On the theoretical side, both numerical simulations and phenomenological models which lump the collective dynamics of the phases into the description of the motion of the vortex center, have been investigated. In this chapter, we first derive the classical equation of motion and show that vortices in underdamped arrays can be viewed as massive, point-like particles. We then continue with the quantum corrections to the equation of motion and discuss their consequences. First, there is a renormalization of the vortex parameters (like the mass, damping, ...) due to quantum fluctuations. In addition there is a class of new phenomena which arise from the quantum dynamics of vortices which are treated in Sec. III D and III E. They include macroscopic quantum tunneling of vortices in 2D arrays, quantum interference in a hexagon-shaped array, Bloch oscillations of vortices in the periodic lattice potential and

[2]Self-field effects may play a role in classical arrays since critical currents are substantially larger. Generally, speaking self-field effects manifest themselves in two ways [219]. First, there are self-inductance effects which are short-ranged and caused by the self-inductance of the cell loop. It turns out that the cell-to-cell energy barrier is dominated by these short-range interactions. Second, there are mutual-inductive effects which have a longer range. For example, the current distribution around a vortex changes from an exponential fall-off for self-inductances to an algebraic fall-off when the mutual inductances between all cell pairs are included.

vortex localization in quasi one-dimensional arrays. In some experiments, evidence has been found that the (independent) single-vortex picture breaks down. In these cases, we briefly comment on the influence of vortex-vortex interactions.

A. Classical equation of motion

In this section, we review the steps to derive the equation of motion for a vortex. We analyze all contributions, i.e. its inertia, its dissipation, the external potential and the applied forces. To keep the notation simple we suppose, for the moment that the vortex moves along a given (say $\hat{x}$) direction with an average vortex velocity v_x.

Vortex mass - Moving vortices lead to phase changes across junctions and they therefore contribute to an electric energy. In principle all capacitances contribute, but as discussed before the main effect comes from the junction capacitance so that $E_{ch} = 1/2 \sum_{<ij>} C V_{ij}$). (The contribution due to C_0 will be discussed in Section III C.) In a quasi-static approach this sum is calculated by comparing the phase differences across each junction at times t and $t + 1/v_x$ (in units of the lattice constant): $\Delta\phi_{ij} = \phi_{ij}(t + 1/v_x) - \phi_{ij}(t)$. The electric energy then acts like a kinetic energy term and the proportionality factor defines the vortex mass [220–223]:

$$E_{ch} = \frac{1}{2} M_v v_x^2 \tag{59}$$

with

$$M_v = \frac{1}{8E_C} \sum_{<ij>} (\Delta\phi_{ij})^2 \ . \tag{60}$$

The problem of calculating the vortex mass is now reduced to finding the phase differences across junctions at times t and $t + 1/v_x$. Note, that Eq.(60) can be applied to various array geometries if the phase configuration around a vortex is known.

In large 2D Josephson arrays the arctan form given in Eq.(58) [224] is used to evaluate the sum in Eq. (60). With the assumption that this arctan-phase configuration remains the same when the vortex moves through the array, numerical evaluation of the phase differences in a large 2D square array yields the Eckern-Schmid value of the vortex mass

$$M_v = \frac{\pi^2}{4} \ E_C^{-1} \quad . \tag{61}$$

In this calculation roughly half of the vortex mass is due to the junction the vortex crosses; the other half comes from all the other junctions in the array. For a triangular 2D array, a similar calculation can be done and the vortex mass is twice the mass of a square array. For typical arrays with $C = 1$ fF and $a^2 = 10\ \mu\text{m}^2$, the vortex mass is 500 times smaller than the electron mass. This small value already indicates that quantum effects are likely to occur.

It has been shown [225] that near array edges the vortex mass vanishes when it approaches a free boundary of the array. These boundary effects are, however, negligible if the vortex is a few lattice spacings away from the edge. One can also include self-field effects. Currents

now extend over a distance of the penetration depth $\lambda_\perp$ from the vortex center so that the arctan approximation can no longer be used. As the vortex is effectively reduced in size, the sum of the V_i's can be restricted to those junctions which are $\lambda_\perp$ from the vortex center. The result is a smaller vortex mass and its decrease with decreasing $\lambda_\perp$ is given in Ref. [226]. The vortex mass is dependent on the E_J/E_C ratio as well. Quantum corrections to the mass, on approaching the S-I transition [227] are discussed in Section III C. To a good approximation it has the value given in Eq. (61) for arrays that are not in the critical region $E_J \sim E_C$.

The vortex mass can also be calculated in geometries other than two dimensional arrays. In a purely 1D array (N junctions in parallel connected by two superconducting leads), the vortex phase configuration is given by

$$\phi_i = 4 \arctan[\exp((x_i - x)/\Lambda_J)],$$

where x denotes the position of the vortex center. For $\Lambda_J < N$, the vortex has a kink-like shape, which extends over a distance of the order of Λ_J; for $\Lambda_J > N$ the vortex is spread out equally over the whole system with $\phi_{x+1} - \phi_x \approx 2\pi/N$. In this latter regime, $\Delta\phi_{t+1/v_x}(x+1,x) - \Delta\phi_{x+1,x}(t) = 2\pi/N$ and $M_v = h^2/(8E_C N^2)$. For $1 < \Lambda_J < N$ the sum can be computed numerically or in a continuum approximation. The sum over the phase differences squared is equal to $8/\Lambda_J$ [228] and hence

$$M_v^{1D} = \frac{1}{\Lambda_J}\, E_C^{-1} \quad \text{for} \quad 1 < \Lambda_J < N\ . \tag{62}$$

In other geometries, the phase configuration of a vortex is not exactly known. It can in principle be calculated. However, since a substantial contribution comes from the junction that the vortex crosses, Eq.(61) can be used as an estimate for the quasi-static vortex mass in these cases.

The notion that the concept of the vortex mass is not new in the theory of superfluids. It has been discussed extensively for type-II superconductors and superfluid He [229–231].

Dissipation - As the vortex is a macroscopic object, it couples to the environment and experiences dissipation. Quantum arrays generally have junctions that are underdamped, i.e., have a McCumber parameter $\beta_c > 1$. One might therefore expect that vortex motion is underdamped as well.

In the simplest approximation one can assume that a moving vortex experience a viscous drag force characterized by a viscous coefficient η. In a Bardeen-Stephen like model η is calculated using the following argument. The total power loss is the sum of all the resistive losses in the junctions. Assuming R_e to be identical for all junctions, the sum in the total power is the same as in the calculation of the vortex mass. For example,

$$\eta = \frac{\Phi_0^2}{2R_e}$$

for a large square 2D array. Here, R_e is the effective voltage-bias resistance, i.e., the effective shunt resistance of each junction. At low temperatures R_e is the subgap resistance which is many orders of magnitude larger than the normal state resistance, indicating the vortices can move through the medium with negligible damping. However, the simple model presented here does not take into account other sources of dissipation like the coupling to the low lying modes of the array (spin-waves) or quasi-particle tunneling (see next sections).

Lattice potential - The total Josephson energy associated to a vortex configuration (calculated for example by means of Eq.(58)) depends on the vortex position. The energy has a minimum value when the vortex is in the middle of a cell; the maximum value is reached when the vortex right on top of a junction. Neglecting vortex-vortex interaction and the influence of the array edges, vortices are only subject to a periodic lattice potential:

$$U_v(x) = \frac{1}{2}\gamma E_J \sin(2\pi x) \quad .$$

Here, γ is the energy barrier in units of E_J a vortex has to overcome when moving from one cell to the next. In large 2D arrays with no self fields, $\gamma = 0.2$ in a square geometry. In a triangular arrays the barrier is about a factor five lower, $\gamma = 0.043$ [224]. Inclusion of self-field effects can be done and γ increases dramatically for $\lambda_\perp < 1$ [219]. In contrast, there is no energy barrier in 1D arrays if $\Lambda_J > 1$ [232].

Equation of motion for a single vortex - A vortex in a Josephson array moves under influence of a Lorentz force $\Phi_0 I$ in a direction perpendicular to the current flow. The phenomenological damping term and the periodic lattice potential $U(x)$ provide additional forces.

Gathering all the ingredients discussed so the equation of motion can be written as:

$$M_v \ddot{\mathbf{r}} \; + \; \eta \dot{\mathbf{r}} \; = \; -\nabla_{\mathbf{r}} U_v \; - \; \Phi_0 \hat{\mathbf{z}} \times \mathbf{I} \tag{63}$$

where $\mathbf{r}$ is the vortex position, $\mathbf{I}$ is the applied current per junction and $\hat{\mathbf{z}}$ is the unit vector perpendicular to the array [233].

The dynamics can be visualized as that of a massive particle moving in a washboard potential analogous to the dynamics of a single junction in the RCSJ model. For the junction problem, the motion is in artificial ϕ-space; for the vortex problem the motion is in real space. The mapping is exact for $2\pi x \;\rightarrow\; \phi$ indicating that vortices in arrays produce the same dynamics as a single junction with a critical current of $\gamma I_c/2$ per junction, a McCumber parameter $\beta_{c,v} = \gamma\beta_c$ and a plasma frequency $\omega_{p,v} = \sqrt{\gamma}\omega_p$.

Numerical evidence for massive vortices has been found by Hagenaars *et al.* [234]. Their data show that a vortex may be reflected at an array edge, thereby changing its sign (i.e., it becomes an antivortex). This behavior can be qualitatively understood within the model of a massive vortex interacting logarithmically with the image vortices outside the array. In the same paper the authors also note that the way in which vortex inertia manifests itself depends on the dynamical situation considered.

In the next three subsections, we first summarize the experimental details on classical arrays with $\beta_{c,v} > 1$ and then discuss two phenomena that are not included in Eq. (63). First, experiments show that vortices in highly underdamped arrays experience more damping than can be expected from the simple approach we followed above. As it turns out coupling to spin waves becomes dominant in these arrays. Second, we review the theoretical and experimental results on the Hall effect.

1. Experiments on classical, underdamped arrays

In Fig.30 a typical example [235,236] of a current-voltage I-V characteristic of a classical 2D array is shown. The applied magnetic field corresponds to $f = 0.1$. At low temperatures,

hysteresis near the depinning current indicates that $\beta_{c,v} > 1$, consistent with the existence] of a mass term in the equation of motion. The depinning current itself is close to the expected value of $(\gamma/2)I_c = 0.1I_c$ per junction. From the analogy with the single junction problem, a RCSJ-like I-V characteristic is expected. This is generally not observed. The I-V curves, instead, show a slight bending in the direction of the voltage axis opposite to what is expected from the single-junction analogy. This is also seen in simulations on the properties of a single vortex in a 2D array with periodic boundaries [237]. Their numerical data points at a nonlinear viscous damping of the form:

$$\eta = \frac{A}{1 + Bv_x}$$

where the A and B depend only on the McCumber parameter of the junctions.

For currents well above depinning (above 50 μA and not visible in Fig.30), the flux-flow state becomes unstable. The I-V enters a row-switched state [105] where rows of junctions across the whole array width start to oscillate coherently [238]: all phases rotate continuously in time with a phase shift between them. In this regime, a description of the array in terms of vortex motion is no longer appropriate.

One should realize that the I-V curve was recorded at an applied magnetic flux of 0.1 Φ_0 per cell ($f = 0.1$). Thus, on average there is approximately one vortex per $1/f$ cells so that the distance between vortices is only three cells. At such a short distance, vortices will interact with each other. The influence of these vortex-vortex interactions on the measured I-V characteristics is not known in detail.

2. Spin-wave damping

As shown in Fig.30 experimental I-V characteristics in the flux-flow regime are generally more or less straight lines. Neglecting the influence of the pinning potential U_v, Eq.(63) indicates that for high bias the slope of this line should approach a conductance value corresponding to $1/(2fR_e)$ per junction. The I-V curves therefore provide a way to estimate R_e in the regime where vortices are driven with relatively large currents.

A systematic study on highly underdamped arrays has been performed by the Delft group [239]. The surprising result is that for the most underdamped arrays R_e is much lower than the normal-state resistance. Such a low resistance cannot be explained by the Bardeen-Stephen model. Apparently, vortices, when driven with a *large current*, experience more damping than can be explained by ohmic dissipation alone. A similar conclusion was drawn by Tighe *et al.* [240], who concluded that in their underdamped arrays vortices moved in an overdamped manner.

Several authors have suggested the possibility that energy can be lost in the wake of the moving vortex [235,239,240]. The effective viscosity due to coupling to spin-waves can be calculated in a semi-quantitative model [239] using the following argument: The oscillating part of the junction is modeled by an $L_J - C$ circuit and the voltage drop across it is $V = \Phi_0 v \Delta\phi/(2\pi)$ which occurs for a time interval of the order of v^{-1}. As a response to this voltage step the phase difference starts to oscillate (note that at the same time the average phase advances when the vortex moves across the junction). Equating the total

power dissipated in the $L_J - C$ circuit to $\eta_{sw} v^2$, the result for the effective viscosity due to the plasma oscillations (in square two-dimensional arrays) is

$$\eta_{sw} = \frac{1}{\pi} \frac{\Phi_o^2}{2N} \frac{1}{\sqrt{L_J/C}} \quad .$$

When comparing this viscosity coefficient to the Bardeen-Stephen viscosity coefficient,

$$\frac{\eta_{sw}}{\eta_v} \sim \frac{R_e}{\sqrt{L_J/C}}$$

one sees that the more underdamped the arrays are, the more dominant the damping due to energy lost in the wake of the vortex becomes.

These observations have been confirmed by more systematic calculations discussed in Section III C. In particular it is possible to obtain a self-consistent picture of vortex dynamics which includes the interaction with its environment. There are two main advantages for discussing the dynamics from this perspective. Firstly it is possible to evaluate quantum corrections to the classical equation of motion and secondly it is possible to analyze the quantum dynamics in detail.

3. The Hall Effect

In addition to the Lorentz force which is due to the external current, a vortex is subject to a Magnus force which is transverse to vortex velocity. The study of the Magnus force in superfluids has a very long history. A detailed discussion is outside the scope of this review (see Ref. [241] and references therein). In Josephson arrays, in presence of a gate to the ground plane, particle-hole symmetry is broken. A vortex feels a Magnus force [242,243] given by

$$\mathbf{F} = Q_x \Phi_0 \hat{\mathbf{z}} \times \dot{\mathbf{r}} \; . \tag{64}$$

Here we assumed for simplicity a homogeneous gate charge. As a result of the combined effect of the Magnus force and the Lorentz force, the vortices move at a certain angle, the Hall angle, with respect to the current. Its measurement yields informations on the different dissipation sources in the system. Combining all the terms the equation of motion in the stationary limit the vortex moves at a constant velocity $\mathbf{v} = [v_x, v_y] = [v \cos\theta_H, v \sin\theta_H]$ obeying the following equations

$$\begin{aligned} \eta v \cos\theta_H &= I_y \Phi_0 - Q_x v \Phi_0 \sin\theta_H \\ \eta v \sin\theta_H &= Q_x v \Phi_0 \cos\theta_H \end{aligned} \tag{65}$$

lead to the resistance tensor

$$\begin{aligned} R_{xx} = R_{xx} &= \frac{\Phi_0^2/\eta}{1 + (Q_x \Phi_0/\eta)^2} \\ R_{xy} = -R_{yx} &= \frac{Q_x \Phi_0^3/\eta^2}{1 + (Q_x \Phi_0/\eta)^2} \end{aligned} \tag{66}$$

and to the Hall angle θ_H

$$\tan\theta_H = \frac{Q_x \Phi_0}{\eta} \tag{67}$$

The main consequence of the previous results is that the Hall effect should be larger in low resistance samples.

In experiments on classical Josephson arrays the Hall angle is usually found to be very small (see e.g. Ref. [244]). Samples are usually characterized by random offset charges and as a result the Magnus force averages to approximately zero. However, up to now there is no general agreement on this explanation. From a theoretical point of view there are questions related to the derivation of Eq.(64) from first principles.

In Ref. [242] the Magnus force was obtained from the QPM, implying that only the external charge enters in determining the Hall angle. A reexamination of the problem by Makhlin and Volovik [245] related the (apparent) absence of the Hall angle to the near exact cancellation of the Magnus force with the spectral-flow force. On deriving the effective action from the BCS Hamiltonian Volovik [246] shows that the offset charges, contributing to the Hall angle, have two different physical origins. In addition to the one stemming from the coupling to the ground plane, there is an additional contribution which depends on the particle-hole asymmetry of the spectrum. This latter term is of the order of the small factor $(\Delta/E_F)^2$, with E_F being the Fermi energy. This confirms the expectation that the Hall angle should be small in Josephson arrays [247].

In *quantum* Josephson arrays Hall measurements have been performed by the Chalmers group [161,248]. Their results are shown in Fig.31. The transverse resistance is odd in the magnetic field. Combining the results for the longitudinal and transverse part the Hall angle can be extracted. Comparing the results with the classical results [244], the Chalmers experiments indicate a larger Hall angle. The only apparent difference is the smaller ratio E_J/E_C and this is consistent with the theoretical expectation that the offset charges are responsible for the Hall effect. It is reasonable to expect that these have a negligible effect on approaching the classical limit.

Finally, it is worth mentioning that the field-tuned transition discussed previously also manifests itself in R_{xy}. An interesting feature which still remains unexplained is that R_{xx} andR_{xy} are related by the following empirical relation

$$R_{xy} \sim \frac{\partial R_{xx}}{\partial f} \tag{68}$$

similarly to what happens in the Quantum Hall effect.

B. Ballistic vortex motion

Besides the experimental verification of the mass term in the equation of motion [235,240] a considerable interest was focused on the direct observation of the ballistic motion. Ballistic vortex motion has not only been observed in long continuous junctions [249], where energy barriers for cell-to-cell motion and spin-wave coupling are absent, but also in discrete 1D arrays [250–252] and in 2D aluminum arrays [253]. The idea goes as follows: If vortices are

massive particles, they should keep on moving if the current is turned off. In an experiment, this concept can be realized by accelerating vortices up to a high velocity v_0 so that their kinetic energy is much larger than the lattice potential. With Eq.(63) one finds that $v_0 \approx \Phi_0 I/\eta$ if one neglects the lattice potential. Then, these fast-moving vortices can be launched into a force-free environment where voltages probes can be used to detect their path through this region.

The observation of ballistic motion is only possible in a velocity window ($v_{min} < v < v_{max}$) bound from below by the presence of the pinning potential and from above by the various damping mechanisms which set in at high velocities. The criterion $E_{kin} \geq E_{pot}$ translates into a lower bound for the vortex velocity required to observe ballistic motion

$$v_{min} = \frac{\sqrt{\gamma}\omega_p}{\pi} \ . \tag{69}$$

Note, that for a 1D system with $\Lambda_J > 1$, $\gamma \approx 0$ so that the minimum vortex velocity is small.

The vortex velocity cannot be chosen arbitrarily large. Fast moving vortices can trigger row switching in the array [105,254]. Simulations [255] indicate that in 2D arrays the vortex velocity must be limited to $v < \omega_p$. Another limitation comes from coupling to spin-waves. In 2D arrays, there is a threshold vortex velocity below which this coupling is weak. It has been shown [256,257] that a moving vortex only couples to spin-waves above $v_{max} \approx 0.1\omega_p$. The requirement that

$$\frac{\sqrt{\gamma}\omega_p}{\pi} < v < 0.1\omega_p$$

indicates that ballistic motion is possible in triangular arrays just above depinning. (Quantum fluctuations make the window larger; details are discussed in the next section.)

Let us analyze the ballistic motion using Eq. (63). With no current applied and for vortices launched at high enough velocity (to ignore pinning effects), the equation of motion reduces to

$$M_v \dot{v}_x \ + \ \eta v_x \ = \ 0 \quad ,$$

indicating that the vortex velocity decreases exponentially in time as $v_x = v(0)\exp[-M_v t/\eta]$. A mean free vortex path can then be defined as

$$\lambda_{free} \ = \ \frac{v(0)M_v}{\eta} \ = \ \pi^{-1}\frac{I}{I_c}\,\beta_c \ , \tag{70}$$

for a square 2D array. The factor $I/\pi I_c$ is typically of order 0.1 so that at high temperatures with $R_e = R_N$, $\lambda_{free} \approx 1$. At low temperatures with $R_e \gg R_N$ (the corresponding β_c can be high as 10^7), $\lambda_{free} \gg 1$.

The experiment with 2D arrays was performed by van der Zant *et al.* [97] using the sample configuration shown in Fig.32. It consists of two 2D arrays which are connected by a narrow channel of 20 cells long and 7 cells wide. Superconducting banks on both side of the channel confine the vortices in the channel and, in order to reduce the influence of the lattice potential, the arrays and the channel were made in a triangular geometry.

In the array on the left hand side, vortices generated by a small magnetic field, are accelerated up to a high velocity. Some of these high-energetic vortices will enter the channel

and will then be launched into the detector array (array on the right hand side). There is no driving current applied to this array. A set of voltage probes around the detector array is used to detect the places where vortices leave the force-free environment. (The voltage measured across two probes is proportional to the number of vortices passing the probes per unit time.) The results of the local voltage drops as a function of temperature it is shown in Fig.33. At high temperatures, vortices move diffusively and voltages are observed between all voltage probes. As a consequence, the voltage across the probes V3 and V10 is much smaller than the channel voltage.

At low temperatures, the voltage measured between the two probes situated just opposite to the channel is almost equal to the channel voltage. Vortices cross the second array in a narrow beam (see Fig.32). This ballistic vortex motion is observed for $T < 500$ mK, for small applied magnetic fields ($0.01 < f < 0.025$) and for currents just above depinning. For high magnetic fields, vortex-vortex interactions start to play a role when more than one vortex is in the channel at the same time and for too high currents coupling to spin-waves probably starts to play a role.

C. Effective single vortex action

In this Section we derive a more general approach to describe the single vortex dynamics which incorporates the coupling to spin-waves and which is also valid in the quantum regime where $E_J \approx E_C$ [130,227,258]. After introducing the effective vortex action, we first consider the classical limit and show that all known results can be recovered. We then proceed to the quantum regime. The vortex mass is calculated as well as the velocity above which spin-wave damping starts to become effective.

As discussed in Appendix E, the effective action for a single vortex is given by

$$S_{eff} = \frac{1}{2} \sum_{a,b=x,y} \int d\tau d\tau' \dot{r}^a(\tau) M_{ab}[\mathbf{r}(\tau) - \mathbf{r}(\tau'), \tau - \tau'] \dot{r}^b(\tau'),$$

$$M_{ab} = \sum_{jk} \nabla_a \Theta(\mathbf{r}(\tau) - \mathbf{r}_j) \langle q_j(\tau) q_k(\tau') \rangle \nabla_b \Theta(\mathbf{r}_k - \mathbf{r}(\tau')) \tag{71}$$

($\Theta(\mathbf{r}) = arctan(y/x)$). Thus, *vortex dynamics is governed by the charge-charge correlation*, which depends on the full coupled charge-vortex gas. The effective action Eq.(71) describes dynamical vortex properties in the whole superconducting region and is therefore a good starting point for the investigation of vortex properties down to the S-I transition. The cumulant expansion that leads to Eq.(71) is correct in the $E_J \gg E_C$ limit where the charges can be considered as continuous variables and where the vortex fluctuations can be disregarded. In general the average defined in Eq.(E1) is far from being gaussian so that one may argue that higher order cumulants should be considered. Nevertheless nothing prevents us to analyze Eq.(71) keeping in mind that a full description of vortex motion may require the analysis of a dynamical equation that contains also terms proportional to higher powers of the vortex velocity.

The expression given in Eq.(71) reproduce the known results in the classical limit where $E_J \gg E_C$. In this region of the phase diagram the charges may be considered to be continuous variables and vortex fluctuations may be neglected so that the charge-charge correlation

reads

$$\langle qq \rangle_{k,\omega_\mu} = E_J k^2 \frac{1}{(\omega_\mu^2 + \omega_k^2)}$$

and

$$\omega_k^2 = \frac{4e^2 E_J}{C_0} \frac{k^2}{1 + \lambda^2 k^2} \quad .$$

The spin-wave dispersion is described by ω_k. It is optical, i.e. $\omega_k = \omega_p$, for long range Coulomb interactions, whereas for on-site interactions we have $\omega_k = \bar{\omega}_p k$. Here $\bar{\omega}_p = \sqrt{4e^2 E_J / C_0}$ is the plasma frequency for the case of on-site Coulomb interactions.

The action (71) reduces to that of a free particle in the limit of small velocities $\dot{r}(\tau)$. The corresponding adiabatic vortex mass M_v is

$$M_v = \int_0^\beta d\tau M_{xx}(0, \tau) \ ,$$

which reduces in the classical limit to

$$M_v = \frac{\pi^2}{4E_C} + \frac{\pi C_0}{4e^2} \ln(L)$$

with L the array dimension. Thus both C_0 and C yield a contribution to the mass. The self-capacitance contribution depends on the system size L. For generic sample sizes and capacitance ratio's the size-dependent contribution is smaller than the Eckern-Schmid mass (the value in Eq. (61)). The effect of a uniform background charge on the vortex mass was considered by Luciano *et al.* [259,260]. The frustration of charging leads to a renormalization of the mass towards the classical value.

The spin-wave damping that a moving vortex experiences may also be calculated from Eq.(71). Varying the vortex coordinate $r^a(\tau)$ in Eq.(71) yields the equation of motion

$$2\pi \epsilon_{ab} I_b / I_c = \partial_\tau \int d\tau' M_{ab}(r(\tau) - r(\tau'), \tau - \tau') \dot{r}^b(\tau') \tag{72}$$

($\epsilon_{xx} = \epsilon_{yy} = 0, \epsilon_{xy} = -\epsilon_{yx} = 1$). Its constant velocity solutions in the presence of an external current determine the non=linear relation between driving current and vortex velocity (i.e. the current-voltage characteristics), once the charge-charge correlation is analytically continued to real frequencies (i.e., if $i\omega_\nu \to \omega + i\delta$) [256]. The relevant information is contained in the real part of Eq.(72), which reads in Fourier components and for a constant vortex velocity

$$I^y / I_{cr} = \frac{v}{4} \int d\omega \int d^2k \frac{k_y^2}{k^2} \delta(\omega - v k_x) [\delta(\omega - \omega_k) + \delta(\omega - \omega_k)] \ . \tag{73}$$

The delta functions express the spin-wave dispersion (from the analytic continuation of the charge-charge correlation) and the vortex dispersion respectively. The overlap integral determines the amount of dissipation a moving vortex suffers from coupling to spin-waves. Adopting the smooth momentum integration cut-off, introduced in Ref. [221], one recovers in the classical limit the results of Refs. [256,257].

While the static damping is zero for vortex velocities below threshold (which implies the possibility of ballistic motion), a dynamical friction due to the coupling to the plasma oscillations is always present for frequencies higher than a given frequency threshold [261]. The latter contribution approaches to zero when the velocity increases to the threshold velocity. However, radiative dissipation of the vortex affects the threshold for ballistic motion. What is important in this analysis is that by changing the frequency of the applied current, one is able to extract the domain of validity where a vortex can be defined as a macroscopic object.

Inclusion of quantum effects contributes to the opening of a more robust velocity interval where ballistic motion can be observed. When the ratio E_J/E_C decreases the charge-charge correlation must be calculated beyond the classical approximation: The discreteness of charge transfer has to be taken into account, which is in particular important at short distances. For long range Coulomb interactions and in the absence of vortex fluctuations the charge-charge correlation function may be rewritten as

$$\langle qq \rangle_{k,\omega_\mu} = \frac{k^2 E_J}{\omega_\mu^2 + \bar{\omega}_k^2}, \quad \bar{\omega}_k^2 = \omega_k^2 + 4\pi^2 E_J \xi^2 k^2. \tag{74}$$

where the correlation length is

$$\xi^2 \sim \sqrt{\frac{E_C}{E_J}} \left(\pi e^{-\sqrt{E_C/E_J} c/\pi} \right)^{\frac{1}{1-\delta}}, \quad \delta = \sqrt{\frac{E_C}{E_J \pi^2}}$$

and the constant c is of order one. The S-I phase transition takes place at $E_J/E_C = 1/\pi^2$. Thus, without vortex fluctuations the phase transition is at a smaller E_J/E_C value than the $2/\pi^2$ that follows from a duality argument [91]. The spin-wave dispersion is affected at small distances (large k) and the mass is now given by:

$$M = \frac{\pi}{16 E_C \xi^2} \ln \left[1 + 4\pi \xi^2 \right]$$

In the limit of small ξ the Eckern-Schmid mass is recovered. An extrapolation to the S-I transition where $\xi \to \infty$ yields a mass that vanishes at the transition.

With the charge charge correlation given in Eq.(74) we may calculate the spin-wave damping of vortex motion due to the coupling to spin-waves beyond the classical limit. Replacing ω_k by $\bar{\omega}_k$ in Eq.(73), the overlap integral over the delta functions only contributes for vortex velocities that are higher than a threshold velocity

$$v_{max} \sim \xi \sqrt{8 E_J E_C}$$

By taking into account quantum effects the spin-wave spectrum enlarges the velocity window in which vortices move over the lattice potential without emitting spin-wave. An extrapolation to the S-I transition yields a diverging threshold Velocity so that vortices and spin-waves decouple. Note, that the outcome of this calculation also has consequences for the classical equation of motion. For instance, it shows that coupling to spin-wave dissipation is reduced for velocities $< 0.5\omega_p$. This value is a factor five higher than expected from classical considerations [256,257].

Spin-wave damping is not the only source of dissipation. Vortices, in their motion, can excite quasi-particles as well if the local voltage drop (due to the finite velocity) exceeds the quasi-particle gap. The effect of quasi-particles damping on vortex motion was considered in Ref. [262]. In this case the equation of motion takes the form

$$\ddot{\mathbf{r}} + \eta\dot{\mathbf{r}} - \eta\Delta \int^{t} dt' \, \mathrm{sinc}[2\Delta(t-t')] \frac{\dot{\mathbf{r}}(t')}{\pi|\mathbf{r}(t)-\mathbf{r}(t')|^2} = -\Phi_0 \hat{\mathbf{z}} \times \mathbf{I} \tag{75}$$

where $\mathrm{sinc}x \equiv (2/\pi x)\sin x$. Despite the nonlinear form of the damping kernel, Choi *et al.* [262] showed that the frictional force on a vortex is linear in the vortex velocity for any practical purpose (in particular in the long-time and long-wavelength limit, where the semiclassical equation of motion is mostly concerned).

D. Quantum vortices

If vortices are massive particles that move ballistically, one can think of them as quantum mechanical objects. Like an electron, a vortex in a periodic potential will have a Bloch wave function with momentum $p = \hbar k$ and thus a wavelength of h/vM_v. At present, many experiments have verified the concept of a quantum vortex [51,53,235,240,263–265]. In this chapter, we discuss three examples: macroscopic quantum tunneling of vortices [51,53,235,240], the observation of vortex interference in a hexagon-shaped array [266] and Bloch oscillations of vortices in the periodic lattice potential [267].

1. Macroscopic quantum tunneling of vortices

In a classical description vortices oscillate in the minima of the washboard potential with frequency $\omega_{p,v}$. In quantum arrays, these oscillations are quantized. To estimate when quantum fluctuations in the vortex position become important, we compare the zero-point energy $\frac{1}{2}\hbar\omega_{p,v} = \frac{1}{2}\sqrt{8\gamma E_J E_C}$ to the energy barrier $U_{\mathrm{bar}} = \gamma E_J$. The two energies are equal if $E_J/E_C = \sqrt{2/\gamma}$. In this quantum vortex regime, the zero-point fluctuations are large enough to allow for quantum tunneling of vortices.

In Fig.34, the resistance per junction (linear response) as a function of temperature is given for two square arrays [51]; in the classical (a) and in the quantum regime (b). The resistance of the classical array decreases exponentially all the way down to the lowest temperatures. The slopes define the barrier for this thermally activated process: $R \propto \exp\left[-U_{\mathrm{bar}}/k_B T\right] = \exp\left[-\beta\gamma E_J\right]$. In contrast, the resistance of the quantum array levels off at a temperature T_{cr} below which it remains constant. We denote this constant value with R_c. Above T_{cr}, again thermally activated behavior is observed. Similar resistance curves have been reported by the Chalmers group [53].

A first estimate of the tunnel rates and of R_c can obtained from the analogy with the single-junction problem. In the moderate damping regime [268]:

$$R_c \approx 140 R_Q f \sqrt{S} \mathrm{e}^{-S} \tag{76}$$

where the action S is given by

$$S = \sqrt{0.95 \frac{\gamma E_J}{E_C}} \left(1 + \frac{0.87}{\sqrt{\beta_{c,v}}}\right) . \tag{77}$$

The $\sqrt{E_J/E_C}$ dependence of the critical resistance, implied by the previous equation, has indeed been reported by the Chalmers group [53].

An estimate for T_{cr} can be obtained by equating S to $\gamma E_J/T_{cr}$. Neglecting the term with $\beta_{c,v}$, the result is:

$$E_J/T_{cr} = \frac{2.5}{\sqrt{\gamma}} \sqrt{\frac{E_J}{E_C}} . \tag{78}$$

With E_J of the order of E_C, the inverse normalized critical temperature (E_J/T_{cr}) is typically somewhat larger than 2.5 in agreement with the data.

Comparing the measured values of R_c with the estimates given in Eq.(76) and Eq.(77), the tunnel rates in the measurements are lower than expected even when taking R_N as the resistance determining $\beta_{c,v}$. A smaller R_c is consistent with a single vortex model in which the vortex mass is an order of magnitude larger than the one calculated in the quasi-static approximation. It is likely that vortices do not move as rigid objects and calculations have shown that the dynamic band mass of a vortex can be an order of magnitude larger [269]. However, considering this uncertainty, no definite conclusion about the validity of the single-junction model can be drawn for the observed flattening of the resistance. Other models like collective tunneling cannot be excluded.

A surprising result is that the array (a) in Fig.34 does not show any signature of quantum tunneling. Our simple argument given above indicates that for this array the zero-point energy is of order $U_{\rm bar}$. The absence of quantum tunneling is explained by the fact that in Fig.34 the measured energy barriers are of order E_J, instead of $0.2E_J$. The Delft group has reported [51] a systematic increase of the measured energy barrier in the range $2 < E_J/E_C < 20$. This increase is not yet understood.

The theoretical analysis of inter-site vortex tunneling in Josephson arrays was first formulated by Korshunov [270,271] who evaluated the instanton action S_{inst} associated to vortex tunneling between adjacent plaquettes. S_{inst}, related to a hop from one plaquette to a neighboring one, determines tunnel rates and the depinning current. It can be obtained in the language of the Coupled Coulomb gas approach [92] by evaluating the action associated with the trajectory

$$\dot{v}_{i,t} = v_{i,\tau+\tau_\epsilon} - v_{i,\tau} = \delta_{\tau,t}[\delta_{i,x+1} - \delta_{i,x}]$$

for a hop from $x, \tau \to x+1, \tau+\tau_\epsilon$, with the result (see Eq.(71))

$$S_{inst} = \frac{1}{2} M_{xx}(0,0).$$

In the limit of large Josephson coupling one recovers all known results, i.e. for general capacitance matrix

$$S_{inst} = \frac{\pi E_J}{4\omega_p} \left[\sqrt{\pi}\sqrt{\lambda^2 + 4\pi} + \frac{\lambda^2}{2} \ln\left(\frac{2\sqrt{\pi}}{\lambda} + \sqrt{1 + \frac{4\pi}{\lambda^2}}\right)\right] . \tag{79}$$

It reduces to $S_{inst} = \pi^{3/2} E_J/4\bar{\omega}_p$ and $S_{inst} = \pi^2 E_J/2\omega_p$ for $C = 0$ and $C_0 = 0$ respectively.

Korshunov pointed out that instanton-instanton interaction cannot be neglected. Vortex tunneling is incoherent in the temperature range $E_J \gg T \gg \sqrt{E_J E_0}$. In this case the tunneling probability W is given by

$$W \sim \frac{E_J^{1/2} e^{-S_{inst}}}{T^{3/2}} e^{2\pi \ln 2T/E_J}$$

up to the crossover temperature $T \sim \sqrt{E_J E_0}$ where the activated behavior takes place.

Dissipation associated to vortex tunneling was discussed by Ioffe and Narozhny [272]. Since the the time associated to vortex tunneling is slow compared to Δ^{-1}, the dissipation which accompanies this process arises from rare processes when a vortex excites a quasi-particle above the gap. These authors find that this source of dissipation can be significant even in the adiabatic limit.

2. Vortex interference: the Aharonov-Casher effect

In 1984 Aharonov and Casher [273] studied the interference of particles with a magnetic moment moving around a line charge. This AC effect is the dual of the Aharonov-Bohm effect [274] that describes quantum interference of charged particles moving around magnetic flux. The AC effect has first been observed using neutron beams in Ref. [275]. The concept of vortex-interference in superconductors has been introduced by Reznik and Aharonov [276] and their ideas have been adapted to ring-shaped Josephson arrays by van Wees [277] and by Orlando and Delin [278]. Although there are similarities with the conventional AC effect, there are important differences. In JJAs vortices do not carry a flux unlike the Abrikosov vortices in a bulk superconductor. Moreover, as already stressed, JJAs form an artificial 2D space. The observation of the AC effect for vortices has been reported by Elion *et al.* [266], only two years after the first theory papers [277,278] appeared.

In the array of Elion *et al.*, vortices follow trajectories indicated as dotted lines in the Fig.35. The sample consists of a hexagon-shaped array with six triangular cells. Large-area junctions couple the hexagon to superconducting banks so that only two paths for vortex motion are possible. The large-area junctions confine vortices to the hexagon, but the coupling to the superconducting banks is not so strong that phases of the islands are set by the banks. A gate controls the charge on the superconducting island in the middle of the hexagon.

In the experiment the differential resistance in the flux-flow regime has been measured as a function of the gate voltage. When fixing the current through the array, clear oscillations in the differential resistance are observed. The measured period, however, corresponds to e, half the value expected from theory. The factor of two arises from tunneling of quasi-particles which effectively limit the quantum phase difference to values in the range $-\pi/2$ to $\pi/2$. (Quasi-particle tunneling changes the vortex phase difference by π and becomes favorable as soon as the induced charge equals $e/2$, i.e. when the phase difference equals $\pi/2$.)

It is possible to derive the AC effect from the Quantum Phase Model. In a more transparent way, although less rigorous, one starts from the representation of the partition function

as a path integral over the phases and charges (see Eq.(D2)) with the inclusion of a uniform background charge, i.e. $q \longrightarrow q - q_x$. The term in the action of the QPM which is relevant for the AC effect is the one which is linear in $\dot{\phi}_i$ in Eq. (D2). If a vortex is present, the configuration of the phases will be related to its position $\mathbf{r}(\tau)$ and, by going over the same steps that lead to the single vortex action in Eq. 71, there is an additional term to the effective action equal to

$$S_{AC} = -i \sum_i \frac{q_{x,i}}{2e} \int_0^\beta d\tau \dot{\mathbf{r}} \cdot \nabla \Theta \left[\mathbf{r}_i - \mathbf{r}(\tau)\right] \tag{80}$$

Eq.(80) defines a pseudo-charge gauge field for the vortex

$$2e\mathbf{A}_Q(\mathbf{r}) = q_x \hat{\mathbf{z}} \times \mathbf{r}/r^2$$

which is singular at the origin of the vortex. Thus the external charge act like a vector potential for the vortex. The phase factor χ implied by Eq.(80) is

$$\chi = 2\pi \sum_{i \subset \Gamma} \frac{q_{x,i}}{2e} \tag{81}$$

where the sum extends to all islands enclosed by the trajectory Γ .

3. Bloch oscillations

Electrons in metals move in the periodic potential created by the positively charged ions. The electron wave functions overlap and energy bands are formed. A constant electric field accelerates electrons, but in the absence of scattering, electrons would be Bragg reflected at the Brillouin zone edges. Electrons then undergo an oscillatory motion in space (Bloch oscillations). No charge would be transported. In metals scattering takes place before the electrons can reach the zone edge so that Bloch oscillations do not appear. In semiconductor superlattices [279] Bloch oscillations have been observed because of the larger superlattice period and because of less scattering in the controlled fabricated structures. Coherent Cooper pair tunneling in current bias Josephson junctions leads to a phenomenon analogous to Bloch oscillations [280].

Vortices in a periodic potential should also from energy bands. It is possible to study Bloch oscillation for vortices [267] in a quasi-1D Josephson array that is a few cells wide and 1000 cells long. A sketch of the sample layout is shown in Fig.36. For low densities, the bus-bars force the vortices to move in the middle row so that they experience a purely 1D sine potential. For a free vortex the energy depends quadratic on the wave vector k: $E(k) = k^2/2M_v$, which equals $E(k) = 2E_C$ at the Brillouin zone edge. In a periodic potential, energy gaps open up at the zone edges. The gap is equal to the Fourier coefficient of the lattice potential [281]. For a sine potential $\frac{1}{2}\gamma E_J \sin(2\pi x)$, the gap is then γE_J. Thus, vortices in arrays form energy bands with a bandwidth of the order E_C and an energy gap of $\frac{1}{2}\gamma E_J$ as illustrated in Fig.37. Assuming the lowest band to be cosine-shaped ($E(k) = \frac{1}{2}E_C(1 - \cos(k))$), the equation of motion $F = \hbar \mathrm{d}k/\mathrm{d}t$ is:

$$\hbar \frac{\mathrm{d}k}{\mathrm{d}t} = \Phi_0 I - \eta v(k) \quad \text{where} \quad \eta u(k) = \frac{1}{\hbar}\frac{\mathrm{d}E(k)}{\mathrm{d}k} = \frac{E_C}{2\hbar}\sin(k). \tag{82}$$

As defined before, I denotes the applied current per junction, η the phenomenological viscosity and $v(k)$ the average vortex velocity.

In the absence of damping, with a small current applied, the wave vector changes linearly in time: the vortex thus reaches the Brillouin zone edge where it will be Bragg reflected. This Bragg reflection results in an oscillatory motion in k-space. On average the vortex velocity is zero and the time it takes the vortex to complete one oscillation follows from $\Delta t = \Delta k / < \mathrm{d}k/\mathrm{d}t >$ with $\Delta k = 2\pi$. The corresponding Bloch oscillation frequency (ν_B) is:

$$\nu_B \;=\; \frac{I}{2e}\,, \tag{83}$$

and the amplitude of the oscillation is

$$x \;=\; \int \frac{1}{\phi_0 I} \;=\; \frac{E_C}{E_J}\,\frac{I_c}{\pi I}. \tag{84}$$

When biasing an array with 1000 junctions with currents of the order of μA, Bloch frequencies are in the range 1-10 GHz. Since $E_C \approx E_J$ and I_c/I is typically 100, the Bloch oscillations extend over 10 cells.

A characteristic feature of Bloch oscillating vortices is a nose-shaped form of the dc current-voltage characteristic (see Fig.38). For very small bias, there is a small supercurrent because vortices need to overcome the energy barriers near the array edges (finite-size effect). Just above the depinning current, any amount of dissipation prevents vortices from reaching the zone edges. Bloch oscillations do not exist in this regime and an increase of the current yields an increase of the measured voltage across the array.

When increasing the current beyond some point, dissipation is not strong enough to prevent the vortices from reaching the zone edges. Bloch oscillations are now possible. In the I-V characteristic a sudden decrease of the voltage is then expected with a negative differential resistance: the oscillating vortices do not contribute to the net transport of vortices through the array. Eqs.(82) can be solved with the result

$$V(I) = n\pi \frac{E_C}{e}\,\frac{I}{I_0} \qquad\qquad \text{if} \quad I < I_0 \tag{85}$$

$$V(I) = n\pi \frac{E_C}{e}\,\frac{I}{I_0}\sqrt{(1-\sqrt{1-\left(\frac{I_o}{I}\right)^2})} \qquad \text{if} \quad I > I_0, \tag{86}$$

where $I_0 = \eta E_C W/(2\Phi_0)$ and n is the one-dimensional vortex density (=number of vortices divided by the number of cells in the direction of motion). The solid line in Fig.38 is a fit to these equations. (The line is offset by a small positive current to correct for the depinning current). Although the overall shape of the experimental curve resembles that of the theoretical prediction, the experimental value of the band width (E_C is the previous discussion) is one order of magnitude smaller than expected. This discrepancy is not understood, but is consistent with a vortex mass that is larger than the calculated, quasi-static vortex mass. Note that the data extracted from the study of the macroscopic quantum tunneling also indicated the same trend for the experimental vortex mass.

Additional information on Bloch vortices can be obtained by irradiating the sample with a microwave signal. Steps occur in the I-V characteristics when the external frequency locks to the Bloch frequency. Surprisingly, the experiments show that the Bloch frequency depends on the vortex density. This dependence is not accounted for by the independent-vortex model presented above (see Eq. (83)) and suggests a collective oscillation of the 1D vortex chain (see next section). We will come back to this issue when discussing the formation of a Mott insulator in these quasi-1D arrays.

E. One-dimensional vortex localization

In Section II G , we already introduced quasi-one dimensional arrays as model systems for the study of interacting bosons in one dimensions. For an ideal periodic potential and in the absence of interactions between the particles, the solution of the Schrödinger equation consists of Bloch waves that extend throughout the whole chain.

In quasi-1D Josephson arrays, however, vortex localization can occur in several ways. We already discussed the existence of Bloch oscillations when an external force is exerted on a vortex. One can view this oscillatory motion in space as localization of individual bosons analogous to Wannier-Stark localization of electrons [282]: the extend of the wave function is decreased when the external force on the quantum particle is increased.

In the next two subsections, we treat two other cases where boson localization occurs. Commensurability effects [283] may lead to localization of vortices in quasi-1D arrays. The repelling interaction between vortices plays a crucial role in this so-called Mott-localization [40]. Another mechanism to localize Bloch waves is disorder and this phenomenon is known as Anderson localization [284]. Two important remarks should be made at this ponit. First, vortex localization, as discussed in the next subsection, has been studied by measuring the zero-bias resistance. In this case only a very small current is applied in contrast to the experiment showing the Bloch oscillations. Second, one should realize that in contrast to localization in electronic systems, vortex localization leads to a zero resistive state. In superconductors motion of vortices is the cause of dissipation. If they are localized, the sample is superconducting.

1. Mott insulator of vortices

More than ten years ago, localization of bosonic particles with a short-range repulsive interaction has been studied theoretically by Fisher *et al.* [40]. They found a Mott insulating phase for commensurate filling and a superfluid phase for incommensurate filling. Strong disorder destroys the Mott phase and there is the possibility to have a Bose glass (for theoretical studies of the phase-diagram of bosons on a chain see Refs. [118,119,285] and references therein).

Experimentally, Mott localization of vortices has been studied by van Oudenaarden *et al.* [263,265]. They explored the influence of the interaction strength, the bandwidth, the sample geometry and temperature on the stability of the Mott states. First, we will summarize the experimental results. Then, we discuss their experiment in the context of a recent theory of Bruder *et al.* [286].

The experiment consists in measuring the zero-bias resistance vs. magnetic field for quasi-one dimensional arrays of different lengths and E_J/E_C ratios. It is convenient to define a 1D frustration n, which is associated with magnetic field piercing through a cell of area W (in units of the lattice constant): $n = WB/\Phi_0 = Wf$. In Fig.39 the results are shown for arrays of three and seven cells wide, i.e., $W = 3$ and 7 respectively. The plot for the $W = 7$-sample is mirrored with respect to the x-axis for clarity. For both samples, clear dips occur for certain values of the 2D frustration index f, i.e., for certain values of the vortex density. When plotted vs. this 1D frustration index, the 1D nature of the sharp dips becomes visible. Dips are found at the same rational values of $n = 1/3, 1/2, 1, 2$.

More detailed measurements of the resistance dips show that they are not infinitely sharp. There is a certain window of n in which the resistance vanishes and the vortex chain is pinned. The interaction energy proportional to E_J (see below) dominates the bandwidth proportional to E_C in this regime. Beyond this window the resistance increases sharply, indicating that the vortex chain is depinned and that the bandwidth dominates the interaction energy. From this consideration, one expects the window to be larger for samples with a larger E_J/E_C ratios. In the experiment, this dependence has indeed been observed.

Around commensurate filling, the system is incompressible: small changes of the magnetic field (i.e. n) do not lead to a change in the number of vortices in the chain. This process costs a certain energy, called the Mott gap. By analyzing thermally activated transport in the Mott states, the value of this gap can be deduced from the experiments and values in the order of Kelvins are reported. The influence of the array length was also studied. No significant differences were observed in arrays with lengths larger than 200 cells. This observation demonstrates that edge effects do not play an important role and that the long arrays are indeed one-dimensional systems.

A quantitative theory of the commensurate-incommensurate transition of a vortex chain in quasi-one-dimensional Josephson arrays has been formulated by Bruder *at al.* [286]. They showed that the transition to the incommensurate state is due to the proliferation of soliton excitations of the vortex chain. Since the range of the interaction between the vortices is much longer than the inter-vortex distance, solitons consist of many vortices, and possess a large effective mass. The transfer of one flux quantum between the array edges is then due to soliton propagation through the sample. The number of solitons necessary to transfer one vortex is equal to the ratio of the periods of the vortex lattice and the junction array.

The analysis of Bruder *at al.* [286] focuses on determining the energy barrier E_R of the observed thermal activation in the resistance vs. temperature curves. Although this approach is of semi-classical nature, quantum effects are crucial in relating the parameters of the effective theory (expressed in terms of soliton excitations) to the microscopic couplings (E_C and E_J) of the Josephson array.

In the commensurate phase, there are two contributions to E_R. The first contribution comes from the activation energy of a soliton and the second term summarizes the boundary pinning energies. This boundary effect can be understood as follows: Because of commensurability, the process of vortex flow through the array can be viewed as the motion of a rigid vortex chain. Therefore, the vortex chain cannot adjust itself to the boundary pinning potential. The potentials produced by the two array ends both contribute to E_R and the relative phase of these two contributions depends on whether the total flux piercing the junction array equals an integer number of flux quanta or not. Consequently, the second

-boundary pinning- term to E_R oscillates with the magnetic flux piercing the array. In Fig.40 E_R is plotted for the case of small boundary pinning while the opposite situation is shown in Fig.41. The short period oscillations are determined by boundary-pinning term while the vanishing of E_R at the edge of Mott lobe is driven by the soliton energy.

In the incommensurate state, the vortex chain is compressible, and can adjust itself to the boundaries of the array. As a result, the main contribution to the activation energy is due to the boundary pinning potential and the elastic energy.

The comparison between theory and experiment is shown in Fig.42. The theoretical results lead to an estimate for the soliton energy much larger than the boundary pinning which is of the order of $\sim 0.5K$. The theoretical value of the activation energy

$$E_R \sim 8K$$

is in very good agreement with the experiments.

Two observations provide additional support for the theory of Bruder *et al.*. First, the regions of n corresponding to the Mott phase are extremely narrow suggesting, at least in the conventional non-interacting picture, a weak interaction between the particles. Consequently, within the Mott phase the activation energies for particle transport are expected to be small as well. However, the observed value of E_R is one order of magnitude larger than the energies E_C and E_J, which determine the single-vortex band spectrum. A second feature in favor is the strong oscillating behavior of the resistance (with a period proportional to the inverse length of the chain) outside the Mott region. These oscillations would not be expected in a model of almost-free quasi-particles within the delocalized phase.

2. Anderson localization of vortices

In 1958, Anderson [284] showed that disorder has a dramatic influence on transport properties. Disorder reduces the spatial extent of wave functions to such an extent that transport can completely be blocked. Three years later Mott and Twose [287] showed that 1D systems are particularly susceptible for disorder: even weak disorder leads to strong localization. Many studies on Anderson localization have been performed on 3D and 2D samples. One-dimensional model systems are harder to find. Josephson-junction arrays have the great advantage that disorder can be introduced in a controlled way. Experimentally, Anderson localization of vortices has been studied by the Delft group [264]. Their results will be outlined in this subsection.

In the experiment by the Delft group disorder has been introduced by constructing superlattice structures. The superlattice is formed by replacing all the junctions of a column by junctions that are twice as large. Consequently, these barrier junctions have a Josephson energy that is two times larger than that of the adjacent junctions. The barrier junctions yield a peak in the potential landscape for vortices traveling through the array. Numerical calculations show that this barrier is $1.7E_J$, which is about one order of magnitude larger than the energy barrier for cell-to-cell motion.

A perfect superlattice structure is made by introducing columns of barrier junctions on a distance of exactly 10 lattice cells. For an array of length 1000, this means that there are 100 columns that have been changed. Disorder is now introduced by changing the distance

between two barriers Samples with different amounts of disorder have been fabricated. In the least disordered samples (labeled with $\delta = 1$) the barriers were separated by 9, 10 or 11 lattice cells with equal probabilities. In other disordered samples (labeled with $\delta = 2$) barriers placed at distances 8, 9, 10, 11, or 12 lattice constants again with equal probability. All samples contained 100 barriers.

The vortex quantum properties are probed by measuring the zero-bias resistance as a function of temperature for the perfect periodic array as well as for the disordered arrays. Since the topic of interest is the study of quantum transport, the vortex density needs to have a non-commensurate value to avoid the Mott state as discussed in the previous subsection. The result for $n = 0.44$ is shown in Fig.43. At high temperatures all three arrays show the same behavior: transport is thermally activated with an energy barrier of $3E_J$, a factor of two larger than the expected value. When the temperature is lowered, however, a significant difference is observed between the periodic sample and the two disordered samples. For the perfect periodic sample a finite resistance is measured at the lowest temperatures. In this regime the resistance is independent on temperature indicating vortex transport by quantum tunneling. In contrast, the resistances of the disordered samples have dropped below the measuring accuracy of the set-up. Thus, in the perfect array vortices are mobile whereas they are localized in the disordered arrays.

The zero-bias resistance has been studied for several values of the vortex density. For $n < 0.3$, the zero-bias resistance is too small to be resolved for the periodic array. In the range $0.3 < n < 0.8$, the resistance of the periodic array is significantly larger than that of the disordered arrays and this is the region where vortex localization occurs. But for even larger vortex densities the behavior of all three arrays is almost the same showing a flattening of the resistance at the lowest temperatures. In all three arrays vortices are now mobile. At these high vortex densities the distance between them is small and their repulsive interaction can no longer be neglected. The experiment shows that in this case delocalization occurs.

Above we have discussed the experiment in terms of Anderson localization which strictly speaking occurs when the interaction between the bosons is very weak; i.e., when the bosons act as independent particles that are localized for arbitrarily weak disorder. In the experiment, vortex densities are large. Disorder now competes with the interaction strength. A sufficiently strong interaction can delocalize the particles, whereas strong disorder will localize them again in a Bose-glass phase. To distinguish between Anderson localization and localization in a Bose glass, more measurements are needed. Experiments should be performed on arrays with fixed disorder but different E_J to clarify the role of the interaction strength.

IV. FUTURE DIRECTIONS

In this last chapter of the review, we discuss some future directions for research on Josephson networks. Of course, additional information on the quantum nature of Josephson networks can be obtained by using new measuring techniques (e.g. the ac-measuring method that has successfully been applied to classical arrays) and better samples (e.g. arrays with a well-controlled environment). Here, we outline the concepts behind two experiments -persistent vortex currents and vortex quantum Hall effect- of which some theoretical

calculations are available. We summarize the main ideas as well as the experimental requirements/improvements for observation of these effects. Future lines of research may also involve the use of Josephson networks as model systems in unexplored areas of physics. Biophysics may be such a field and an interesting example in this respect is vortex transport in ratchet arrays. Undoubtedly, the most exciting new line of future research is quantum computation. In this paper, we do not have space to treat quantum computation with Josephson circuits in great depth. We therefore only present the concept and summarize the current status of art.

A. Persistent vortex currents

Persistent currents in rings made of normal metals are a manifestation of the Aharonov-Bohm effect for quantum coherent electrons in a multiply connected geometry. In the absence of any driving current, the flux through the ring induces the motion of charge carriers that can be detected at low temperatures [288]. Charge-flux duality indicates that in Josephson rings a persistent current of vortices may be expected generated by the charge induced on the inner island. A persistent vortex current leads to a persistent voltage across the ring and as such would be manifestation of the Aharonov-Casher effect discussed in Sec. III D. Although vortex interference in an open Josephson circuit has been reported by Elion *et al.* [266], there are no experiments reporting the existence of persistent vortex currents in Josephson Corbino circuits. The proposed setup to measure persistent vortex current is shown in Fig.44.

When the mean free vortex path is long enough, we can neglect the dissipation in the dynamics and the Hamiltonian of a vortex in a discrete Josephson ring (with N junctions) can be written as

$$H = \frac{1}{2M_v}\left(P - \frac{\Phi_0}{N}Q_x\right)^2 \tag{87}$$

where P is the vortex momentum and Q_x the charge on the inner island of the ring. The vortex dynamics is quantized and the set of discrete energy values is given by

$$E_\nu = \frac{(2e\nu - Q_x)^2}{2C_{eff}} \quad \text{with} \quad C_{eff} = \left(\frac{N}{\Phi_0}\right)^2 M_v \tag{88}$$

where ν is an integer and where C_{eff} agrees with the continuum result of Ref. [289] and with C_{kin} in Ref. [278]. Thus, a Josephson ring with a vortex trapped inside acts like a perfect capacitor. A similar situation arises in a single classical junction in the absence of screening. With exactly one vortex trapped, its critical current is zero. The difference lies in the value of the effective capacitance, which in quantum rings differs from the geometrical one. For example, for a ring consisting of a square 2D array $C_{eff} = (N^2/2)C$ and for a 1D ring with $\Lambda_J < N$, $C_{eff} = (2N/\pi^2\Lambda_J)NC$.

Although this change in capacitance can in principle be measured, quantum rings should exhibit a more interesting phenomenon: persistent vortex currents. This can easily been seen from the Hamiltonian of Eq.(87) since it has the same from as the Hamiltonian for electrons in a metal ring. Duality arguments then indicate the existence of a persistent voltage due

to the persistent motion [225,277,290] of a vortex induced by Q_x. The basic reasoning is as follows: With some disorder, small gaps open up in the energy spectrum of Eq.(88) and energy bands form. With no current applied, the charge Q_x dictates the quantum dynamics of the ring. It determines the vortex velocity and therefore the voltage across the ring because the vortex speed is proportional to $\partial E_n/\partial Q_x$. As a result, a persistent voltage appears across the ring which is periodic in Q_x with period $2e$.

Within the free-particle model, the maximum voltage can be estimated. The voltage V due to a circling vortex with velocity v is equal to $\Phi_0 v/N$. The velocity is equal to $(N/\Phi_0)\partial E_\nu/\partial Q_x$. Then for $\nu = 0$ and $Q_x = e$, the maximum voltage equals $e/C_{eff} = e/M_v\,(\Phi_0/N)^2$. For a ring consisting of a square 2D array $V_{max} = (2e/CN^2)$. With $N = 10$, $C = 1$ fF, $V_{max} \sim 3\ \mu$V.

In the picture presented above, the vortex is treated as a free, non-interacting particle. A detailed description of vortex dynamics, however, is only possible if one considers its dissipative environment. As discussed before, an important dephasing mechanism is the existence of linear spin-waves. This coupling leads to damping and hence to a finite phase-coherence length for vortices. This problem was studied in Ref. [291]. For the persistent voltage one obtains

$$\langle 2eV\rangle = \frac{4\pi}{\beta}\frac{\sum_{\nu=1}^{\infty} n\sin(2\pi\nu Q_x/2e)\exp(-S_\nu)}{1+2\sum_{\nu=1}^{\infty}\cos(2\pi\nu Q_x/2e)\exp(-S_\nu)} \tag{89}$$

where S_ν corresponds to the action in the sector of ν winding numbers. In the adiabatic mass approximation in the limits $E_J \gg E_C$ and $R_N \lesssim R_K$, the action reduces to that of a free particle with mass $M_v = \pi^2/4E_C$. The saddle point action is

$$S_\nu^0 = \frac{M_v}{2\beta}(\nu N)^2 \tag{90}$$

and the persistent voltage V is a sawtooth function of Q_x at zero temperature and a sine-like function at higher temperatures. It depends on the system size through the ratio of the radius N/π to the thermal wavelength of the vortex $\lambda_T = \sqrt{2\pi/M_v T} = \sqrt{8\beta E_C/\pi}$.

To go beyond the adiabatic mass approximation, the actions S_ν can be calculated with the full non-local kernel (see Eq. 71) that incorporates the effect of inelastic processes due to the interaction with spin-waves. An important consequence of the quantum corrections is that the vortex dephasing length

$$L_\varphi = \omega_p \xi/T \tag{91}$$

increasing with the ratio $E_C \sim E_J$ (ξ gets larger on approaching the S-I transition). For $E_C \sim E_J \sim 1K$, L_φ may be as large as 100 lattice constants at T= 10 mK, which is much larger than the thermal wavelength λ_T for the vortex in the adiabatic mass approximation. In the limit $\xi \ll N$ and $\omega_\nu \ll \omega_p$ the adiabatic result is recovered. If $\xi \sim 1$ a larger persistent voltage is found. If the ratio E_J/E_C is reduced, the coherence length ξ grows beyond the radius of the system, and the persistent voltage grows even more. As compared to the adiabatic mass limit, the persistent voltage including the vortex-spin-wave coupling is always larger. For E_J= E_C=1 K, T=10 mK and $N = 10$, a persistent voltage in the microvolt range is expected, which is observable.

Other interesting issues involve the effect of the underlying lattice and of disorder on the persistent voltage. They both induce backscattering and the opening of gaps in the band structure $E(Q_x)$. One expects Zener tunneling across the band gaps to occur if the voltage V_x is switched on fast, yielding a higher transient current that relaxes to the persistent current after some relaxation time.

Experimentally, fabrication of quantum rings is difficult, but does not seem to be impossible. First of all vortices should have long mean free paths. As we have seen, 2D arrays exhibit only a small window for which free propagation of vortices is possible. Purely 1D discrete Josephson rings with one vortex trapped [228] seem to be more promising in this respect since for $\Lambda_J > 1$ there is no energy barrier for vortex motion. Coupling to spin-waves can be small and long mean free vortex paths are expected [292]. Secondly, Josephson rings should be decoupled from their environment. This can be achieved by placing high-Ohmic resistors or alternatively arrays of junctions in the leads close by.

A third restriction comes from the charging energy. Calculations on the continuous Josephson system [293] show that the temperature has to be smaller than $e^2/(2\pi^2 C_{eff})$ in order to observe quantum vortex dynamics. Temperatures of the order of 100 mK therefore require C_{eff} to be 1 fF. This requirement indicates that aluminum junctions have to be smaller than 0.01 μm^2 and that the whole ring structure can not be made too large. The capacitances to ground would otherwise be too dominant. The fourth restriction comes from the shadow-evaporation method itself. Both the wire connecting the central island in the middle of the ring and the gate capacitor -preferable situated underneath or on top of the central island- have to be made in separate fabrication steps. Alignment and good electrical isolation between the different layers have to be established.

B. The Quantum Hall effect

Quantum electron transport in two-dimensional systems in the presence of an applied magnetic field is one of the most intensively investigated areas in condensed matter. When the filling factor (ratio between the electron density and the density of flux quanta) is of the order of one, the Quantum Hall effect (integer and fractional) occurs [294]. In the previous sections we showed that charges and vortices behave as quantum particles hopping coherently in the artificial two-dimensional space created by the Josephson array. The duality between charges and vortices can be shown also in the presence of external frustration; magnetic field for charges and offset charges for vortices. In a series of papers [295–297] it was suggested that a Quantum Hall effect could be observed in Josephson arrays both for charges and vortices. The three proposals address different regimes: Nazarov and Odintsov [295] describe the possibility of Hall states for Cooper pairs while the authors in Refs. [296,297] consider the Hall fluid of vortices.

In the limit $E_C >> E_J$ and in the case of very low density, charges behaves as a dilute Bose gas with strong repulsion. Under these conditions, analytic and numerical calculations [295] support the idea that in a magnetic field Cooper pairs form Laughlin-type incompressible states (a Cooper pair fluid): the charge density changes in a stepwise function by changing the external parameters. The incompressible states give rise to the quantization

of the Hall conductance

$$\sigma_{xy} = \frac{4e^2\nu}{h}$$

where the filling factor $\nu = q/f$ is given by the ratio between the charge density q and the magnetic frustration f. According to Odintsov and Nazarov two sets of Hall plateaus exist. One corresponds to the fractional quantum Hall effect with $\nu = 2m$ (m integer). The other corresponds to the integer quantum Hall effect with $\nu = l/2$ (l integer).

The opposite limit in which the Josephson energy dominates, has been considered in Refs. [296,297]. In this case vortices condense to form a quantum Hall fluid and the transverse conductivity is now given by:

$$\sigma_{xy} = 2m\frac{4e^2}{h} \quad .$$

Despite the similarities highlighted here, there are important differences as compared to the "electronic" case. Both charges and vortices are bosons, moreover they are interacting particles. Interactions modify the results. For instance, in the vortex case the logarithmic interaction changes the longitudinal response [297] as well.

Up to now there is no experimental evidence for the quantum Hall effect in Josephson arrays. For the Cooper-pair fluid, the random offset charges form a serious obstacle for observation of the Quantum Hall states. For the vortex fluid the situation is less clear. Additional theoretical work is required to locate the region in parameter space where the Hall fluid is the ground state (as opposed to the Abrikosov lattice for example). Effects related to disorder, quantum correction of the mass, and dissipation should all be taken into account.

C. Quantum Computation with Josephson junctions

Quantum Computation (QC) has recently excited many scientists from various different areas of physics, mathematics and computer science. In contrast to its classical counterpart, quantum information processing is based on the controlled unitary evolution of quantum mechanical systems. The great interest in this field is certainly related to the fact that some problems which are intractable with classical algorithms can be solved much faster with QC. Factorization of large numbers as proposed by Shor is probably the best known example in this respect. This section briefly reviews the recent work in this field using Josephson nano-circuits. For excellent reviews devoted to QC we refer to Refs. [298,299]. Furthermore, many elementary books on quantum mechanics treat the physics of two-level systems. A review devoted to the implementation of quantum computation by means of Josephson nano-circuits just appeared [300].

The elementary unit of any quantum information process is the *qubit*. The two values of the classical bit are replaced by the ground state ($|0>$) and excited ($|1>$) state of a two-level system. (Note that it common to adopt the spin-1/2 language as we will do here.) Already at this stage a fundamental difference between classical and quantum bits emerges. While information is stored either in 0 or in 1 in a classical bit, any state $|\psi(t)> = a(t)|0> + b(t)|1>$ can be used as a qubit.

Manipulations of spin systems have been widely studied and nowadays NMR physicists can prepare the spin system in any state and let it evolve to any other state. Controlled

evolution between the two degenerate states $|0>$ and $|1>$ is obtained by applying resonant microwaves to the system but state control can also be achieved with a fast DC pulse of high amplitude. By choosing the appropriate pulse widths, the NOT operation can be established

$$\begin{aligned} |0> &\longrightarrow |1> \\ |1> &\longrightarrow |0> \end{aligned} \tag{92}$$

or the Hadamard transformation

$$\begin{aligned} |0> &\longrightarrow \frac{1}{\sqrt{2}}(|0> + |1>) \\ |1> &\longrightarrow \frac{1}{\sqrt{2}}(|0> - |1>) \; . \end{aligned} \tag{93}$$

These unitary operations alone do not make a quantum computer yet. Together with one-bit operations it is of fundamental importance to perform two-bit quantum operations; i.e., to control the unitary evolution of entangled states. Thus, a universal quantum computer needs both one and two-qubit gates (it has been shown that most of two-qubit gates are universal [301]). One example of a two-qubit gate is the Control-NOT operation:

$$\begin{aligned} |00> &\longrightarrow |00> \\ |01> &\longrightarrow |01> \\ |10> &\longrightarrow |11> \\ |11> &\longrightarrow |10> \end{aligned} \tag{94}$$

The unitary single-bit operations and this Control-NOT operation are sufficient for performing all tasks of a quantum computer. Therefore, quantum computers can be viewed as programmable quantum interferometers. Initially prepared in a superposition of all the possible input states, the computation evolves in parallel along all its possible paths, which interfere constructively towards the desired output state. It is this intrinsic parallelism in the evolution of quantum systems that allows for exponentially more efficient ways of performing computation.

It is of crucial importance that qubits are protected from the environment, i.e., from any source that could cause decoherence [302]. This is a very difficult task because at the same time one also has to control the evolution of the qubits, which inevitably means that the qubit is coupled to the environment. In quantum optics experiments, single atoms are manipulated which are almost decoupled from the outside world. Large-scale integration (needed to make a quantum computer useful) seems to be on the other hand impossible. Qubits made out of solid-state devices (spins in quantum dots or superconducting nano-devices), may offer a great advantage in this respect because fabrication techniques allow for scalability to a large number of coupled qubits.

At present different proposals have been put forward to use superconducting nano-circuits [303–307] for the implementation of quantum algorithms. Depending on the operating regime, they are commonly referred to as charge [303,304,307,308] and flux [305,306] qubits. We briefly discuss both approaches and summarize the experimental advances made so far.

Charge qubits [303,304] - In this case the qubit is realized by the two nearly degenerate charge states of a single electron box as shown in Fig.45. They represent the states $|0\rangle$, $|1\rangle$ of the qubit. In the computational Hilbert space the ideal evolution of the system is governed by the Hamiltonian

$$H = -\Delta E_{\mathrm{ch},i}((|0><0| - |1><1|) - \frac{E_J}{2}(|0><1| + |1><0|) \tag{95}$$

where $\Delta E_{\mathrm{ch},i} = E_{\mathrm{ch}}(n_x - 1/2)$. Any one bit operation can be realized by varying the external charge n_x and, in the proposal of Ref. [303] by varying the Josephson coupling as well. Modulation of E_J is achieved by placing the Cooper-pair box in SQUID geometry. The advantage of this choice is that during idle times the Hamiltonian can be "switched off" completely eliminating any trivial phase accumulation which should be subtracted for computational purposes.

As discussed before, a quantum computer can be realized once two bit gates are implemented. The Karlsruhe group has proposed an inductive coupling between qubits which lead to a coupling of the type

$$H_C = -E_L \sigma_y^{(1)} \sigma_y^{(2)} \quad . \tag{96}$$

This type of coupling is very close in spirit to the coupling used in the ion-trap implementation of QC. The main advantage of this choice is that qubits are coupled via an infinite range coupling and that the two bits can easily be isolated. A different scheme has been proposed in Ref. [304]. They emphasize the adiabatic aspect of conditional dynamics and suggest to use capacitive coupling between gates as to reduce unwanted transitions to higher charge states. The coupling reads $H_C = -E_C \sigma_z^{(1)} \sigma_z^{(2)}$ and the qubit is now defined as a finite one-dimensional array of junctions. By means of gate voltages applied at different places in the array the bit-bit coupling can be modulated in time and a control-NOT can be realized.

The experiments on the superposition of charge states in Josephson junctions [309,310] and the recent achievements in controlling the coherent evolution of quantum states in a Cooper pair box [311] render superconducting nanocircuits interesting candidates to implement solid state quantum computers. The experiment by Nakamura *et al.* [311] goes as follows. Initially, the system is prepared in the ground state. Appropriate voltage pulses bring the system in resonance so that the two charge states are in a coherent superposition $a(t)|0> + b(t)|1>$. The final state is measured by detecting a tunneling current through an additional probe-junction. For example, zero tunneling current implies that the system ended up in the $|0>$ state, whereas a maximum current indicates that the final state corresponds to the excited one. In the experiment the tunneling current shows an oscillating behavior as a function of pulse length, thereby demonstrating the evolution of a coherent quantum state in the time domain.

Nakamura *et al.* also estimate the dephasing time and report it to be of the order of few nanoseconds. The probe junction and 1/f noise presumably due the motion to trapped charges are the main source of decoherence. In their absence, the main dephasing mechanism is thought to be spontaneous photon emission to the electromagnetic environment. Decoherence times of the order of 1 μs should then be possible.

Phase qubits [305,306] - A qubit can also be realized with superconducting nano-circuits in the opposite limit $E_J \gg E_C$. An rf-SQUID (a superconducting loop interrupted by a

Josephson junction) provides the prototype of such a device. The Hamiltonian of this system reads

$$\mathcal{H} = -E_J \cos\left(2\pi\frac{\Phi}{\Phi_0}\right) + \frac{(\Phi-\Phi_x)^2}{2L} + \frac{Q^2}{2C}\,. \tag{97}$$

Here, L is the self-inductance of the loop and the phase difference across the junction ($2\pi\Phi/\Phi_0$) is related the flux Φ in the loop. The externally applied flux is denoted by Φ_x. The charge Q is canonically conjugated to the flux Φ. In the limit in which the self-inductance is large, the two first terms in the Hamiltonian form a double-well potential near $\Phi = \Phi_0/2$. Also in this case the Hamiltonian can be reduced to that of a two-state system. The term proportional to σ_z measure the asymmetry of the double well potential and the off-diagonal matrix elements depend on the tunneling amplitude between the wells. By controlling the applied magnetic field, all elementary unitary operations can be performed.

In order to fulfill various operational requirements more refined designs should be used. In the proposal of Mooij *et al.* [305], qubits are formed by three junctions (see Fig. 46). Flux qubits are coupled by means of flux transformers which provide inductive coupling between them. Any loop of one qubit can be coupled to any loop of the other, but to turn off this coupling, one would need to have an ideal switch in the flux transformer. This switch is to be controlled by high-frequency pulses and the related external circuit can lead to decoherence effects.

At present, both the Stony Brook group (Friedman *et al.* [312]) and the Delft group (Van der Wal *et al.* [313]) have demonstrated superposition of two magnetic flux states in superconducting loops. One state corresponds to the magnetic moment of μA-currents flowing clockwise whereas the other corresponds the same moment but of opposite sign due to the current flowing anti-clockwise. Coherent quantum oscillations have not yet been detected. To probe the time evolution, pulsed microwaves instead of continuous ones have to be applied. Observation of such oscillations would imply the demonstration of macroscopic quantum coherence (MQC). It is called macroscopic because the currents are built of billions of electrons coherently circulating within the superconducting ring.

There are two main differences between the approaches of the two groups. The Stony Brook group uses the excited states of an RF SQUID. The Delft circuit consists of a three-junction system and the continuous microwaves induce transitions between the ground state and the first excited state only. The three-junction geometry has the advantage that it can be made much smaller so that it is less sensitive to noise introduced by inductive coupling to the environment. Nevertheless, recent insights indicate that in all designs put forward so far the measuring equipment destroys quantum coherence. The meter is believed to be main obstacle to study the 'intrinsic' decoherence times. Future work must evaluate the role of the measuring equipment and new measuring schemes should be developed in order to study MQC in Josephson loops.

ACKNOWLEDGMENTS

Special thanks go to J.E. Mooij and G. Schön for many years of fruitful collaboration, guidance and for sharing their insight and knowledge with us.
With C. Bruder, G. Falci, B. Geerligs, G. Giaquinta, T.P. Orlando, A. van Otterlo we had a

long-standing fruitful and pleasant collaboration, we would like to thank them for this. We also thank C. Bruder for a careful reading of the manuscript.
We acknowledge L. Amico, R. Baltin, P.A. Bobbert, Ya. Blanter, A. Kampf, W. Elion, A. Tagliacozzo, K.-H. Wagenblast, G. T. Zaikin, D. Zappalà, and G.T. Zimanyi for valuable collaboration on these topics.
Finally we thank O. Buisson, J. Clarke, P. Delsing, A. Fubini, L. Glazman, D.B. Haviland, P. Martinoli, Yu. Nazarov, A. Odintsov, A. van Oudenaarden, B. Pannetier, M. Rasetti, P. Sodano, L. Sohn, M. Tinkham, V. Tognetti for many useful conversations.
R.F is supported by the European Community under TMR and IST programmes and by INFM-PRA-SSQI, H.v.d.Z. is supported by the Dutch Royal Academy of Arts and Sciences (KNAW).

APPENDIX A: ARRAY FABRICATION AND EXPERIMENTAL DETAILS

There are two types of junctions arrays: *proximity* coupled arrays and arrays made of Josephson *tunnel* junctions. The proximity coupled arrays consist of superconducting islands (Nb or Pb) on top of a normal metal film (Cu) and are solely used for the study of classical phenomena. The main reason for this is the low (less than 1 Ohm) normal-state resistance of the junctions.

At present there are two technologies to fabricate arrays with Josephson *tunnel* junctions. Commercial niobium junctions are fabricated using a trilayer with aluminum oxide as insulating barrier. Reliable niobium junctions, however, are too large to observe the quantum effects discussed in this review. Quantum arrays are built up of all aluminum, tunnel junctions. These Josephson junctions are fabricated with a shadow-evaporation technique [314]. We will now outline the most recent fabrication technique as used in the Delft group.

Samples are fabricated on silicon substrates with an insulating SiO_2 top layer. In the first step two resist layers are spun on the substrate. The lower layer is a solution of PMMA/MAA copolymer in acetic acid and the upper layer is a solution of PMMA in chlorobenzene. The resist sandwich is baked at 180 °C for one hour. Then the sample mask is written by high-resolution electron-beam lithography at 100 kV. After writing, the exposed resist is developed in a 1:3 mixture of MIBK and 2-propanol for one minute. The solubility of the lower resist is larger than the upper layer, which leads to an undercut in the lower resist layer. This undercut is necessary for the formation of free-hanging bridges below which the junctions are formed in the shadow evaporation technique.

After mask definition, a 24 nm thick aluminum layer is evaporated under a given angle. Then the aluminum layer is exposed to pure oxygen at a controlled pressure. By changing the pressure the thickness of the aluminum oxide barrier is varied. In the second evaporation step (the sample is not taken out of the vacuum) a 40 nm thick aluminum layer is evaporated under the opposite angle. After this step, the tunnel junction is formed. The remaining resist layers with the unwanted aluminum on top are removed by rinsing the sample in acetone.

We end this appendix with some remarks on the measuring set-up. Arrays are measured in a dilution refrigerator inside μ-metal and lead magnetic shields at temperatures down to 10 mK. To protect the arrays from high energy photons generated by room-temperature noise and radiation, extensive filtering and placing the arrays in a closed copper box are minimum requirements. Therefore, a typical set-up for the measurements of quantum arrays has the

following characteristics. At the entrance of the cryostat, electrical leads are filtered with radio-frequency interference (RFI) feedthrough filters. Arrays are placed inside a closed, grounded copper box (microwave-tight). All leads leaving this box are filtered with RC filters for low-frequency filtering ($R = 1$ kΩ and $C = 470$ pF) and with microwave filters. A microwave filter consists of a coiled manganin wire (length ~ 5 m), put inside a grounded copper tube that is filled with copper powder (grains < 30 μm). The resistance of the wire in combination with the capacitance to ground via the copper grains provide an attenuation over 150 dB at frequencies higher than 1 MHz. The copper box with the RC and microwave filters is situated in the inner vacuum chamber and is mounted on the mixing chamber in good thermal contact.

APPENDIX B: TRIANGULAR ARRAYS AND GEOMETRICAL FACTORS

In comparing properties of square and triangular arrays some care is necessary. The energy required to store an additional electron on an island is $e^2/2C_\Sigma$, where C_Σ is the sum of the capacitances to other islands and to ground. As in triangular arrays all islands are coupled with $z = 6$ instead of $z = 4$ junctions, the required energy is 2/3 times smaller than that of an island in a square lattice. Similarly, the freedom of the phase on a particular island is determined by the Josephson coupling energy of all junctions connected to the island and therefore it seems reasonable to assume that in a triangular array the effective Josephson coupling energy is 3/2 times that of a square array. Summarizing, we come to the conclusion that the effective E_C/E_J-ratio for a triangular array is a factor 4/9 lower than that of a square array.

APPENDIX C: PHASE CORRELATOR

In this Appendix we show how to evaluate the phase-phase correlator g_{ij} introduced in Section II B (see also Ref. [121]). The starting point is:

$$\begin{aligned} g_{i0}(\tau) &= \langle \exp[\phi_i(\tau) - \phi_0(0)\rangle_{ch} \\ &= \frac{1}{Z_{ch}} \sum_{\{n_j\}} \prod_j \int d\phi_{j0} \int_{\phi_{j0}}^{\phi_{j0}+2\pi n_j} \mathcal{D}\phi_j e^{-S_{ch}} e^{2\pi i \sum_j q_{xj} n_j + i[\phi_i(\tau) - \phi_0(0)]} \end{aligned} \tag{C1}$$

By making use of the parametrization

$$\phi_i(\tau) = \phi_{i0} + 2\pi i n_i \frac{\tau}{\beta} + \theta_i(\tau)$$

it is possible to verify that all the off-diagonal elements of the correlation function, viz. $g_{i0}(\tau)$ for $i \neq 0$ vanish because of the integrations over ϕ_{j0}. The reason is that S_{ch} does not depend on the phase $\phi_0(\tau)$ itself but only on its time derivative. It is therefore sufficient to calculate the on-site correlation function at site

$$g(\tau) \equiv g_{00}(\tau) = \frac{1}{Z_{ch}} \sum_{\{n_j\}} \exp\Big(2\pi i \sum_j q_{xj} n_j - T \sum_{ij} \frac{4\pi^2}{8e^2} n_i C_{ij} n_j\Big) \exp(-2\pi i T n_0 \tau)\, g_c(\tau) \tag{C2}$$

where $g_c(\tau)$, the correlation function for the case of continuous charges, results from the remaining integral over $\theta(\tau)$. It is given by

$$g_c(\tau) = \exp\,[\,-2e^2 C_{00}^{-1}\tau(1-\tau T)]\;. \tag{C3}$$

By using the Poisson resummation formula

$$\sum_{\{n_i\}} \exp(-\sum_{ij} n_i A_{ij} n_j + 2\sum_i z_i n_i) = \sqrt{\frac{\pi^N}{detA}} \sum_{\{q_i\}} \exp[-\sum_{ij} (\pi q_i + z_i) A_{ij}^{-1} (\pi q_j + z_j)] \tag{C4}$$

and performing the Fourier transform

$$g(\omega_\nu) = \int_0^\beta d\tau \exp(i\omega_\nu \tau) g(\tau)$$

one obtains

$$g(\omega_\nu) = \frac{1}{Z_{ch}} \sum_{\{q_i\}} e^{-\frac{2e^2}{T}\sum_{ij}(q_i - q_x)C_{ij}^{-1}(q_j - q_x)} \frac{4e^2 C_{00}^{-1}}{[2e^2 C_{00}^{-1}]^2 - [4e^2 \sum_j C_{0j}^{-1}(q_j - q_x) - i\omega_\nu]^2}\;. \tag{C5}$$

The expressions for the coefficients ϵ, γ, ζ and λ in the coarse-graining approach follow from an expansion at small frequencies of Eq.(C5).

APPENDIX D: DERIVATION OF THE COUPLED COULOMB GAS ACTION

In this Appendix we briefly discuss the steps leading to Eq.(23). following the calculation in Ref. [91,92]. First a path integral representation is introduced for the island charges. In terms of phase trajectories $\phi_i(\tau)$ and charges $q_i(\tau) = Q_i(\tau)/2e$ the partition function takes the form

$$Z = \prod_j \int dq_{j0} \int Dq_j \prod_i \sum_{\{m_i\}} \int D\phi_i(\tau) \exp(-S\{\phi, q\}), \tag{D1}$$

where the phases obey the boundary conditions $\phi_j(0) = \phi_j(\beta) + 2\pi n_j$, while the charge paths are periodic, $q_j(0) = q_j(\beta) = q_{j0}$. The effective action in the mixed representation is

$$S\{\phi, q\} = \int_0^\beta d\tau \left\{ 2e^2 \sum_{i,j} q_i(\tau) C_{ij}^{-1} q_j(\tau) + i\sum_i q_i(\tau)\dot{\phi}_i(\tau) - E_{\rm J} \sum_{\langle ij\rangle} \cos(\phi_i - \phi_j) \right\}. \tag{D2}$$

Summation over winding numbers $\{n_i\}$ fixes the charges q_i to be integer-valued. Starting from the partition function (D1), we first introduce the vortex degrees of freedom. This can be done by means of the Villain transformation [86] (see also [87]); the time-dependent quantum problem requires some additional steps [91,92]. We introduce the lattice with spacing ϵ in time direction; this spacing is of order of inverse Josephson frequency: $\epsilon \sim (8E_{\rm J}E_{\rm C})^{1/2}$. In the Villain approximation one replaces

$$\exp\Big\{-\epsilon E_J \sum_{\langle ij\rangle,\tau} [1 - \cos(\phi_{i,\tau} - \phi_{j,\tau})]\Big\} \to \sum_{\{\mathbf{m}_{i\tau}\}} \exp\Big\{-\frac{\epsilon E_{\rm J} F(\epsilon E_J)}{2} \sum_{i,\tau} |\nabla\phi_{i\tau} - 2\pi \mathbf{m}_{i\tau}|^2\Big\}. \tag{D3}$$

Here, we have introduced a two-dimensional vector field $\mathbf{m}_{\mathbf{i}\tau}$, defined on the dual lattice (alternatively, it can be considered as a scalar field defined on bonds). The function

$$F(x) = \frac{1}{2x\ln(J_0(x)/J_1(x))} \to \frac{1}{2x\ln(4/x)}, \quad x \ll 1,$$

has been introduced to "correct" the Villain transformation for small E_J. As we see, its entire effect is to renormalize (increase) the Josephson coupling $E_J \to E_J F(\epsilon E_J)$, but it does not affect the physics. In the following we will use only the renormalized constant.

The rhs. of Eq.(D3) can be rewritten as

$$\sum_{\{\mathbf{J}_{i\tau}\}} \exp\Big\{ -\frac{1}{2\epsilon E_J}\sum_{i,\tau} |\mathbf{J}_{i\tau}|^2 - i\mathbf{J}_{\mathbf{i}\tau}\nabla\phi_{i\tau}\Big\}$$

Now the Gaussian integration over the phases can be easily performed, yielding

$$Z = \sum_{q_{i\tau}}\sum_{\mathbf{J}_{i\tau}} \exp\Big\{ -2e^2\epsilon\sum_{i,j,\tau} q_{i\tau}C^{-1}_{ij}q_{j\tau} - \frac{1}{2\epsilon E_J}\sum_{i,\tau}|\mathbf{J}_{i\tau}|^2\Big\}, \tag{D4}$$

and the summation is constrained by the continuity equation,

$$\nabla\cdot\mathbf{J}_{i\tau} - \dot{q}_{i\tau} = 0\ .$$

The time derivative stands for a discrete derivative $\dot{f}(\tau) = \epsilon_\mu^{-1}[f(\tau+\epsilon_\mu) - f(\tau)]$. The constraint is satisfied by the parameterization [88]

$$J^{(\mu)}_{i\tau} = n^{(\mu)}(\mathbf{n}\nabla)^{-1}\dot{q}_{i\tau} + \epsilon^{(\mu\nu)}\nabla_\nu A_{i\tau}.$$

Here the operator $(\mathbf{n}\nabla)^{-1}$ is the line integral on the lattice (in Fourier space it has the form $i(k_x+k_y)^{-1}$), $\epsilon^{(\mu\nu)}$ is the antisymmetric tensor, while $A_{i\tau}$ is an unconstrained integer-valued scalar field. It is important to mention that the continuity equation can be solved in different ways which can be mapped onto each other by gauge transformations (see Ref. [90]).

With the use of the Poisson resummation (which requires introducing a new integer scalar field $v_{i\tau}$) the partition function can be rewritten as

$$Z = \sum_{[q_{i\tau},v_{i\tau}]} \exp -S\{q,v\}\ .$$

The effective action for the integer charges q_i and vorticities v_i is

$$\begin{aligned} S[q,v] = {} & 2e^2\epsilon\sum_{ij\tau} q_{i\tau}C^{-1}_{ij}q_{j\tau} - \frac{1}{2\epsilon E_{\rm J}}\sum_{i\tau}\Big[n^{(\mu)}(\mathbf{n}\nabla)^{-1}\dot{q}_{i\tau}\Big]^2 \\ & - \frac{\epsilon E_{\rm J}}{4\pi}\sum_{ij\tau}\Big[2\pi v_{i\tau} - \frac{i}{\epsilon E_{\rm J}}\epsilon^{(\mu\nu)}\nabla_\nu n^{(\mu)}(\mathbf{n}\nabla)^{-1}\dot{q}_{i\tau}\Big]G_{ij}\Big[2\pi v_{i\tau} - \frac{i}{\epsilon E_{\rm J}}\epsilon^{(\mu\nu)}\nabla_\nu n^{(\mu)}(\mathbf{n}\nabla)^{-1}\dot{q}_{j\tau}\Big] \end{aligned}$$

The kernel G_{ij} is the lattice Green's function, i.e., the Fourier transform of k^{-2}. Finally, after some algebra [92] one arrives to the effective action of Eq.(23), which we rewrote, for simplicity, in the continuous notations.

APPENDIX E: EFFECTIVE SINGLE VORTEX ACTION

It is possible to derive from the coupled Coulomb gas action an effective action for a single vortex of vorticity $v = \pm 1$. The single vortex effective action includes the effect of the interaction with fluctuating charges and the other vortices which are present in the system due to quantum fluctuations. The desidered effective action is formally obtained by performing the sum in the partition function over all charge and vortex configurations excluding the vortex whose dynamics is to be studied. We introduce the vortex trajectory

$$v_{i,\tau} = v\delta(\mathbf{r}_i - \mathbf{r}(\tau)) \quad .$$

The single vortex effective action can then be written as

$$S_{eff} = -\ln \Big\langle \epsilon 2\pi E_J v \sum_{ij,\tau} v_{i,\tau} G_{ij} \delta(\mathbf{r}_j - \mathbf{r}(\tau)) + \\ + iv \sum_{ij,\tau} \dot{q}_{i,\tau} \Theta_{ij} \delta(\mathbf{r}_j - \mathbf{r}(\tau)) + iv\epsilon \sum_{ij,\tau} \mathbf{I}_{i,\tau} \cdot \nabla \Theta_{ij} \delta(\mathbf{r}_j - \mathbf{r}(\tau)) \Big\rangle \ , \tag{E1}$$

where the average is to be taken with the full coupled Coulomb gas action. The first term describes the static interaction with other vortices, whereas the second describes the dynamical interaction with charges. This expression, although exact, cannot be evaluated explicitly because of the nonlinearity of the action. To proceed we expand the dynamical part of the average in Eq.(E1) in cumulants up to second order in the vortex velocity $\dot{r}(\tau)$. For a uniform external current distribution the result is

$$S_{eff} = \frac{1}{2} \sum_{\tau\tau'} \dot{\mathbf{r}}^a(\tau) \mathcal{M}_{ab}(\mathbf{r}(\tau) - \mathbf{r}(\tau'), \tau - \tau') \dot{\mathbf{r}}^b(\tau') + 2\pi i v \epsilon \sum_{\tau} \epsilon_{ab} I^a_\tau \mathbf{r}^b(\tau) \ ,$$

$$\mathcal{M}_{ab} = \sum_{jk} \nabla_a \Theta(\mathbf{r}(\tau) - \mathbf{r}_j) \langle q_{j\tau} q_{k\tau'} \rangle \nabla_b \Theta(\mathbf{r}_k - \mathbf{r}(\tau')) \ , \tag{E2}$$

where $a, b = x, y$ and ϵ_{ab} is the anti-symmetric tensor [315].

APPENDIX F: LIST OF SYMBOLS

Josephson Energy	E_J
Junction capacitance	C
Ground capacitance	C_0
Capacitance matrix	C_{ij}
Charging energy (junction)	$E_C = e^2/(2C)$
Charging energy (ground)	$E_0 = e^2 C_{00}^{-1}/2$
Index labels for the islands in the array	i, j
Superconducting order parameter	$\Delta e^{i\phi}$
Charge on the island	Q
External charge	Q_x
Vector potential	$A_{ij} = \int_i^j \mathbf{A} \cdot d\mathbf{l}$
Flux quantum	$\Phi_0 = h/2e$
Magnetic frustration per plaquette	f
External current	I
Junction critical current	I_c
Quantum of resistance	$R_Q = h/(4e^2)$
Dissipation strength	α
Josephson plasma frequency	$\omega_p = \sqrt{8E_J E_C}$
BCS transition temperature	T_c
Vortex unbinding transition	T_J
Charge unbinding transition	T_{ch}
Universal conductance at the S-I transition	σ^*
Vortex mass	M_v
McCumber parameter	β_c
Josephson Junctionn Array	JJA
Superconductor - Insulator	S-I
Berezinskii - Kosterlitz - Thouless	BKT
Aharonov - Bohm	AB
Aharonov - Casher	AC
Bose - Hubbard	BH
Quantum Phase Model	QPM

REFERENCES

[1] R.F. Voss and R.A. Webb, Phys. Rev. B **25**, 3446 (1982); R.A. Webb, R.F. Voss, G. Grinstein and P.M. Horn, Phys. Rev. Lett. **51**, 690 (1983).

[2] *Percolation, Localization, and Superconductivity*, M. Goldman and S.A. Wolf Eds., NATO ASI **108** (1986).

[3] *Coherence in Superconducting Networks*, J.E Mooij and G. Schön Eds., Physica **B 152** pp 1-302 (1988).

[4] *Josephson Junction Arrays*, H.A. Cerdeira and S.R. Shenoy Eds., Physica **B 222**, pp 253-406 (1996).

[5] *Macroscopic Quantum Phenomena and Coherence in Superconducting Networks*, C. Giovanella and M. Tinkham Eds., (World Scientific, Singapore, 1995).

[6] E. Simanek, *Inhomogeneous Superconductors, Granular and Quantum Effects*, (Oxford University Press, Oxford, 1994).

[7] V.L. Berezinskii, Zh. Eksp. Teor. Fiz. **59**, 907 (1970) [Sov. Phys. JETP **32**, 493 (1971)].

[8] J.M. Kosterlitz and D.J. Thouless, J. Phys. C **6**, 1181 (1973).

[9] J. Resnick, J. Garland, J. Boyd, S. Shoemaker, and R. Newrock, Phys. Rev. Lett. **47**, 1542 (1981); P. Martinoli, P. Lerch, C. Leemann, and H. Beck, J. Appl. Phys. **26**, 1999 (1987).

[10] G. Schön and A.D. Zaikin, Phys. Rep. **198**, 237 (1990).

[11] D.V. Averin and K.K. Likharev, *Mesoscopic Phenomena in Solids*, B.L. Altshuler, P.A. Lee, and R.A. Webb Eds., (North-Holland, Amsterdam, 1991).

[12] S.L. Sondhi, S.M. Girvin, J.P. Carini, D. Shahar, Rev. Mod. Phys. **69**, 315 (1997).

[13] S. Sachdev, *Quantum Phase Transition*, (Cambridge University Press, Cambridge, 1999).

[14] A. Goldman and N. Markovic, Physics Today November issue p. 39 (1998).

[15] U. Weiss *Quantum Dissipative Systems*, (World Scientific, Singapore, 1999).

[16] P.W. Anderson, *Lectures on the Many Body Problem*, Caianiello Ed., (Academic Press, New York, 1964), p.113.

[17] W.J. Elion, M. Matters, U. Geigenmüller, and J.E. Mooij, Nature **371**, 594 (1994).

[18] M. Matters, W.J. Elion, and J.E. Mooij, Phys. Rev. Lett. **75**, 721 (1995).

[19] M. Tinkham, *Introduction to Superconductivity*, (McGraw-Hill, New York, 1996).

[20] A. Barone and G. Paterno, *Physics and Applications of the Josephson Effect*, (J. Wiley, New York, 1982).

[21] C.W.J. Beenakker and H. van Houten, Solid State Physics **44**, 1 (1991).

[22] Y. Imry, *Introduction to Mesoscopic Physics*, (Oxford University Press, Oxford, 1997).

[23] *Mesoscopic Superconductivity*, F.W.J. Hekking, G. Schön, and D.V. Averin Eds., Physica **B 203** pp 201-537 (1994).

[24] *Mesoscopic Electron Transport*, L.P. Kouwenhoven, L.L. Sohn and G. Schön Eds., NATO ASI series E, Vol. 345, Kluver (1997)

[25] S. Doniach in *Percolation, Localization and Superconductivity*, A.M. Goldman and S.A. Wolf Eds. (Plenum Press, New York, 1983).

[26] J.E. Mooij and G. Schön in *Single Charge Tunneling* H. Grabert and M.H. Devoret Eds., NATO ASI series Vol.294 (Plenum, NY 1992), p. 275.

[27] S. Katsumoto, J. Low. Temp. Phys. **98**, 287 (1995).

[28] V. Ambegaokar and A. Baratoff, Phys. Rev. Lett. **10**, 486 (1963); **11**, 104(E) (1963).

[29] For small junctions with low R_N, the oxide barrier is of the order of one atomic layer. Such thin layers may produce leaky junctions. We find that for our 1 fF junctions, this lower limit is about 1 kΩ. Thus, our aluminum tunnel junctions may become leaky when $R_N C < 10^{-12}$ s. For very small junctions with $C < 0.1$ fF, this criterion indicates that $R_N > R_Q$ ($= h/4e^2 = 6.45$ kΩ).
[30] The local rule instead of the global rule [10] to describe the coupling of tunneling processes to the environment seems to be more appropriate because the voltage offset is measured at high-bias currents.
[31] J.G. Lu, J. M. Hergenrother, and M. Tinkham, Phys. Rev. B **57**, 4591 (1998).
[32] C_0 can be increased considerably when placing the array on a conducting ground plane as done by A.J. Rimberg et *al*, Phys. Rev. Lett. **78**, 2632 (1997).
[33] J. D. Jackson, *Classical Electrodynamics*, (John Wiley & Sons, New York 1962).
[34] Quasi-particles may be generated by the environment (e.g. by photons). In a single small junction, the high-frequency coupling to the environment determines the effective damping, yielding an effective impedance of the order of 100 Ω (G. Ingold and Yu. V. Nazarov in *Single Charge tunneling* H. Grabert and M.H. Devoret Eds., NATO ASI series vol.294 (Plenum,NY 1992)). This impedance can be increased, i.e., a single junction can be decoupled from its environment by placing high-ohmic resistors or arrays of small junctions in the leads close to the junction. From the latter we expect that junctions inside a 2D array are decoupled from the leads.
[35] In classical arrays the scale of damping in junctions is commonly defined through the McCumber parameter $\beta_c(T) = 2\pi I_c(T) C R_e^2/\Phi_0$, where R_e is the effective damping resistance for each junction.
[36] A.O. Caldeira and A.J. Leggett, Phys. Rev. Lett. **46**, 211 (1981).
[37] A.O. Caldeira and A.J. Leggett, Ann. Phys. (N.Y.) **149**, 347 (1983).
[38] V. Ambegaokar, U. Eckern, and G. Schön, Phys. Rev. Lett. **48**, 1745 (1982).
[39] Recently Beloborodov *et al.* considered normal arrays and found a new effective action that in the low temperature limit yields the dynamically screened Coulomb interaction of a normal metal, whereas at high temperatures recovers the standard quantum dissipative action; I.S. Beloborodov, K.B. Efetov, A. Altland, F.W.J. Hekking, cond-mat/0006337.
[40] M.P.A. Fisher, B.P. Weichman, G. Grinstein, and D.S. Fisher, Phys. Rev. B **40**, 546 (1989).
[41] K. Liu and M. Fisher, J. Low. Temp. Phys. **10**, 655 (1973).
[42] C. Bruder, R. Fazio, G. Schön, Phys. Rev. B **47**, 342 (1993).
[43] L. Amico and V. Penna, Phys. Rev. B **62**, 1224 (2000).
[44] D. Das, S. Doniach, Phys. Rev. B **60**, 1261 (1999).
[45] I.F. Herbut, Phys. Rev. B **60**, 14503 (1999).
[46] T.K. Kopec and J.V. Josè, Phys. Rev. Lett. **84**, 749 (2000).
[47] L. Amico, Mod. Phys. Lett. B, **14**, 759 (2000).
[48] R. Fazio, G. Falci, and G. Giaquinta, Physica B **152**, 257 (1988).
[49] I. V. Yurkevich, I. V. Lerner, cond-mat/0007317.
[50] L.J. Geerligs, M. Peters, L.E.M. de Groot, A. Verbruggen, and J.E. Mooij, Phys. Rev. Lett. **63**, 326 (1989).
[51] H.S.J. van der Zant, W.J. Elion, L.J. Geerligs, and J.E. Mooij, Phys. Rev. B **54**, 10081

(1996).
[52] C.D. Chen, P. Delsing, D.B. Haviland, Y. Harada, and T. Claeson, Phys. Rev. B **51**, 15654 (1995).
[53] C.D. Chen, P. Delsing, D.B. Haviland, Y. Harada, and T. Claeson, Phys. Rev. B **54**, 9449 (1996).
[54] M. Strongin, R.S. Thompson, O.F. Kammemer, and J.E. Crow, Phys. Rev. B **1**, 2078 (1970).
[55] G. Deutscher, B. Bandyopadhay, T. Chui, P. Lindenfeld, W.L. McLean, and T. Worthington, Phys. Rev. Lett. **44**, 1150 (1980).
[56] S. Kobayashi, Y. Tada, and W. Sasaki, J. Phys. Soc. Jpn. **49**, 2075 (1980).
[57] B.G. Orr, H.M. Jaeger, A.M. Goldman, and C.G. Kuper, Phys. Rev. Lett. **56**, 378 (1986).
[58] H.M. Jaeger, D.B. Haviland, B.G. Orr, and
[59] S. Kobayashi, Surf. Sci. Reports **16**, 1 (1992). A.M. Goldman, Phys. Rev. B **40**, 182 (1989).
[60] R. Yagi, T. Yamaguchi, H. Kazawa, and S. Kobayashi, J. Phys. Soc. Jpn. **65**, 36 (1996).
[61] D.B. Haviland, Y. Liu, and A.M. Goldman, Phys. Rev. Lett. **62**, 2180 (1989).
[62] Y. Liu, K.A. Greer, B. Nease, D.B. Haviland, G. Martinez, J.W. Haley, and A.M. Goldman, Phys. Rev. Lett. **67**, 2068 (1991).
[63] A. Yazdani and A. Kapitulnik, Phys. Rev. Lett. **74**, 3037 (1995).
[64] H.S.J. van der Zant, H.A. Rijken and J.E. Mooij, J. Low Temp. Phys. **79**, 289 (1990).
[65] K.B. Efetov, Sov. Phys. JETP **51**, 1015 (1980).
[66] P. Fazekas, B. Muelshlegel, M. Schroter, Z. Phys. B **57**, 193 (1984).
[67] R. Fazio, and G. Giaquinta, Phys. Rev. B **34**, 4909 (1986).
[68] R.S. Fishman, Phys. Rev. B **38**, 4437 (1988).
[69] M.V. Feigel'man, S.E. Korshunov, and A.B. Pugachev, JETP Lett. **65**, 566 (1997).
[70] E. Simanek, Phys. Rev. B **23**, 5762 (1982).
[71] Yu.E. Lozovik and S.G. Akopov, J. Phys. C **14**, L31 (1981).
[72] D.M. Wood and D. Stroud, Phys. Rev. B **25**, 1600 (1982).
[73] A. Cuccoli, A. Fubini, V. Tognetti, R. Vaia Phys. Rev. B **61**, 11289 (2000).
[74] R.S. Fishman and D. Stroud, Phys. Rev. B **37**, 1499 (1988); Phys. Rev. B **38**, 280 (1988).
[75] L. Jacobs, J.V. Josè, M.A. Novotny, and A.M. Goldman, Phys. Rev. B **38**, 4562 (1988).
[76] J.V. Josè and C. Rojas, Physica B **203**, 481 (1994); Phys. Rev. B **54**, 12361 (1996).
[77] P. Fazekas, Z. Phys. B **45**, 215 (1980).
[78] B.-J. Kim, J. Kim, S.-Y. Park, M.Y. Choi Phys. Rev. B **56**, 395 (1997).
[79] J.V. Josè, Phys. Rev. B **29**, 2836 (1984).
[80] S. Doniach, Phys. Rev. B **24**, 5063 (1981).
[81] J. Kissner and U. Eckern, Z. Phys. B **91**, 155 (1993).
[82] J. Herz, Phys. Rev. B **14**, 1175 (1976).
[83] G. Parisi, *Statistical Field Theory*, Addison Wesley (1988).
[84] M.P.A. Fisher and G. Grinstein, Phys. Rev. Lett. **60**, 208 (1988).
[85] R. Savit, Rev. Mod. Phys. **52**, 453 (1980)
[86] J. Villain, J. Physique **36**, 581 (1975).
[87] J.V. José, L.P. Kadanoff, S. Kirkpatrick, and D.R. Nelson, Phys. Rev. B **16**, 1217

(1977).
[88] S. Elitzur, R. Pearson, and J. Shigemitzu, Phys. Rev. D **19**, 3638 (1979).
[89] B. Nienhuis, in: *Phase transitions and critical phenomena*, Vol. 11, ed. by C. Domb and J. L. Lebowitz (Academic Press, London, 1987), p.1.
[90] M. P. A. Fisher and D-H. Lee, Phys. Rev. B **39**, 2756 (1989).
[91] R. Fazio and G. Schön, Phys. Rev. B **43**, 5307 (1991).
[92] R. Fazio, U. Geigenmüller, and G. Schön, in *Quantum Fluctuations in Mesoscopic and Macroscopic Systems*, H.A. Cerdeira, *et al.* eds. (World Scientific, 1991), p. 214.
[93] J.E. Mooij, B.J. van Wees, L.J. Geerligs, M. Peters, R. Fazio, and G. Schön, Phys. Rev. Lett. **65**, 645 (1990).
[94] Ya.M. Blanter, and G. Schön, Phys. Rev. B **53**, 14534 (1996).
[95] C. Rojas, J.V. José, and A.M. Tikofsky, Bull. Am. Phys. Soc. **40**, p.68, B11-7 (1995).
[96] Ya.M. Blanter, R. Fazio, and G. Schön, Nucl. Phys. B **S58**, 79 (1997).
[97] H.S.J. van der Zant, L.J. Geerligs, and J.E. Mooij, Europhys. Lett. **19**, 541 (1992).
[98] R. Yagi, T. Tamaguchi, H. Kazawa and S. Kobayashi, J. Phys. Soc. Jpn. **66**, 2429 (1997)
[99] In the opposite limit with $C \ll C_0$ the vortex BKT transition temperature is $T_J = \frac{\pi E_J}{2}\left(1 - \frac{1}{3\pi}\frac{E_C}{E_J}\right)$ [76].
[100] In the case of normal arrays, the transition temperature is $E_C/4\pi$. This implies that, in the charge regime, an array has a lower resistance in the normal case compared to the superconducting one. (The factor 4 reduction of T_{ch} is related to the charge e of the quasi-particles as compared to $2e$ of the Cooper pairs). A higher resistance in 'superconducting' charging arrays has indeed been observed in Ref. [93].
[101] T.S. Tighe, M.T. Tuominen, J. M. Hergenrother, and M. Tinkham, Phys. Rev. B **47**, 1145 (1993).
[102] P. Delsing, C.D. Chen, and D.B. Haviland, Phys. Rev. B **50**, 3059 (1994).
[103] The case of normal arrays was investigated, for instance, by R. Yamada, S. Katsumoto, and S. Kobayashi, J. Phys. Soc. Jpn. **62**, 2229 (1993).
[104] M.T. Tuominen, J. M. Hergenrother, T.S. Tighe,and M. Tinkham, Phys. Rev. B **69**, 1997 (1992).
[105] H.S.J. van der Zant, C.J. Muller, L.J. Geerligs, C.J.P.M. Harmans, and J.E. Mooij, Phys. Rev. B **38**, 5154 (1988).
[106] W.Y. Shih and D. Stroud, Phys. Rev. B **30**, 6774 (1984); M.Y. Choi and S. Doniach, Phys.Rev. B **31**, 4516 (1985); T.C. Halsey, Phys. Rev. B **31**, 5728 (1985).
[107] P. Martinoli and C. Leemann, J. Low Temp. Phys. **118**, 699 (2000).
[108] D.R. Hofstadter, Phys. Rev. B **14**, 2239 (1976).
[109] R.S. Fishman, and D. Stroud, Phys. Rev. B **37** 1499, (1987).
[110] B.-J. Kim, G.-S. Jeon, M.-S. Choi, M. Y. Choi Phys. Rev. B **58**, 14524 (1998).
[111] M. Niemeyer, J. K. Freericks and H. Monien, Phys. Rev. B **60**, 2357 (1999).
[112] J.V. José, T.K. Kopeć, and C. Rojas, Physica B **222**, 353 (1996).
[113] M. Y. Choi and S. Doniach, Phys. Rev. B **31**, 4516 (1985).
[114] M.-C. Cha and S. M. Girvin, Phys. Rev. B **49**, 9794 (1994).
[115] E. Granato, Phys. Rev. B **48**, 7727 (1993); J. Appl. Phys. **75** 6690 (1994).
[116] V.A. Krupenin, D.E. Presnov, A.B. Zorin, J. Niemeyer J. Low Temp. Phys. **118**, 287 (2000).

[117] P. Lafarge, J.J. Meindersma, J.E. Mooij, in *Macroscopic Quantum Phenomena and Coherence in Superconducting Networks*, C. Giovanella and M. Tinkham Eds., (World Scientific, Singapore, 1995), pag. 94.
[118] J.K. Freericks and H. Monien, Europhys. Lett. **26**, 545 (1994); Phys. Rev. B **53**, 2691 (1996).
[119] G.G. Batrouni, R.T. Scalettar, and G.T. Zimanyi, Phys. Rev. Lett. **65**, 1765 (1990).
[120] R.T. Scalettar, G.G. Batrouni, and G.T. Zimanyi, Phys. Rev. Lett. **66**, 3144 (1991).
[121] C. Bruder, R. Fazio, A.P. Kampf, A. van Otterlo, and G. Schön, Physica Scripta T **42**, 159 (1992).
[122] L. Amico and V. Penna, Phys. Rev. Lett. **80**, 2189 (1998).
[123] G. Grignani, A. Mattoni, P. Sodano, and A. Trombettoni, Phys. Rev. B **61**, 1676 (2000).
[124] A.F. Andreev and I.M. Lifshitz, Sov. Phys. JETP **29**, 1107 (1969).
[125] A.J. Leggett, Phys. Rev. Lett. **25**, 1543 (1970).
[126] H. Matsuda and T. Tsuneto, Suppl. Prog. Theor. Phys **46**, 411 (1970).
[127] G.A. Lengua and J.M. Goodkind, J. Low. Temp. Phys. **79**, 251 (1990).
[128] M.W. Meisel, Physica **178**, 121 (1992); and references therein.
[129] E. Roddick and D.H. Stroud, Phys. Rev. B **48**, 16600 (1993).
[130] A. van Otterlo and K-H. Wagenblast, Phys. Rev. Lett. **72**, 3598 (1994).
[131] A. van Otterlo and K-H. Wagenblast, R. Baltin, C. Bruder, R. Fazio, and G. Schön, Phys. Rev. B **52**, 16176 (1995).
[132] G.G. Batrouni, R.T. Scalettar, G.T. Zimanyi, and A.P. Kampf, Phys. Rev. Lett. **74**, 2527 (1995); R.T. Scalettar, G.G. Batrouni, A.P. Kampf, and G.T. Zimanyi, Phys. Rev. B **51**, 8467 (1995).
[133] E. Frey and L. Balents, Phys. Rev. B **55**, 1050 (1997).
[134] C. Pich and E. Frey, Phys. Rev. B **57**, 13 712 (1998).
[135] L. Amico, G. Falci, R. Fazio, and G. Giaquinta, Phys. Rev B **55**, 1100 (1997).
[136] G. Murthy, D.P. Arovas, and A. Auerbach, Phys. Rev B **55**, 3104. (1997).
[137] M. Gabay and A. Kapitulnik, Phys. Rev. Lett. **71**, 2138 (1993).
[138] S.C. Zhang, Phys. Rev. Lett. **71**, 2142 (1993).
[139] L. Balents, D. R. Nelson, Phys. Rev. B **52**, 12951 (1995).
[140] K. Mullen, H.T.C. Stoof, M. Wallin, and S.M. Girvin, Phys. Rev. Lett. **72**, 4013 (1994).
[141] L. Balents, Europhys. Lett. **33**, 291, (1996).
[142] E. Roddick and D.H. Stroud, Phys. Rev. B **51**, 8672 (1995).
[143] D.R. Nelson, Phys. Rev. Lett. **60**, 1973 (1988).
[144] M.V. Feigel'man, V.B. Geshkenbein, L.B. Ioffe, and A.I. Larkin, Phys. Rev. B **48**, 16641 (1993).
[145] G. Blatter, M.V. Feigel'man, V.B. Geshkenbein, A.I. Larkin, and V.M. Vinokur, Rev. Mod. Phys. **66**, 1125 (1994).
[146] E. Frey, D.R. Nelson, and D.S. Fisher, Phys. Rev. B **49**, 9723 (1994).
[147] A. Schmid, Phys. Rev. Lett. **51**, 1506 (1983).
[148] J. S. Penttila, U. Parts, P. J. Hakonen, M. A. Paalanen, E. B. Sonin, Phys. Rev. Lett. **82**, 1004 (1999).
[149] see M. Devoret and H. Grabert in *Single Charge Tunneling* H. Grabert and M.H. Devoret Eds., NATO ASI series Vol.294 (Plenum, NY 1992).

[150] M.P.A. Fisher, G. Grinstein, and S.M. Girvin, Phys. Rev. Lett. **64**, 587 (1990).
[151] X.G. Wen and A. Zee, Int. J. Mod. Phys. (1990).
[152] Y. Takahide, R. Yagi, A. Kanda, Y. Ootuka, and S. Kobayashi, Phys. Rev. Lett. **85**, 1974 (2000).
[153] A.J. Rimberg, T.R. Ho, C. Kurdak, J. Clarke, K.L. Campman, and A.C. Gossard, Phys. Rev. Lett. **78**, 2632 (1997).
[154] S. Chakravarty, S.A. Kivelson, G.T. Zimanyi, and B.I. Halperin, Phys. Rev. B **35**, 7256 (1986).
[155] R.A. Ferrell and B. Mirhashem, Phys. Rev. B **37**, 648 (1988).
[156] A. Kampf and G. Schön, Physica **152**, 239 (1988).
[157] A. Kampf and G. Schön, Phys. Rev. B **36**, 3651 (1987).
[158] E. Simanek and R. Brown, Phys. Rev. B **35**, 7256 (1988).
[159] The effect of the phase-dependent renormalization of the capacitance was discussed in G. Falci, R. Fazio, V. Scalia and G. Giaquinta, Phys. Rev. B **43**, 13053 (1991).
[160] J. Choi and J.V. Josè, Phys. Rev. Lett. **62**, 1989 (1989).
[161] P. Delsing, C.D. Chen, D.B. Haviland, T. Bergsten, and T. Claeson, in *Superconductivity in Networks and Mesoscopic Structures*, C. Giovannella and C.J. Lambert Eds., American Institute, of Physics (1997).
[162] W. Zwerger, J. Low Temp. Phys. **72**, 291 (1988).
[163] S.V. Panyukov and A.D. Zaikin, J. Low Temp. Phys. **75**, 365 (1989); *ibid* **75**, 389 (1989).
[164] A. Kampf and G. Schön, Phys. Rev. B **37**, 5954 (1988).
[165] S. Chakravarty, G.L. Ingold, S.A. Kivelson, and A. Luther, Phys. Rev. Lett. **56**, 2303 (1986).
[166] S. Chakravarty, S.A. Kivelson, and G.T. Zimanyi, Phys. Rev. B **37**, 3283 (1988).
[167] G. Falci, R. Fazio, and G. Giaquinta, Europhys. Lett. **14**, 145 (1991).
[168] A. Cuccoli, A. Fubini, V. Tognetti, and R. Vaia, cond-mat/0002072.
[169] M.P.A. Fisher, Phys. Rev. B**36**, 1917 (1987).
[170] G.T. Zimanyi, Physica B **152**, 233 (1988).
[171] K-H., Wagenblast, A. van Otterlo, G. Schön, and G.T. Zimanyi, Phys. Rev. Lett. **78**, 1779(1997).
[172] H. Beck, Phys. Rev. B **49**, 6153 (1994).
[173] S.E.Korshunov, Phys. Rev. B **50**, 13616 (1994).
[174] K-H. Wagenblast, A. van Otterlo, G. Schön, and G.T. Zimanyi, Phys. Rev. Lett. **79**, 2730 (1998).
[175] S.V. Kravchenko, G.V. Kravchenk, J.E. Furneaux, V.M. Pudalov, and M. D'Iorio, Phys. Rev. B **50**, 8039 (1994).
[176] C. Castellani, C. Di Castro and M. Grilli, Phys. Rev. Lett. **75**, 4650 (1995).
[177] In two-dimensional systems the resistance per square is scale invariant.
[178] X.G. Wen, Phys. Rev. B **46**, 2655 (1992).
[179] S.M. Girvin, M. Wallin, M.-C. Cha, M.P.A. Fisher, and A.P. Young, Prog. Teor. Phys. Supp. **107**, 135 (1992).
[180] M.-C. Cha, M.P.A. Fisher, S.M. Girvin, M. Wallin, and A.P. Young, Phys. Rev. B **44**, 6883 (1991).
[181] R. Fazio and D. Zappalà, Phys. Rev. B **53**, R8883 (1996).

[182] E.S. Sørensen, M. Wallin, S.M. Girvin and A.P. Young, Phys. Rev. Lett **69**, 828 (1992).
[183] G.G. Batrouni, B. Larson, R.T. Scalettar, J. Tobochnik, and J. Wang, Phys. Rev. B **48**, 9628 (1993).
[184] M. Makivic, N. Trivedi, and S. Ullah, Phys. Rev. Lett **71**, 2307 (1993).
[185] M. Wallin, E.S. Sørensen, S.M. Girvin and A.P. Young, Phys. Rev. B **49**, 12115 (1994).
[186] K. Runge, Phys. Rev. B **45**, 13136 (1992)
[187] I. Herbut, Phys. Rev. Lett. **79**, 3502 (1997).
[188] A. van Otterlo, K-H. Wagenblast, R. Fazio and G. Schön, Phys. Rev. B **48**, 3316 (1993).
[189] A.P. Kampf and G.T. Zimanyi, Phys. Rev. B **47**, 279 (1993).
[190] I. Herbut, Phys. Rev. Lett. **81**, 3916 (1998).
[191] K. Damle and S. Sachdev, Phys. Rev. B **56**, 8714 (1997).
[192] K. Damle and S. Sachdev, Phys. Rev. B **57**, 8307 (1998).
[193] S. Sachdev, Phys. Rev. B **57**, 7157 (1998).
[194] K. Kim and P.B. Weichman, Phys. Rev. B **43**, 13583 (1991).
[195] E. Granato and J.M. Kosterlitz, Phys. Rev. Lett., **65**, 1267 (1990).
[196] D. Dalidovich, P. Phillips, Phys. Rev. Lett. **84**, 737 (2000).
[197] E.D. Chow, P. Delsing, and D.B. Haviland, Phys. Rev. Lett. **81**, 204 (1998); D. B. Haviland, K. Andersson, P. Agren, J. Low Temp. Phys., **118**, 733 (2000).
[198] P. Minnhagen, Rev. Mod. Phys. **59**, 1001 (1987).
[199] R.M. Bradley and S. Doniach, Phys. Rev. B **30**, 1138 (1984).
[200] This choice corresponds to choose equal lattice constants in space and time directions and therefore should not modify the critical properties of the transition.
[201] A.A. Odintsov, Phys. Rev. B **54**, 1228 (1996).
[202] W. Zwerger, Europhys. Lett. **9**, 421 (1989).
[203] S.E. Korshunov, Europhys. Lett. **9**, 107 (1989).
[204] P.A. Bobbert, R. Fazio, G. Schön, and G.T. Zimanyi, Phys. Rev. B **41**, 4009 (1990).
[205] P.A. Bobbert, R. Fazio, G. Schön, and A.D. Zaikin, Phys. Rev. B **45**, 2294 (1992).
[206] D.B. Haviland and P. Delsing, Phys. Rev. B **54**, R6857 (1996).
[207] J. Sólyom, Adv. Phys. **28**, 201 (1979).
[208] C.L. Kane and M.P.A. Fisher, Phys. Rev. Lett. **68**, 1220 (1992);
[209] R. Fazio, K.-H. Wagenblast, C. Winkelholz, and G. Schön Physica B **222**, 364 (1996)
[210] L.G. Glazman and A.I. Larkin, Phys. Rev. Lett. **79**, 3736 (1997).
[211] G. Falci, R. Fazio, A. Tagliacozzo, and G. Giaquinta, Europhys. Lett. **30**, 169 (1995).
[212] M.-S. Choi, M.Y. Choi, T. Choi and S.-I. Lee, Phys. Rev. Lett. **81**, 4240 (1998).
[213] R. Baltin and K.-H. Wagenblast, Europhys. Lett. **39**, 7 (1997).
[214] T. Kuehner and H. Monien, Phys. Rev. B **58**, R14741, (1998).
[215] M.P.A. Fisher, Phys. Rev. Lett. **65**, 923 (1990).
[216] A.F. Hebard and M.A. Paalanen, Phys. Rev. Lett. **65**, 927 (1990).
[217] M.A. Paalanen, A.F. Hebard, and R.R. Ruel, Phys. Rev. Lett. **69**, 1604 (1992).
[218] H.S.J. van der Zant, F.C. Fritschy, W.E. Elion, L.J. Geerligs, and J.E. Mooij, Phys. Rev. Lett. **69**, 2971 (1992).
[219] J.R. Phillips, H.S.J. van der Zant, J. White, and T.P. Orlando, Phys. Rev. B **47**, 5219 (1993).
[220] E. Simanek, Solid State Comm. **48**, 1023 (1983).

[221] U. Eckern and A. Schmid, Phys. Rev. B **39**, 6441 (1989).
[222] A.I. Larkin, Yu. Ovchinnikov and A. Schmid, Physica B **152**, 266 (1988).
[223] U. Eckern, in *Applications of Statistical and Field Theory Methods to Condensed Matter*, Edited by R. Bishop (Plenum, New York, 1990).
[224] C.J. Lobb, D.W. Abraham and M. Tinkham, Phys. Rev. B **27**, 150 (1983).
[225] T.P. Orlando, J.E. Mooij, and H.S.J. van der Zant, Phys. Rev. B **43**, 10218 (1991).
[226] E. Trias, T.P. Orlando and H.S.J. van der Zant Phys. Rev. 54**54**, 6568 (1996).
[227] R. Fazio, A. van Otterlo, and G. Schön, Europhys. Lett. **25**, 453 (1994).
[228] H.S.J. van der Zant, T.P. Orlando, S. Watanabe and S.H. Strogatz in Proc. of the NATO ARW on *Mesoscopic Superconductivity*, F. Hekking, G. Schön, and D.V. Averin Eds, Physica B **203**, 490 (1994).
[229] H. Suhl, Phys. Rev. Lett. **14**, 226 (1965).
[230] E. Simanek, Phys. Rev. B **32**, 500 (1985).
[231] J.-M. Duan and A.J. Leggett, Phys. Rev. Lett. **68**, 1216 (1992).
[232] R.D. Bock, J.R. Phillips, H.S.J. van der Zant, and T.P. Orlando, Phys. Rev. B **49**, 10009 (1994).
[233] It might be useful to express all the quantities characterizing the vortex motion including all the dimensional constants: Vortex mass $M_v = \frac{h}{16a^2}\ E_C^{-1}$, dissipation strength $\eta = \Phi_0^2/2R_e a^2$, lattice potential $U_v(x) = \frac{1}{2}\gamma E_J \sin(2\pi x/a)$, Lorentz force $\Phi_0 I/a$.
[234] T.J. Hagenaars, P.H.E. Tiesinga, J.E. van Himbergen, and J.V. Josè, in *Quantum Dynamics of Submicron Structures*, eds. H.A. Cerdeira *et al.*, (Kluwer, Dordrecht, 1995), p.617.
[235] H.S.J. van der Zant, F.C. Fritschy, T.P. Orlando, and J.E. Mooij, Phys. Rev. Lett. **66**, 2531 (1991).
[236] H.S.J. van der Zant, in *Superconductivity in Networks and Mesoscopic Structures*, C. Giovannella and C.J. Lambert Eds., American Institute of Physics (1997).
[237] T.J. Hagenaars, P.H.E. Tiesinga, J.E. van Himbergen, and J.V. Josè, Phys. Rev. B **50**, 1143 (1994).
[238] J.R. Phillips, H.S.J. van der Zant, and T.P. Orlando, Phys. Rev. B **50**, 9380 (1994).
[239] H.S.J. van der Zant, F.C. Fritschy, T.P. Orlando, and J.E. Mooij, Phys. Rev. B **47**, 295 (1993).
[240] T.S. Tighe, A.T. Jonson, and M. Tinkham, Phys. Rev. B **44**, 10286 (1991).
[241] E.B. Sonin, Phys. Rev. B **55**, 485 (1997).
[242] R. Fazio, A. van Otterlo, G. Schön, H.S.J. van der Zant, and J.E. Mooij, Helv. Phys. Acta **65**, 228 (1992).
[243] M.P.A. Fisher, Physica A **177**, 553 (1991)
[244] B.J. van Wees, H.S.J. van der Zant, and J.E. Mooij, Phys. Rev. B **35**, 7291 (1987).
[245] Yu.G. Makhlin and G.E. Volovik, Pis'ma Zh. Eksp. Teor. Fiz. **62**, 923 (1985) [JETP Lett. **62**, 941 (1995)].
[246] G. E. Volovik, cond-mat 9707136.
[247] There were some controversy in the literature on this point. It has been suggested that the offset charge in the equation of motion should be replaced with the electron number (F. Gaitan and S. R. Shenoy, Phys. Rev. Lett. **76**, 4404 (1996)). We do not share this point of view since only the offset charges, which are responsible for a local deviations from charge neutrality in the array, lead to the Magnus force.

[248] C. D. Chen, P. Delsing, D. B. Haviland, and T. Claeson in *Macroscopic Quantum Phenomena and Coherence in Superconducting Networks*, C. Giovanella, and M. Tinkham Eds., (World Scientific, 1995), pag. 121.
[249] A. Matsuda and T. Kawakami, Phys. Rev. Lett. **51**, 694 (1983).
[250] A. Fujimaki, K. Nakajima, and Y. Sawada, Phys. Rev. Lett. **59**, 2985 (1987).
[251] H.S.J. van der Zant, T.P. Orlando, S. Watanabe, and S.H. Strogatz, Phys. Rev. Lett. **74**, 174 (1995).
[252] S. Watanabe, S.H. Strogatz, H.S.J. van der Zant, and T.P. Orlando, Phys. Rev. Lett. **74**, 379 (1995).
[253] H.S.J. van der Zant, F.C. Fritschy, T.P. Orlando, and J.E. Mooij, Europhys. Lett. **18**, 343 (1992).
[254] K. Nakajima and Y. Sawada, J. App. Phys.**52**, 5732 (1981).
[255] P. Bobbert, Phys. Rev. B **45**, 7540 (1992).
[256] U. Geigenmüller, C.J. Lobb and C.B. Whan, Phys. Rev. B **47**, 348 (1993).
[257] U. Eckern and E.B. Sonin, Phys. Rev. B **47**, 505 (1993).
[258] A. van Otterlo, R. Fazio, and G. Schön, Physica B Physica B **203**, 504 (1994); A. van Otterlo, R. Fazio, and G. Schön, Physica B **194-196**, 1153 (1994).
[259] G. Luciano, U. Eckern, and J.G. Kissner, Europhys. Lett. **32**, 669 (1995).
[260] G. Luciano, U. Eckern, J.G. Kissner, and A. Tagliacozzo, J. Phys: Condens. Matter **8**, 1241 (1996).
[261] G. Luciano, U. Eckern, and A. Tagliacozzo, Phys. Rev. **B** 56, 14686 (1997)
[262] M-S. Choi, S-I. Lee, and M.Y. Choi, Phys. Rev. B **57**, 2720 (1998).
[263] A. van Oudenaarden and J.E. Mooij, Phys. Rev. Lett. **76**, 4947 (1996).
[264] A. van Oudenaarden, S.J.K. Várdy and J.E. Mooij, Phys. Rev. Lett. **77**, 4257 (1996).
[265] A. van Oudenaarden, B. van Leeuwen, M.P.P. Robbens, and J.E. Mooij, Phys. Rev. B **57**, 11684 (1998).
[266] W.J. Elion, I.I. Wachters, L.L. Sohn, and J.E. Mooij, Phys. Rev. Lett. **71**, 2311 (1993).
[267] A. van Oudenaarden S.J.K. Várdy, and J.E. Mooij, Czhec. J. Phys. **46**, 707 (1996).
[268] J.M. Martinis, M.H. Devoret, and J. Clarke, Phys. Rev. B **35**, 4682 (1987).
[269] U. Geigenmüller in *Macroscopic Quantum Phenomena*, T.D. Clark et al. Eds, (World Scientific, 1991).
[270] S.E. Korshunov, JETP Lett. **46**, 484 (1987).
[271] S.E. Korshunov, Physica B **152**, 261 (1988).
[272] L. B. Ioffe, B. N. Narozhny, Phys. Rev. B **58**, 11449 (1998).
[273] Y. Aharonov and A. Casher, Phys. Rev. Lett. **53**, 319 (1984).
[274] Y. Aharonov and D. Bohm, Phys. Rev. **115**, 485 (1959).
[275] A. Cimmino, G.I. Opat, A.G. Klein, H. Keiser, S.A. Werner, M. Arif, and R. Clothier, Phys. Rev. Lett. **63**, 380 (1989).
[276] B. Reznik and Y. Aharonov, Phys. Rev. D **40**, 4178 (1989).
[277] B.J. van Wees, Phys. Rev. Lett. **65**, 255 (1990).
[278] T.P. Orlando and K.A. Delin, Phys. Rev. B **43**, 8717 (1991).
[279] V.G. Lyssenko, G. Valusis, F. Löser, T. Hasche, K. Leo,M.M. Dignam, and K. Köhler, Phys. Rev. Lett. **79**, 301 (1997), and references therein.
[280] L.S. Kuzmin and D.B. Haviland, Phys. Rev. Lett. **67**, 2890 (1991).
[281] C.L. Kittel, *Introduction to Solid State Physics*, (John Wiley & Sons, New York, 1986),

Chapter 7.
[282] for a review see: E. Mendex and G. Bastard, Physics Today, June, page 34 (1993).
[283] For other effect of commensurability in Josephson arrays see M. Kardar, Phys. Rev. B **33**, 3125 (1986).
[284] P.W. Anderson, Phys. Rev. **109**, 1492 (1958).
[285] P. Niyaz, R.T. Scalettar, C.Y. Fong, and G.G. Batrouni, Phys. Rev. B **50**, 362 (1994).
[286] C. Bruder, L.I. Glazman, A.I. Larkin, J.E. Mooij, and A. van Oudenaarden, Phys. Rev. B **59**, 1383 (1999).
[287] N.F. Mott and W.D. Twose, Adv. Phys. **10**, 107 (1961).
[288] M. Büttiker, Y. Imry, and R. Landauer, Phys. Lett. A **96**, 365 (1983).
[289] Z. Hermon, A. Shnirman, and E. Ben Jacob, Phys. Rev. Lett. **74**, 4915 (1995).
[290] M.Y. Choi, Phys. Rev. Lett. **71**, 2987 (1993).
[291] R. Fazio, A. van Otterlo, and A. Tagliacozzo, Europhys. Lett. **36**, 135 (1996).
[292] H.S.J. van der Zant, T.P. Orlando, S. Watanabe and S.H. Strogatz in *Quantum Dynamics of Submicron Structures*, eds. H.A. Cerdeira *et al.*, (Kluwer, Dordrecht, 1995), p. 587.
[293] Z. Hermon, A. Stern, E. Ben-Jacob, Phys. Rev. B **49**, 9757 (1994).
[294] R. Prange and S. Girvin, *The Quantum Hall effect*, Springer Verlag,Berlin (1987).
[295] Yu.V. Nazarov and A.A. Odintsov, Physica B **194-196**, 1737 (1994); A.A. Odintsov and Yu.V. Nazarov, Phys. Rev. B **51**, 113 (1995).
[296] M.Y. Choi, Phys. Rev. B **50**, 10088 (1994).
[297] A. Stern, Phys. Rev. B **50**, 10092 (1994).
[298] A. Ekert and R. Jozsa, Rev. Mod. Phys. **68**, 733 (1996).
[299] A. Steane, Rep. Prog. Phys. **61**, 117 (1998).
[300] Y. Makhlin, G. Schön and A. Shnirman, to be published in Rev. Mod. Phys. .
[301] A. Barenco, Proc. R. Soc. London A **449**, 679 (1995).
[302] G.M. Palma, K.-A. Suominen and A.K. Ekert, Proc. R. Soc. London A **452**, 567 (1996); W. Zurek, Physics Today **44**, 36 (1991).
[303] A. Shnirman, G. Schön and Z. Hermon, Phys. Rev. Lett. **79**, 2371 (1997); Y. Makhlin, G. Schön and A. Shnirman, Nature **398**, 305 (1999).
[304] D.A. Averin, Sol. State Comm. **105** 659 (1998).
[305] J.E. Mooij, T.P. Orlando, L. Tian, C. van der Wal, L. Levitov, S. Lloyd, and J.J. Mazo, Science **285**, 1036 (1999)
[306] L.B. Ioffe, V.B. Geshkenbein, M.V. Feigelman, A.L. Faucher, and G. Blatter, Nature **398**, 679 (1999).
[307] R. Fazio, G.M. Palma and J. Siewert, Phys. Rev. Lett. **81**, 5385 (1999).
[308] G. Falci, R. Fazio, G.M. Palma, J. Siewert, and V. Vedral, Nature **403**, 869 (2000).
[309] M. Matters, W. Elion, and J.E. Mooij, Phys. Rev. Lett. **75**, 721 (1995).
[310] V. Bouchiat, D. Vion, P. Joyez, D. Esteve, and M. Devoret, Physica Scripta **T76**, 165 (1998).
[311] Y. Nakamura, Yu.A. Pashkin, J.S. Tsai, Nature **398**, 786 (1999).
[312] J.R. Friedman, V. Patel, W. Chen, S.K. Tolpygo and J.E. Lukens, Nature **406**, 43 (2000).
[313] C.H. van der Wal, A.C.J. ter Haar, F.K. Wilhelm, R.N. Schouten, C.J.P.M. Harmans, T.P. Orlando, S. Lloyd, J.E. Mooij, to be published in Science.

[314] T.A. Fulton and G.J. Dolan, Phys. Rev. Lett. **59**, 109 (1987).
[315] Similar considerations for $E_{\rm C} \gg E_{\rm J}$ leads to the effective action of charges in JJA. In particular in the adiabatic limit it is possible to obtain the charge mass $M_{\rm q} = (a^2 E_{\rm J})^{-1}$ Thus, in two dimensional arrays of Josephson junctions a charge-vortex duality exists. In the limiting case $E_J \gg E_C$ the vortices are well-defined. They form Coulomb gas, and can be considered as particles with masses. In the opposite limit, $E_C \ll E_J$, the charges are the relevant excitations. The properties of charges are the same as the properties of vortices in the corresponding limiting case. An analogous situation occurs in 1D Josephson chains, in the presence of extra inductive terms charge solitons with a larger mass may appear as topological excitations (see Z.Hermon, E.Ben-Jacob, and G.Schön, Phys. Rev. B **54**, 1234 (1996)).

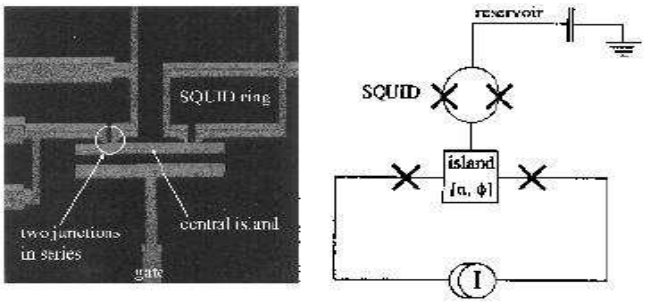

Fig 1 - R. Fazio and H. van der Zant

FIG. 1. Left hand side: a Scanning-Electron-Microscope (SEM) photograph of the Heisenberg transistor. The leads in upper, left corner are used to perform a four-terminal measurement on the two junctions in series. Offset-charges on the central island are nulled out by the gate capacitor situated below the central island. (Picture taken by W.J. Elion.) Right hand side: a schematic drawing of the Heisenberg transistor [17]. The phase and the charge on the island are quantum mechanical conjugated variables. By varying the flux through the SQUID ring the effective Josephson energy is tuned and, as a result, phase fluctuations on the central island can be varied. (Reprinted by permission from Nature **371**, 594 (1994) copyright 1994 Macmillan Magazines Ltd.)

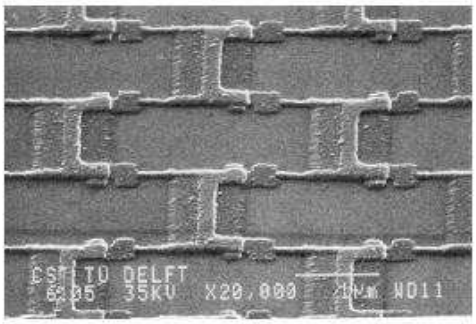

Fig 2 - R. Fazio and H. van der Zant

FIG. 2. A Scanning-Electron-Microscope (SEM) photograph of a two-dimensional, square array of small tunnel junctions produced by shadow evaporation. The white bar is 1 μm long. (Picture taken from the Ph.D. thesis of L.J. Geerligs, Delft 1990 (unpublished).)

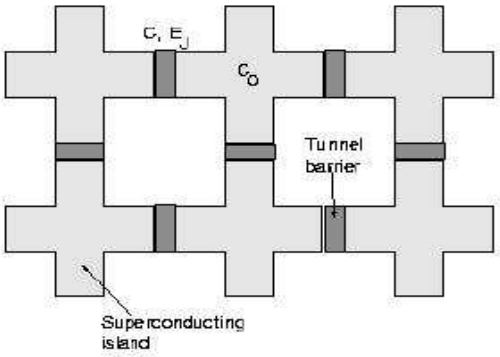

Fig 3 - R. Fazio and H. van der Zant

FIG. 3. A Josephson array consists of a regular network of superconducting islands weakly coupled by tunnel junctions. Each junction is characterized by the Josephson coupling E_J and the junction capacitance C; each island by the capacitance to the ground C_0.

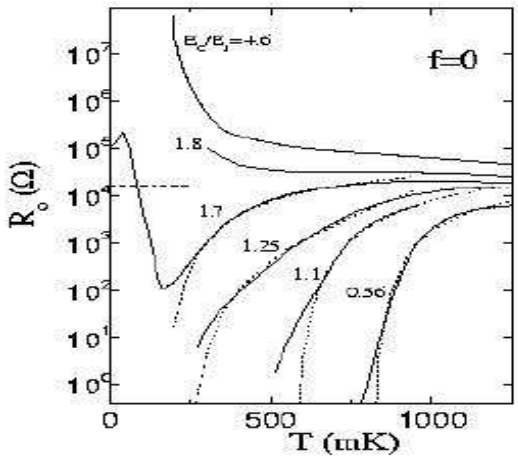

Fig 4 - R. Fazio and H. van der Zant

FIG. 4. The zero-field linear resistance per square measured as a function of the temperature for six different square arrays. The curved dashed lines are fits to the vortex-BKT square root cusp formula. The dashed horizontal line indicates the zero-temperature universal resistance at the S-I transition calculated in Ref. [150]. (From Ref. [51].)

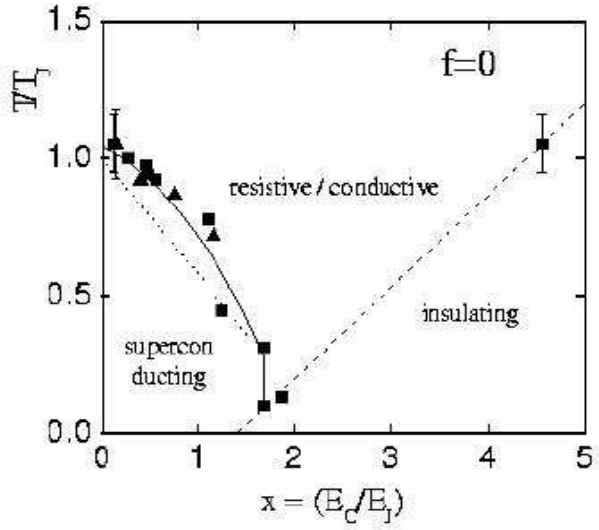

Fig 5 - R. Fazio and H. van der Zant

FIG. 5. Measured phase diagram in zero magnetic field for square (solid squares) and triangular (solid triangles) arrays showing the S-I transition at $E_C/E_J \sim 1.7$. The solid line is a guide to the eye connecting the data points and the dotted line on the superconducting side represents the result of the calculation of Ref. [76]. (From Ref. [51].)

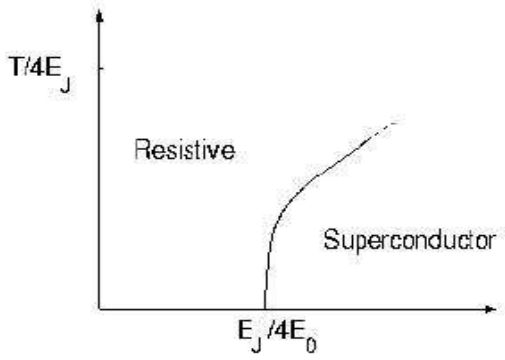

Fig 6 - R. Fazio and H. van der Zant

FIG. 6. Sketch of the phase diagram for short-range interaction between charges. The phase incoherent state is resistive with an activated behavior of the resistance. At $T = 0$ the array is a insulator. The dependence of the quantum critical point on the capacitance matrix is all contained in E_0.

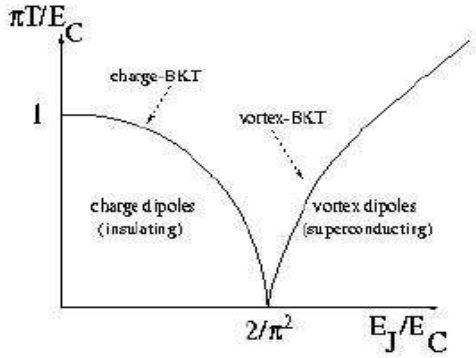

Fig 7 - R. Fazio and H. van der Zant

FIG. 7. The phase diagram for a quantum JJA in the limit of long-range (logarithmic) interaction between charges. Similarly to vortices the charges undergo a BKT transition leading to insulating behavior at low temperature and small E_J/E_C ratio.

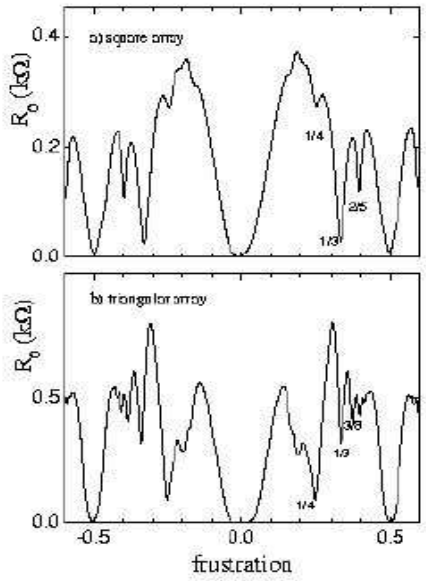

Fig 8 - R. Fazio and H. van der Zant

FIG. 8. Zero-bias resistance versus magnetic frustration for a square (a) and a triangular (b) array. The dip at $f = 1/2$ is the most pronounced one in both figures. In the triangular array the dip at $f = 1/4$ is more pronounced than the one at $f = 1/3$. In the square array the opposite occurs. (From Ref. [51].)

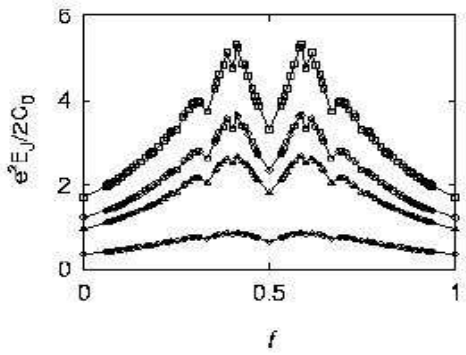

Fig 9 - R. Fazio and H. van der Zant

FIG. 9. Phase boundaries between the Mott insulating phase (below each curve) and the superconducting phase (above). Boundaries for various ratios of the junction capacitance C to the self-capacitance C_0 are shown: $C/C_0 = 0.0001(\square)$, $0.1(\circ)$, $0.2(\triangle)$, and $1.0(\diamond)$. (From Ref. [110].)

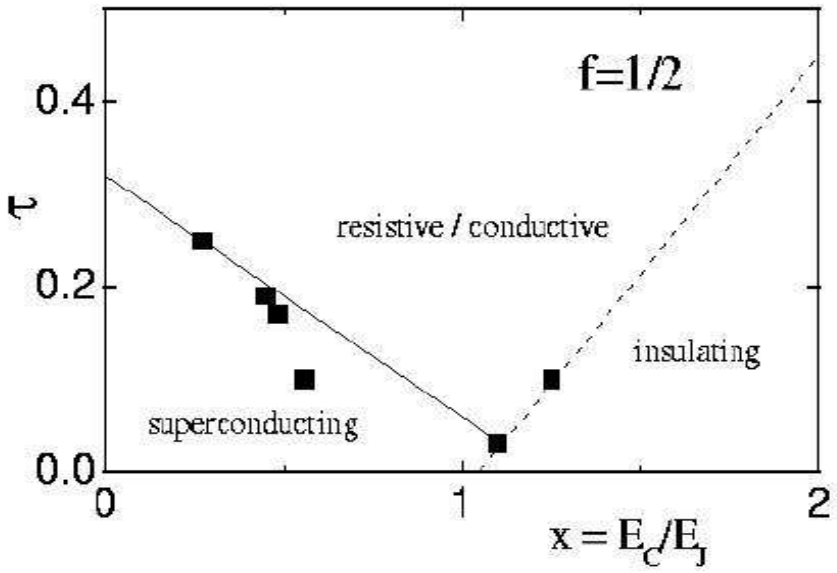

Fig 10 - R. Fazio and H. van der Zant

FIG. 10. Measured phase diagram for square arrays at $f = 1/2$, showing the S-I transition at $E_C/E_J \sim 1.2$. In the figure the temperature axis is normalized to the Josephson coupling, i.e., $\tau = T/E_J$. The solid and dashed lines are guides to the eye connecting the data points. (From Ref. [51].)

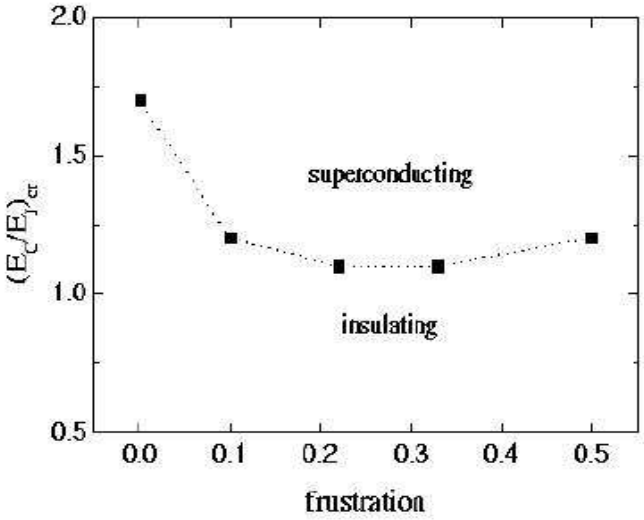

Fig 11 - R. Fazio and H. van der Zant

FIG. 11. Measured phase diagram for square arrays in a magnetic field. Below the dotted line samples become superconducting at low temperatures; above this line samples become insulating. At non-commensurate magnetic fields, the S-I transition is not sharp and there is an additional (intermediate) metallic region not shown in the figure. (From Ref. [51].)

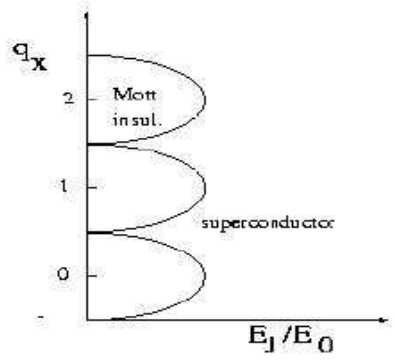

Fig 12 - R. Fazio and H. van der Zant

FIG. 12. The $T = 0$ phase diagram in the limit of on-site interaction as a function of the charge frustration. At the values of q_x for which two charge states are degenerate, the superconducting phase extends to arbitrary small Josephson coupling.

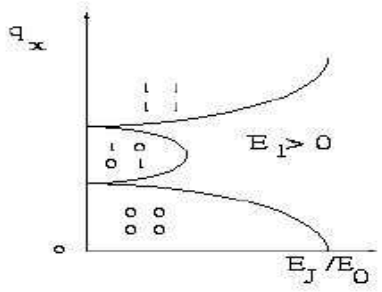

Fig 13 - R. Fazio and H. van der Zant

FIG. 13. The $T = 0$ phase diagram calculated with on-site interaction and a small nearest neighbor charging term E_1. Around $q_x = 1/2$ the half-integer lobe appears. Inside the lobes, each number represents the number of Cooper pairs on a particular island. For example, the intermediate lobe, centered around $q_x = 1/2$ has a checkerboard structure.

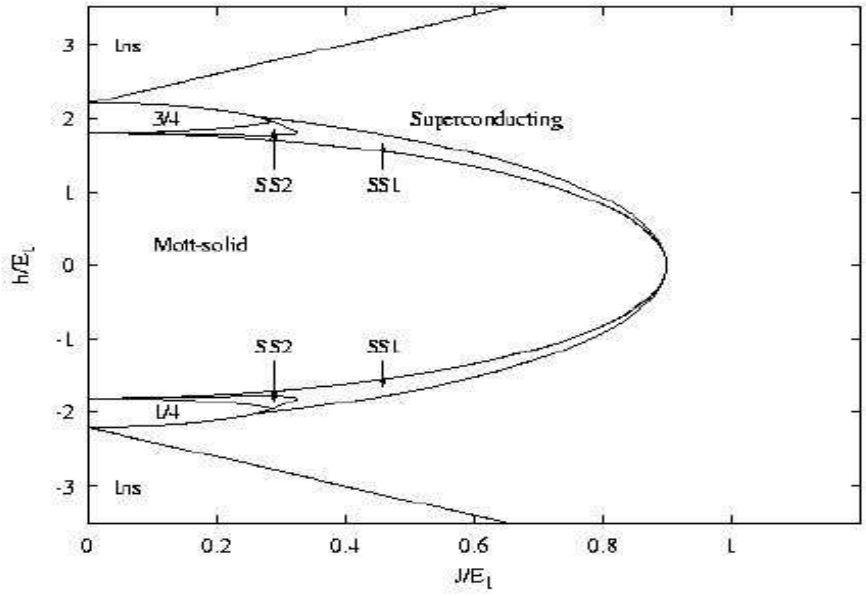

Fig 14 - R. Fazio and H. van der Zant

FIG. 14. Mean-field phase diagram in the presence of charge frustration obtained in the hard-core limit. As discussed in the text the fictitious field h is related to $q_x - 1/2$ and the coupling J corresponds to E_J. In the figure nn and nnn charging terms are different from zero $E_2 = 0.1E_1$. The central lobe corresponds to the half-filling case and the two small ones on the side are the quarter-filling lobes. Finally SS1 and SS2 are different types of supersolid. (From Ref. [42].)

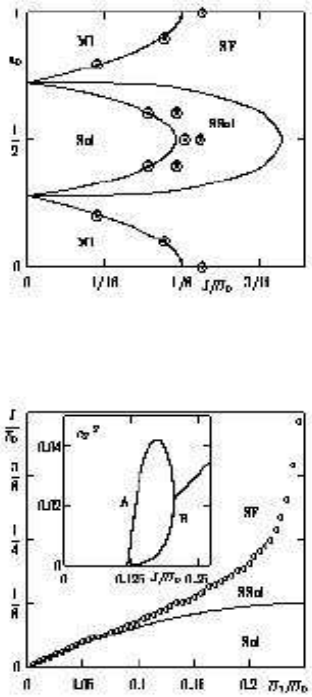

Fig 15 - R. Fazio and H. van der Zant

FIG. 15. Top: Mean-field phase diagram for soft-core bosons, as obtained from the analysis of the QPM with on-site and nearest-neighbor ($E_1/E_0 = 1/5$) interaction. The symbols are the Monte Carlo data (the region between the dotted circles and the crossed circles is the supersolid). The checkerboard charge-density wave is denoted by "Sol", the supersolid phase by "SSol", the superfluid phase is denoted by "SF" and the Mott-insulating phase by "MI". Bottom: Supersolid region "SSol" at q_x= 0.5 as a function of U_1/U_0 in the mean-field approximation of. Inset: Occupation-number probability $|c_2|^2$ at q_x= 0.5 for the two sub-lattices A and B at the particular value of $E_1/E_0 = 0.2$. (The notation is slightly different from that used in this review, $U_0 \to E_0$, $U_1 \to E_1$, $J \to E_J$, $n_0 \to q_x$). (From Ref. [131].)

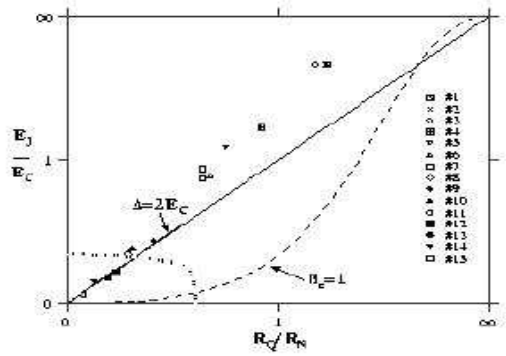

Fig 16 - R. Fazio and H. van der Zant

FIG. 16. Measured low-temperature phase diagram for fifteen square arrays plotted as the E_J/E_C-ratio vs. R_Q/R_N. Samples $\sharp\, 1-8$ show a decreasing resistance as temperature is lowered (superconducting arrays). Samples $\sharp\, 9-15$ show an increasing resistance as temperature is lowered (insulating arrays). This classification roughly agrees with the theoretical prediction [91] which states that insulating arrays are to be found in the region bounded by the dotted line. Only the insulating samples $\sharp\, 9-11$ fall slightly outside this area. The diagonal line represents $\Delta_0 = 2E_C$ and the dashed line corresponds to a Stewart McCumber parameter of $\beta_c = 1$. (From Ref. [161].)

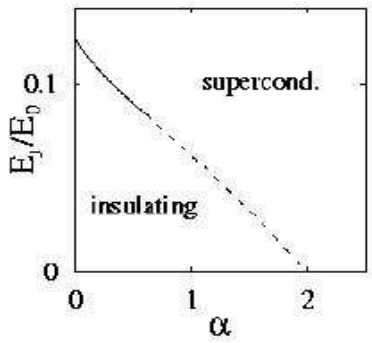

Fig 17 - R. Fazio and H. van der Zant

FIG. 17. The phase diagram at $T = 0$ in the local damping model. Along the solid line the conductivity is universal, whereas it is a function of the dissipation strength along the dotted line. (From Ref. [171].)

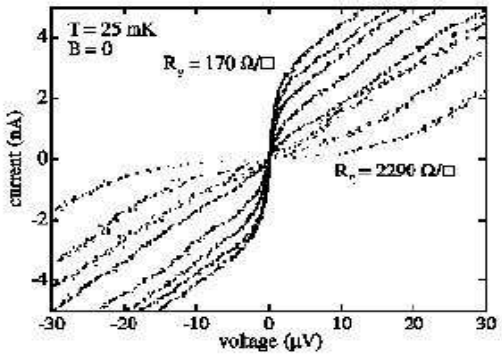

Fig 18 - R. Fazio and H. van der Zant

FIG. 18. Measured array $I-V$ characteristics for eight values of the back-gate voltage corresponding to different ground plane resistances R_g. The $I-V$.s change from superconducting-like to insulator-like as a function ofR_g. (From Ref. [153].)

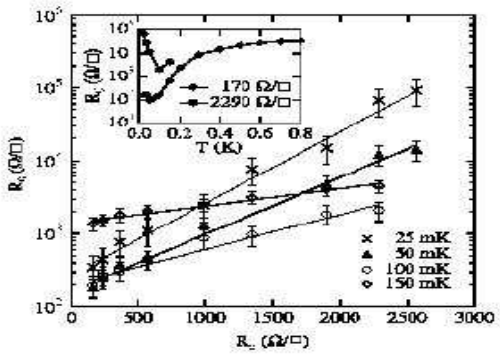

Fig 19 - R. Fazio and H. van der Zant

FIG. 19. Measured zero-bias array resistance R_0 as a function of the ground plane resistance R_g. The inset shows the temperature dependence of the resistance. (From Ref. [153].)

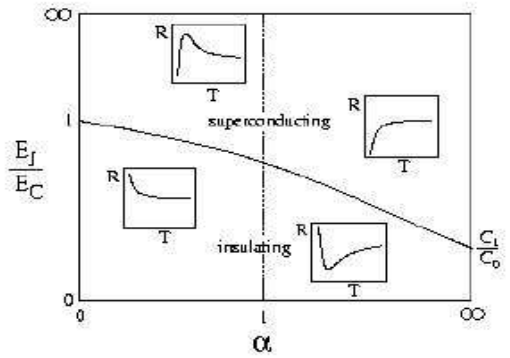

Fig 20 - R. Fazio and H. van der Zant

FIG. 20. Calculated phase diagram of an array coupled capacitively to a 2DEG. The insets show the resistance as a function of the temperature in the different regions of the phase diagram. (From Ref. [174].)

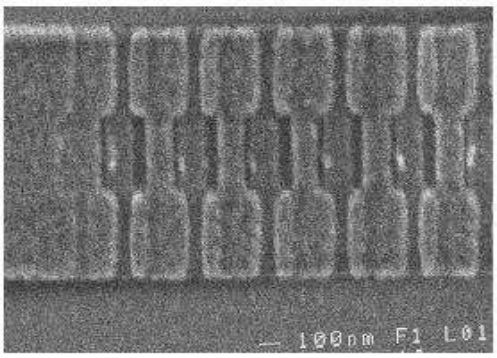

Fig 21 - R. Fazio and H. van der Zant

FIG. 21. A Scanning-Electron-Microscope (SEM) image of a SQUID chain. (From Ref. [197]).

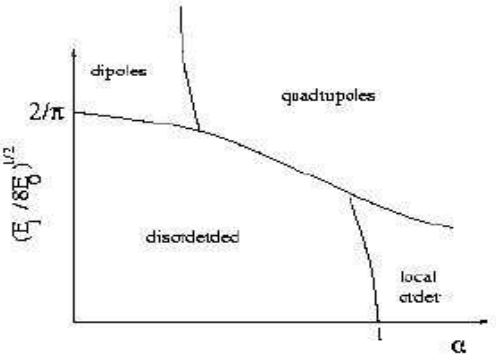

Fig 22 - R. Fazio and H. van der Zant

FIG. 22. Calculated phase diagram of a Josephson chain shown as a function of the Josephson coupling and the dissipation strength. The dissipative part of the action leads to two new phases. For $\alpha > 1/2$ the dipoles are bound in a gas of quadrupoles and moreover for strong dissipation there is an additional phase transition which separate the quadrupole phase from a phase in which the system shows local order. (From Ref. [204]).

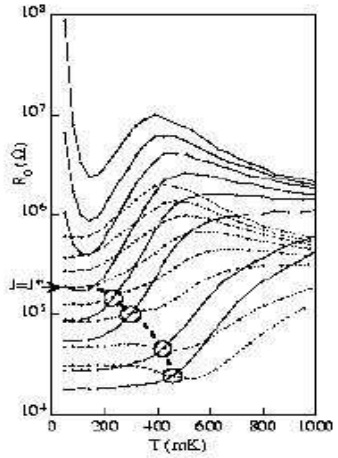

Fig 23 - R. Fazio and H. van der Zant

FIG. 23. Resistance vs. temperature for eight values of the magnetic field in the range $0-64$ G. The two sets of curves correspond to two different one-dimensional arrays with $N = 255$ (solid lines) and $N = 63$ (dashed lines) junctions. The longer array shows a sharper S-I transition. At the point $J^\star$ ($J = \sqrt{E_J/E_C}$) the resistance is length independent. (From Ref. [197].)

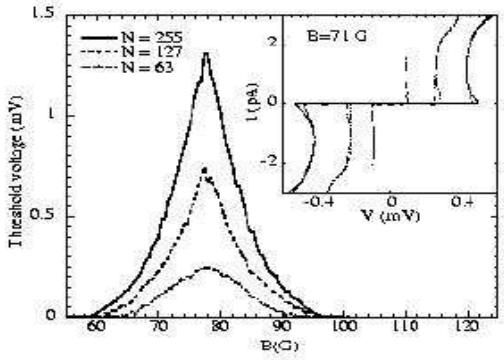

Fig 24 - R. Fazio and H. van der Zant

FIG. 24. The magnetic field dependence of the threshold voltage for one-dimensional arrays of different length. The inset shows the corresponding $I - V$ curves. (From Ref. [197].)

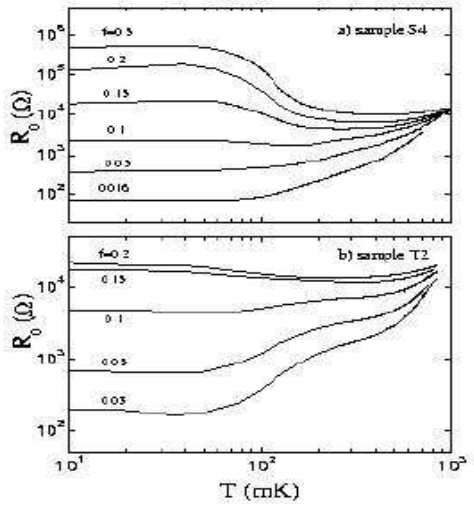

Fig 25 - R. Fazio and H. van der Zant

FIG. 25. Temperature dependence of the resistance for a square (a) and triangular (b) 2D Josephson array measured at different applied magnetic fields. The field tuned S-I transition occurs at that frustration where the temperature dependence of the resistance changes sign. In both cases this change occurs at $f = 0.10 - 0.15$. (From Ref. [51].)

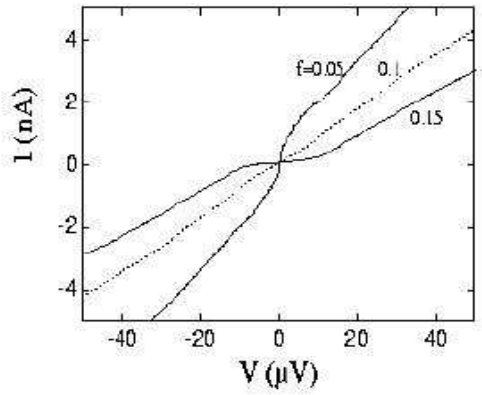

Fig 26 - R. Fazio and H. van der Zant

FIG. 26. $I - V$ characteristics measured at low temperature (10 mK) for three values of the applied field. The square 2D array has an (E_C/E_J ratio of 1.25. The crossover from the superconducting to the insulating behavior is related to the field tuned S-I transition. (From Ref. [51].)

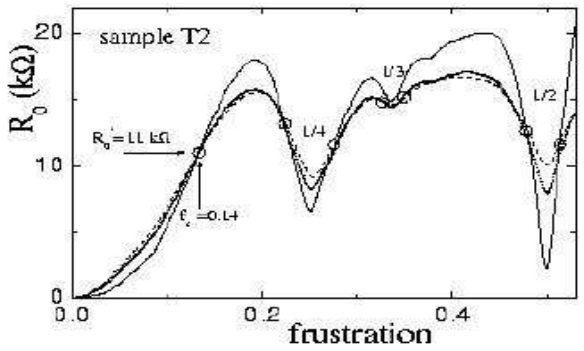

Fig 27 - R. Fazio and H. van der Zant

FIG. 27. Field dependence of the resistance of a triangular 2D array measured at different temperatures, $T = 50$ mK (solid line), $T = 120$ mK (dotted line), and $T = 160$ mK (dashed line). The field-tuned transition is observed around different fractional values of the frustration indicated by the open circles. (From Ref. [51].)

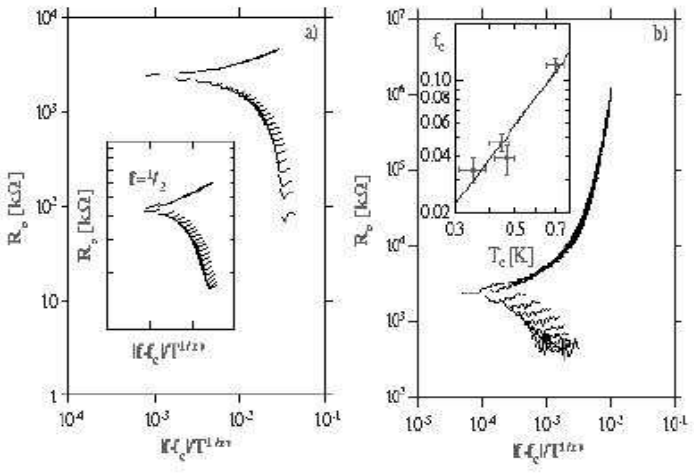

Fig 28 - R. Fazio and H. van der Zant

FIG. 28. Resistance as a function of the scaling parameter $|f - f_c|T^{-1/z_B\nu_B}$ for two different arrays (data taken in the range $0 < f < 0.2$). The data collapse onto a single curve: the upper part for the insulating transition and the lower part for the superconducting transition. The inset in the figure on the left shows the scaling for the array close to full frustration (data taken in the range $0.5 < f < 0.6$). The inset in the figure on the right shows a log-log plot of the critical frustrations f_c as a function of the BKT transition temperature for the four measured samples. The line through the data yields a critical exponent $z = 1.05$. (From Ref. [52].)

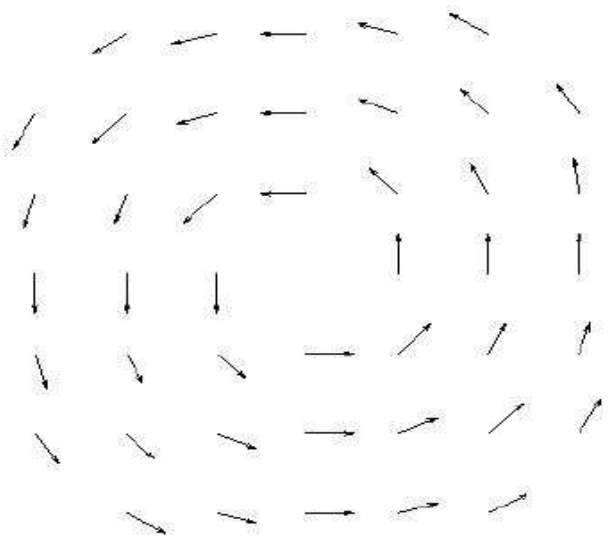

Fig 29 - R. Fazio and H. van der Zant

FIG. 29. Phase configuration of a vortex configuration. The arrows indicate the phase of each island with respect to a given reference direction.

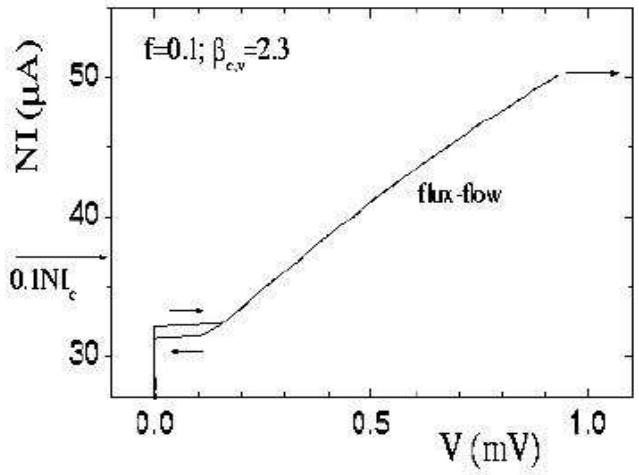

Fig 30 - R. Fazio and H. van der Zant

FIG. 30. A current-voltage characteristic of an underdamped 2D square, aluminum array measured at low temperature (10 mK) in a magnetic field of 0.1 Φ_0 applied per cell ($f = 0.1$). The arrow at the left indicates the expected depinning current of $0.1NI_c$ with N the number of junctions perpendicular to the direction of the current flow. For small voltages hysteresis is seen. The flux-flow region is found above the depinning current but below the current at which row switching sets in (arrow at the left). (From Ref. [236].)

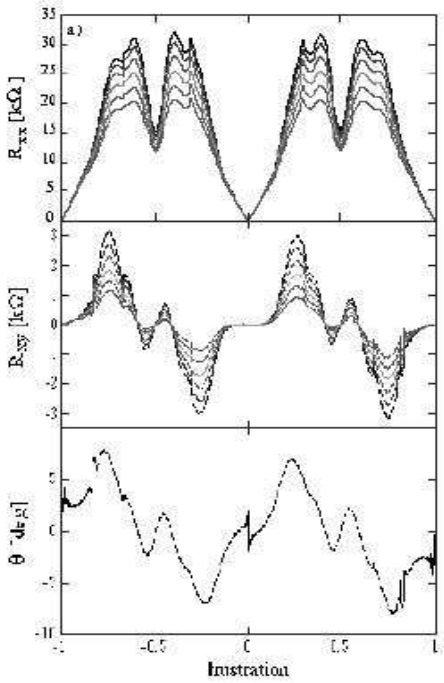

Fig 31 - R. Fazio and H. van der Zant

FIG. 31. Longitudinal resistance R_{0xx} (a) and the Hall resistance R_{0xy} (b), and the Hall angle Θ (c) as a function of frustration. R_{0xx}, and R_{0xy} are shown for various temperatures ranging from $T = 20$ (top), 75, 100, 125, 150, 175 mK. R_{0xx} is symmetric around $f = 0$ and $f = \pm 1/2$ whereas R_{0xy} changes sign upon passing through these frustrations. (From Ref. [161].)

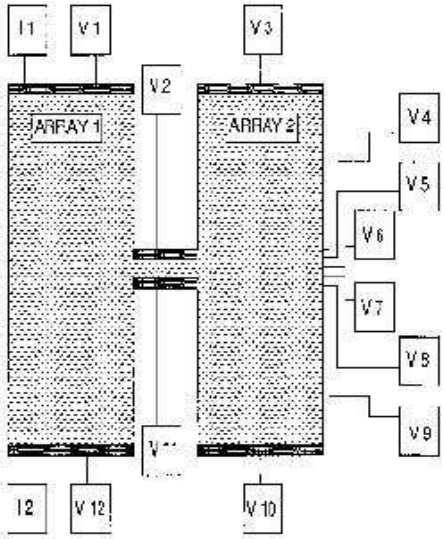

Fig 32 - R. Fazio and H. van der Zant

FIG. 32. Sample lay-out used to measure ballistic vortices in 2D Josephson arrays. (From Ref. [97].)

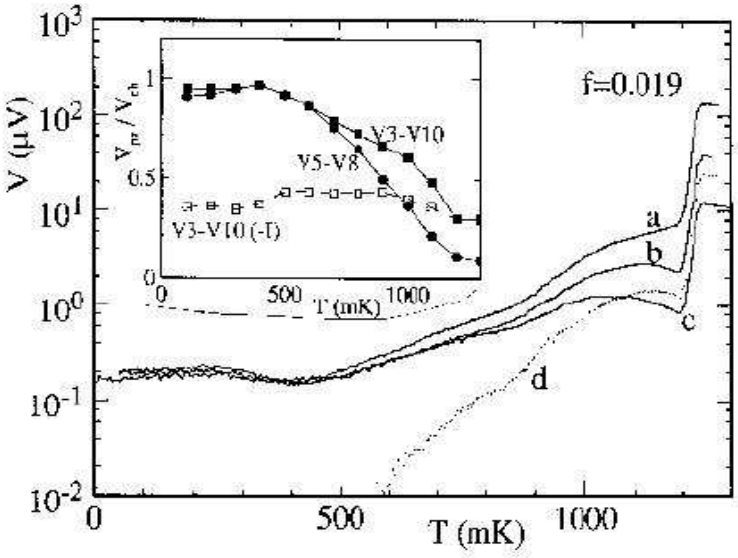

Fig 33 - R. Fazio and H. van der Zant

FIG. 33. Voltage vs. Temperature measured across the channel (a), between probes V3 and V10 (b), between probes V5 and V8 (c), and between probes V3 and V4 (d). In the inset voltages are plotted in units of the voltage across the channel. The dashed line corresponds to the voltage across V3-V10 when the current direction is reversed. At low temperatures, the voltage across the two probes opposite from the channel is almost equal to the voltage across the channel: all vortices that go through the channel leave the array between V7 and V8. With reversed current direction vortices are accelerated in the opposite direction and no ballistic motion is observed. (From Ref. [97].)

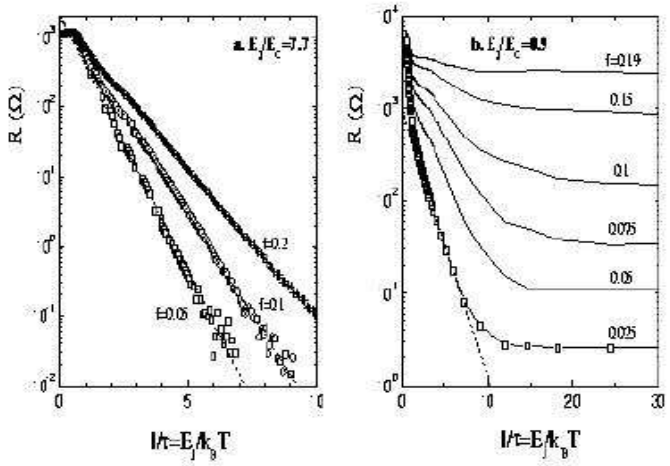

Fig 34 - R. Fazio and H. van der Zant

FIG. 34. Measured zero-bias resistance per junction versus the inverse normalized temperature measured for two different square arrays. At low temperatures the resistance of the sample with the smaller E_J/E_C ratio (b) is temperature independent indicative for quantum tunneling of vortices. (From Ref. [236].)

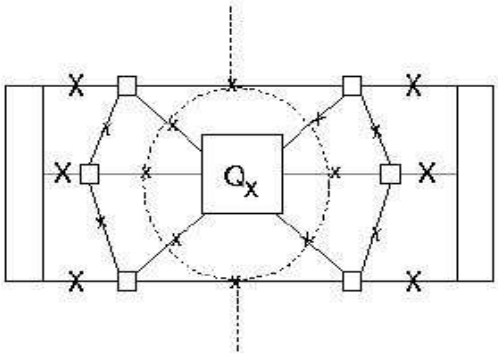

Fig 35 - R. Fazio and H. van der Zant

FIG. 35. Schematic drawing of the hexagon-shaped Josephson array to measure vortex interference. (From Ref. [266].)

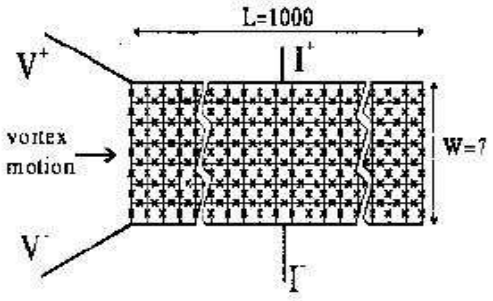

Fig 36 - R. Fazio and H. van der Zant

FIG. 36. A sketch of the sample layout of a quasi one-dimensional Josephson array. The current is injected in the middle while the voltage probes are situated at the end of the busbars. (From Ref. [263].)

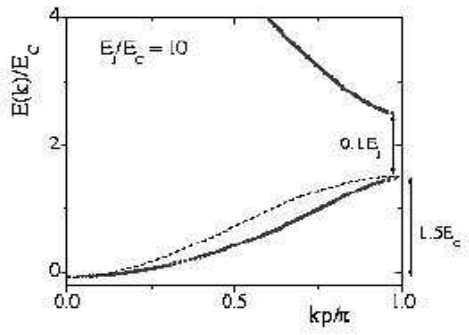

Fig 37 - R. Fazio and H. van der Zant

FIG. 37. Schematic drawing of the energy bands for a vortex moving in a quasi-1D Josephson array. Dots: numerical calculated energy bands starting from Schrödingers equation with a cosine potential. The dashed line shows the first band of a cosinusoidal dispersion relation with the same band width. (From Ref. [236].)

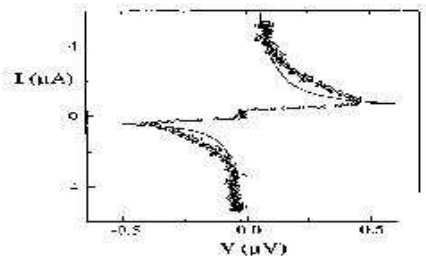

Fig 38 - R. Fazio and H. van der Zant

FIG. 38. A nose-shaped I-V characteristic indicative for Bloch oscillating vortices. Data (circles) has been obtained in a quasi-1D array with size 7 by 1000 and has been measured at 10 mK for a 1D vortex density (n) of 0.04. The solid line is the analytical result discussed in the text. (From the Ph.D. thesis of A. van Oudenaarden, Delft, 1998, unpublished.)

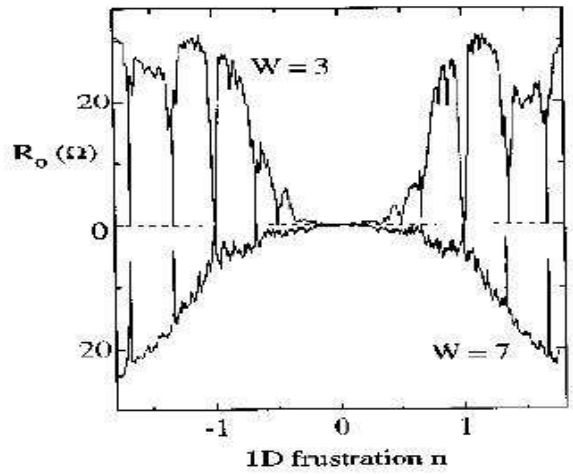

Fig 39 - R. Fazio and H. van der Zant

FIG. 39. Zero-bias resistance R_0 as a function of the one-dimensional vortex density ($n = Wf$) for two samples with different widths W. The sample length is 1000 cells and data has been obtained at 30 mK. The bottom curve ($W = 7$) is mirrored with respect to the x-axis for clarity. (From Ref. [265].)

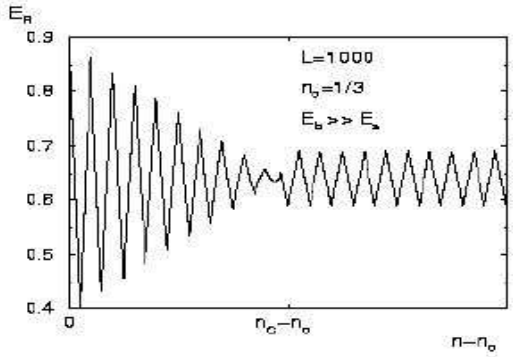

Fig 40 - R. Fazio and H. van der Zant

FIG. 40. Activation energy as a function of $n - n_0$ (n_0 is the commensurate density) in the case that the boundary pinning E_b dominates over the soliton formation energy E_s. On the incommensurate side of the transition, $n > n_C$, solitons form spontaneously and the physics is determined by boundary pinning and the elastic energy. (From Ref. [286].)

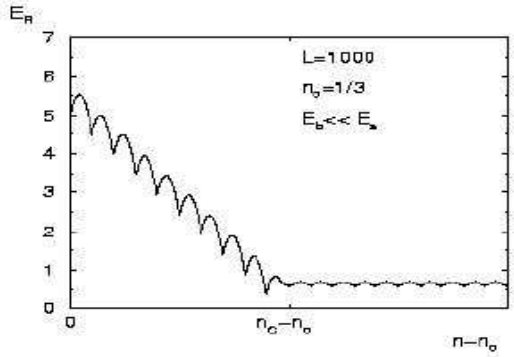

Fig 41 - R. Fazio and H. van der Zant

FIG. 41. Activation energy as a function of $n - n_0$ when the soliton formation energy $E_s$dominates over the boundary pinning E_b (opposite limit as considered in Fig. 40). (From Ref. [286].)

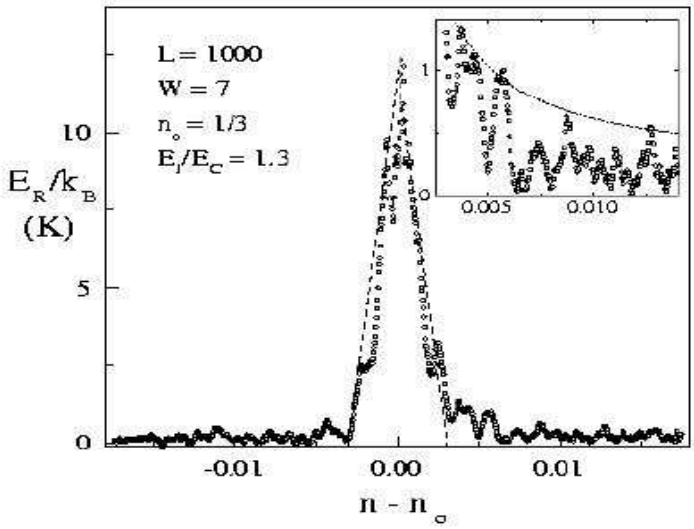

Fig 42 - R. Fazio and H. van der Zant

FIG. 42. Measured activation energy of an array of 1000×7 cells with $E_J = 0.9$ K and $E_C = 0.7$ K. The dashed line is a fit to the data yielding the width of the Mott region. The inset shows E_R inside the Mott phase. (From Ref. [286].)

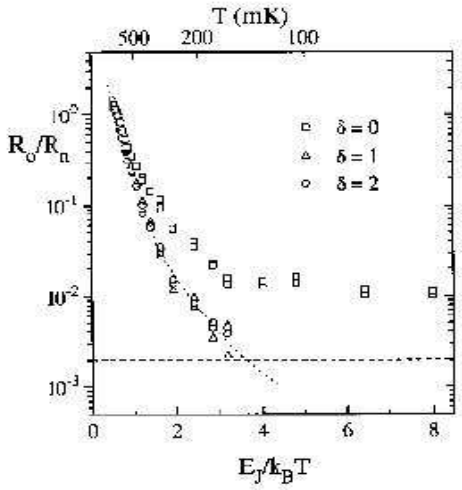

Fig 43 - R. Fazio and H. van der Zant

FIG. 43. Arrenius plot of the linear resistance for the ordered (squares) and for the disordered (triangles, circles) arrays. At low temperatures (right hand side of the figure), the resistance of the disordered arrays (triangles and circles) has dropped below measuring accuracy (dashed line) indicating vortex localization. (From Ref. [264].)

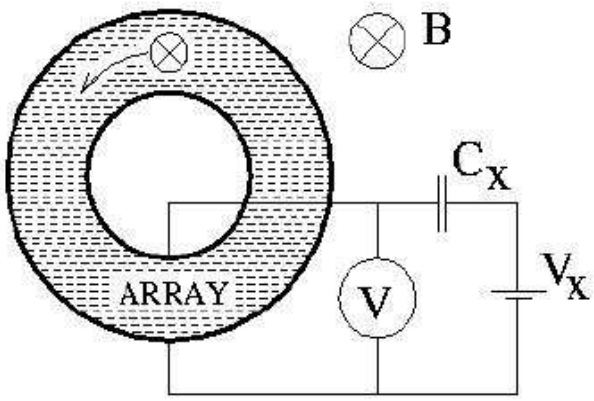

Fig 44 - R. Fazio and H. van der Zant

FIG. 44. The experimental setup to detect interference effects of vortices: The Corbino disk (From Ref. [277].)

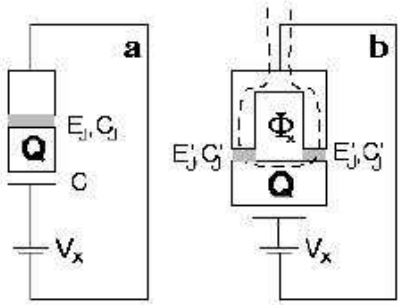

Fig 45 - R. Fazio and H. van der Zant

FIG. 45. a) A charge qubit. b) Improved qubit design as proposed by the Karlsruhe group. The island is coupled to the circuit via two Josephson junctions with parameters $C'_{\rm J}$ and $E'_{\rm J}$. This dc-SQUID is tuned by the external flux which is controlled by the current through the inductor loop (dashed line). The setup allows switching the effective Josephson coupling to zero. (Reprinted by permission from Nature **398**, 305 (1999 copyright 1999 Macmillan Magazines Ltd.)

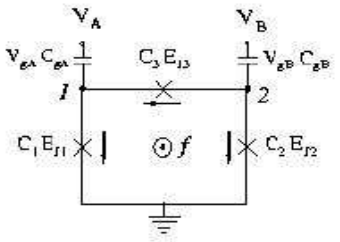

Fig 46 - R. Fazio and H. van der Zant

FIG. 46. The three-junction flux qubit. Josephson junctions 1 and 2 have the same Josephson energies E_J and capacitance C; Josephson junction 3 has a Josephson energy and capacitance that are α times larger. The islands are coupled by gate capacitors $C_g = \gamma C$ to gate voltages V_A and V_B. The arrows define the direction of the currents. (From Ref. [305].)